International Journal of Optics

Recent Advances in Optical 3D Imaging and Display

Lead Guest Editor: Xiaowei Li
Guest Editors: Seok-Tae Kim, Wei Liu, and Wuxiang Zhao

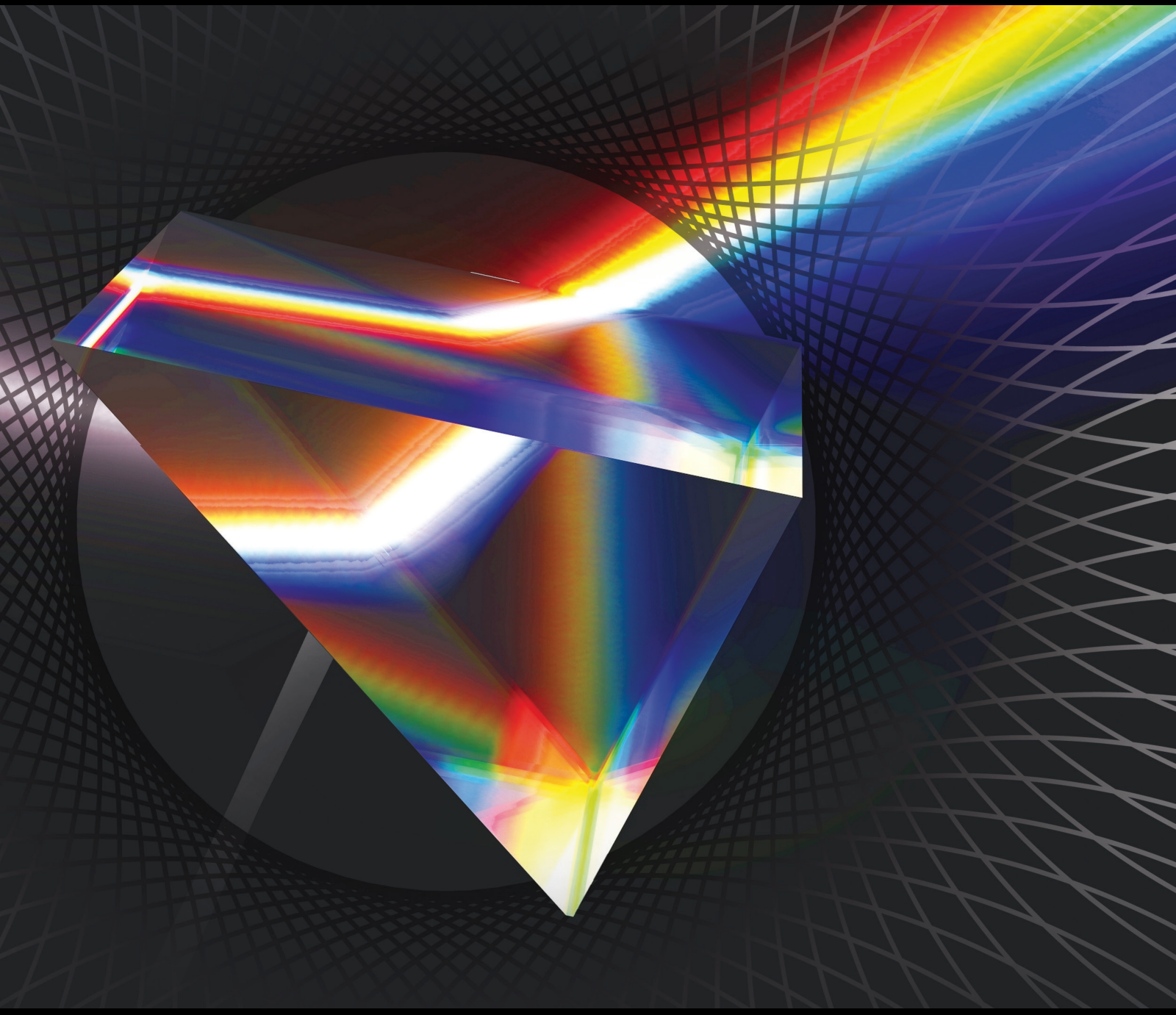

Recent Advances in Optical 3D Imaging and Display

International Journal of Optics

Recent Advances in Optical 3D Imaging and Display

Lead Guest Editor: Xiaowei Li
Guest Editors: Seok-Tae Kim, Wei Liu, and Wuxiang Zhao

Contents

Hindawi
International Journal of Optics
Volume 2022, Article ID 6298010, 20 pages
https://doi.org/10.1155/2022/6298010

Research Article

Single-Pixel Compressive Digital Holographic Encryption System Based on Circular Harmonic Key and Parallel Phase Shifting Digital Holography

B. Lokesh Reddy and Anith Nelleri

School of Electronics Engineering, Vellore Institute of Technology (VIT), Chennai 600127, Tamil Nadu, India

Correspondence should be addressed to Anith Nelleri; anith.nelleri@vit.ac.in

Received 28 January 2022; Accepted 12 May 2022; Published 14 July 2022

Academic Editor: Wei Liu

An encryption system that combines compressive sensing (CS) and two-step parallel phase shifting digital holography (PPSDH) using double random phase encoding (DRPE) is presented in this paper. The two-step PPSDH is a linear inline holographic scheme and is much suitable for encrypting the 2D/3D information in a single exposure. The distribution of random phase mask (RPM) in the DRPE is implemented using circular harmonic key which increases the security of the encryption process. In this system, the keys used to encrypt are spatial positions of the planes, wavelength, and rotation of the circular harmonics in RPMs, and CS acts as an additional key that makes the system more secure than the conventional optical encryption methods. At the transmission end, two-step PPSDH is applied to encrypt the object information in single hologram. The digital mirror device (DMD) is placed between the object and a single-pixel detector for acquiring fewer hologram measurements. At the receiver end, the single digital hologram is numerically recovered by using a CS optimization problem. The original complex object field is decrypted from the CS recovered holograms by the inversion of two-step PPSDH process with the help of the correct keys. The numerical simulations are presented for complex 2D and 3D objects to test the feasibility of the proposed encryption and decryption system. The proposed method carried out intensity and phase reconstruction of the original object field using single-pixel compressive imaging. The computer simulation results demonstrated that the encrypted information is highly secured with the rotation of the circular harmonic key. The sensitivity of the decrypted intensity and phase images is also studied with variations of the encrypted keys. The obtained results show that the proposed encryption scheme is feasible and has better security performance and robustness.

1. Introduction

Digital holography [1–7] is a promising technique to sense and retrieve 3D object information such as amplitude and phase of the object. The optically generated and digitally sensed holograms are numerically reconstructed to obtain 3D object features. The sensed digital hologram is a real-valued digital image. The retrieved 3D information from the digital hologram is a 2D complex image that contains 3D information of the object in the form of intensity and phase. Thus, the existing 2D image processing algorithms can adapt to process 3D information from 2D digital complex images. The optically generated and digitally sensed holograms are numerically reconstructed to obtain the 3D object features. The sensed digital hologram is a real-valued digital image. Digital holography has been widely used in many applications in the areas of phase contrast imaging [8, 9], 3D microscopy [10, 11], 3D object recognition [6, 12], information security [13, 14], surface shape measurement [15–17], interferometry [18, 19], etc.

The optoelectronic and computational imagining concepts involved in digital holography enable us to sense the compressed holographic data by digital sensors. Later on, it can be reconstructed with good accuracy using computational techniques. The compressive sensing (CS) techniques [20–25] can adapt well to digital holography as the process

involves the detection of holographic data in the transform domain. This opens up new avenues for combining compressive data sensing with information security or encryption. Thus, the sensing and computing modalities of digital holography have complemented the CS framework. It has emerged as a secured CS 3D information system with a high data transmission rate and less storage space. The CS [20–25] is a paradigm shift in signal sampling theory that deals with reconstruction of the original signal from fewer samples than those of the Nyquist sampling rate. CS is an iterative procedure to reconstruct the original signal from the incomplete linear measurements by exploiting the sparsity of the signal. In the CS theory, the most commonly used sparse representations of the signal are FFT, DCT, Wavelet, etc. and help in accurate reconstruction of the original signal. CS framework is applied in holographic encryption for sampling and compression in order to reduce the hologram acquisition data and electronic data-processing load at sensors.

In conventional digital holographic encryption/decryption methods, the encrypted information is transmitted at the Nyquist sampling rate. The sender and receiver use a secret key to decrypt the encrypted information. The transmission of hologram requires a large amount of data storage, but the transmission channel bandwidth is limited. Traditionally, holographic encryption methods are implemented based on double random phase encoding (DRPE) [26–31], joint transform correlator (JTC) [32, 33], and ghost imaging (GI) [34], along with the encryptions based on the Fresnel domain [27, 29, 35, 36], Fourier domain, or fractional Fourier domain [37–40]. The CS based encryption methods have the additional advantage that the encryption depends on the measurement matrix (sampling mask) used for the sensing process which will enhance the security level and act as an additional key, which is not used in the conventional optical encryption systems. CS can be implemented in the optical domain using a digital micromirror device (DMD) and a single-pixel detector [41]. A DMD device is a reflective spatial light modulator introduced by Texas instruments that contain many micromirrors. The light incident on the DMD is modulated with the sampling matrix, and then a single-pixel detector records the measurements depending on the orientation of the mirrors [41, 42]. A single-pixel detector sequentially measures the light field that is reflected from the DMD device. The sensed information of a single-pixel detector ($K \ll M$ measurements) is converted from analog to digital information using A/D convertor, and it transmits K random linear measurements of the object under recording. The encrypted information is numerically reconstructed using the CS optimization algorithm [20–25] from fewer measurements. A single-pixel detector can reduce the size and complexity of the sensor at the transmitting end.

In recent years, CS-based optical encryption methods have been increasing the demand for many optical information processing applications [41–53]. The idea of the single-pixel imaging was first proposed by Duarte et al. [41]. Bromberg et al. [43] have demonstrated a real-time pseudo-thermal GI using a combination of the DMD and single-pixel detector. Di et al. [44] have proposed multiple image encryption based on single-pixel compressive holography to encrypt the holograms. The decryption process of each image was carried out using total variation minimization problem. Clemente et al. [45] have adapted a phase shifting digital holography (PSDH) technique with a single-pixel detector to demonstrate the compressive holographic encryption. This method has experimentally reconstructed the amplitude of the ophthalmic lens by retaining only 20% of the hologram pixels. Li et al. [46, 47] have numerically presented a compressive optical image encryption method for inline PSDH by adopting the single-pixel imaging. In this work, the phase shifted digital holograms were acquired using single-pixel detector. In the reconstruction process, the encrypted holograms were reconstructed by retaining various hologram measurements (such as 60%, 80%, and 90%). Finally, the intensity of the original object wavefield was decrypted from the reconstructed holograms by the inversion of PSDH process. Leihong et al. [48] have experimentally presented compressive ghost imaging encryption based on PSDH. The simulation results have shown that the CS scheme improved the security and reconstruction quality of the intensity image. Wang et al. [49] have presented single-pixel compressive holographic encryption by modifying the Mach–Zehnder interferometer setup for multiple-3D-object imaging based on multiple interferences. The numerical simulation results have shown the accurate reconstruction of original 3D object intensity information from encrypted hologram measurements. It has been demonstrated that the cryptosystem provides high encryption capacity and robustness with multiple interferences. Recently, Du et al. [50] have proposed an efficient CS based optical image encryption system using single-pixel imaging. In this method, the input image is encrypted using one random phase mask (RPM) with various recording distances as one-dimensional vector key. It has been numerically presented that the one RPM key at different recording distances minimized the key storage requirement of data transmission and also enhanced the robustness of the encryption system. The encryption systems [44–50] were proposed based on inline schemes such as four-step, three-step, or two-step PSDH. Moreover, the phase reconstruction of the encrypted object field is not presented in the single-pixel compressive holography. The strength of digital holography is the ability to reconstruct the phase information and has great applications in 3D imaging of moving objects. Although the phase reconstruction is accurate in classical PSDH, it is not suitable for moving objects because it involves multiple exposures. On the other hand, to acquire instantaneous 3D image of object wavefield, parallel phase shifting digital holography (PPSDH) [54–56] was proposed. The PPSDH is a single exposure scheme that can be used for imaging moving objects or static objects. In the present work, single-pixel compressive imaging is demonstrated based on PPSDH and circular harmonic keys in DRPE scheme for improving the security level and storage efficiency of holographic data.

The encrypted hologram measurements can be realized with much less criteria than those of the Nyquist sampling.

In this paper, a CS based encryption method to encrypt the complex object information by using linear two-step PPSDH and a circular harmonic key in DRPE is demonstrated. The holographic encryption system is implemented using a phase-only key with the random spatial distribution of circular harmonics in the Fresnel domain to improve the system security performance. The single-pixel compressive imaging is adapted with two-step PPSDH for compression of the encrypted holograms in the optical domain. During the encryption process, the two RPMs, the measurement matrix, the distance, and the wavelength of Fresnel transform are encryption keys. Compared with the traditional encryption scheme, the transmitted information can be significantly reduced with single-shot exposure method, and the circular harmonic key is associated with RPM, which improves the security of the system. In the proposed system, the quality of reconstructed hologram is guaranteed with much less rate than that of the Nyquist sampling. The proposed system is validated using computer simulations to show the proof of the concept. The robustness and key space security of the proposed encryption system have been verified with minimal pixel detection. The CS reconstruction framework was implemented using the Total Variation Minimization by Augmented Lagrangian and Alternating Direction Algorithm (TVAL3) [24]. The efficacy of the proposed cryptosystem has been analyzed using various performance metrics, and also the key space security and robustness of our method have been examined.

2. Proposed Encryption and Decryption Scheme Using a Circular Harmonic Key in DRPE

The schematic representation of the optical encryption arrangement of DRPE using the circular harmonic key in the Fresnel domain is shown in Figure 1(a). In this method, the RPM is expressed in terms of polar coordinates using a circular harmonic key [57, 58] to enhance the security of the optical system. To obtain the circular harmonic key, the Cartesian coordinates (x, y) are converted to the polar coordinates (ρ, φ) using $x = \rho\cos\varphi$ and $y = \rho\sin\varphi$. Thus, the RPM key can be expressed in the Fresnel domain as

$$P(\rho, \varphi) = \exp[i\Phi(\rho, \varphi)], \tag{1}$$

where Φ contains the distribution of random values. The key can be decomposed into circular harmonics [56] with the position (ρ, φ) as the center, which is expressed as follows:

$$\Phi(\rho\cos\varphi, \rho\sin\varphi) = \Phi(\rho, \varphi) = \sum_{m=-\infty}^{\infty} \Phi_m(\rho)\exp[im\varphi], \tag{2}$$

where m is the order of circular harmonics and $\Phi_m(\rho)$ can be calculated as follows:

$$\Phi_m(\rho) = \frac{1}{2\pi}\int_0^{2\pi} \Phi(\rho, \varphi)\exp[im\varphi]\mathrm{d}\varphi. \tag{3}$$

Now, the RPM using a circular harmonic key in the Fresnel domain is defined as follows:

$$P_m(\rho, \varphi) = \exp[i\Re\{\Phi_m(\rho, \varphi)\}], \tag{4}$$

where $\Re$ is the real part of $\Phi_m(\rho, \varphi)$; Φ_m contains the distribution of random values and polar coordinates $\rho = \sqrt{x^2 + y^2}$. The circular harmonic given in (4) is rotation-symmetric, and $\Phi_m(\rho)$ highly depends on the position (ρ, φ). Now, the first RPM_1 is expressed as follows:

$$P_m(\rho_1, \varphi_1) = \exp[i\Re\{\Phi_m(\rho_1, \varphi_1)\}] = \mathrm{RPM}_1, \tag{5}$$

and similarly, the second RPM_2 can be expressed as follows:

$$Q_m(\rho_2, \varphi_2) = \exp[i\Re\{\Phi_m(\rho_2, \varphi_2)\}] = \mathrm{RPM}_2. \tag{6}$$

The inclusion of circular harmonic function [57, 58] in the random phase masks imparts additional degrees of freedom of encoding such as order of harmonics (m), radius (ρ_1, ρ_2), and rotation angle (φ_1, φ_2) to strengthen the security level of the encryption system. Therefore, the proposed encryption scheme with keys in polar coordinates is a solution to the problem of variance in the decryption process. The degree of rotation angle and the order of the circular harmonic key in the RPMs increase the complexity of DRPE process, thus breaking the keys.

The encryption process involves three different planes, i.e., the input plane, the intermediate Fresnel transform plane, and the output plane. The optical system is illuminated with a plane wave of wavelength λ, and the encrypted complex object information is obtained at the output plane in the Fresnel domain. The object $O(x_i, y_i)$ which is located in the input plane (x_i, y_i) is bonded with RPM_1. When the plane wave propagates through the system, the random phase mask distribution $P_m(\rho_1, \varphi_1)$ gets multiplied by $O(x_i, y_i)$ which results in primary random phase encoding. The propagation of this field to the plane at a distance d_1 from the input plane and the resulting complex Fresnel field is denoted by $U(x', y')$ as given in (7). At distance d_1, the field $U(x', y')$ gets multiplied by the second random phase mask $Q_m(\rho_2, \varphi_2)$ resulting in second random phase encoding in the Fresnel plane. This field is further propagated to the output plane by a distance d_2 to obtain the Fresnel encrypted field $G(x_0, y_0)$ as given in (8). The free space propagation corresponding to each plane is modeled by a Fresnel transform with the corresponding distance.

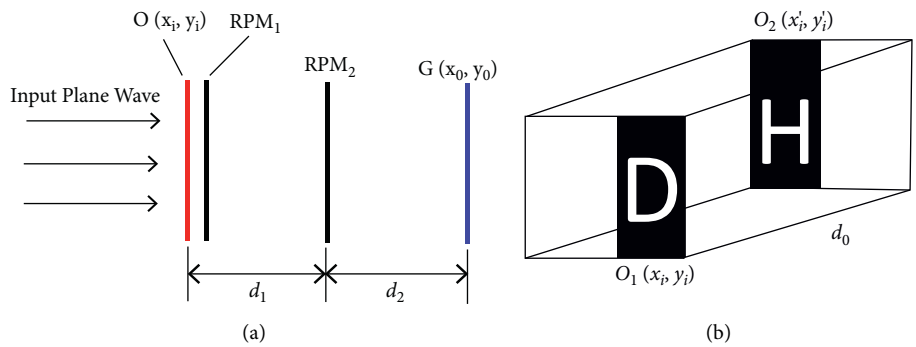

Figure 1: (a) Schematic setup of the DRPE in Fresnel domain illustrating the principle of the encryption system: $O(x_i, y_i)$ is a 2D complex object; RPM_1 and RPM_2, are random phase masks; $G(x_0, y_0)$ is the DRPE information obtained after the two phase masks; d_1 and d_2 are distances between the planes. (b) 3D complex object used in the simulation: $O_1(x_i, y_i)$ is an object at plane 1; $O_2(x_i', y_i')$ is an object at plane 2; d_0 is the distance between the two planes.

$$U(x', y'; d_1) = \frac{e^{ikd_1}}{i\lambda d_1} \iint O(x_i, y_i) P_m(\rho_1, \varphi_1) \exp \frac{i\pi}{\lambda d_1} \left[(x' - x_i)^2 + (y' - y_i)^2 \right] \mathrm{d}x\mathrm{d}y, \tag{7}$$

$$G(x_0, y_0; d_2) = \frac{e^{ikd_2}}{i\lambda d_2} \iint U(x', y') Q_m(\rho_2, \varphi_2) \exp \frac{i\pi}{\lambda d_2} \left[(x_0 - x')^2 + (y_0 - y')^2 \right] \mathrm{d}x\mathrm{d}y. \tag{8}$$

For simplicity, (7) and (8) can be written as follows:

$$G(x_0, y_0) = \mathscr{F}rT_{\lambda,d_2} \left\{ Q_m(\rho_2, \varphi_2) \cdot \mathscr{F}rT_{\lambda,d_1} \{ O(x_i, y_i) \cdot P_m(\rho_1, \varphi_1) \} \right\}. \tag{9}$$

Now, decryption process can be expressed as follows:

$$O(x_i, y_i) = \mathscr{F}rT^{-1}_{\lambda,d_1} \left\{ \mathscr{F}rT^{-1}_{\lambda,d_2} \{ G(x_0, y_0) \cdot Q^*_m(\rho_2, \varphi_2) \} P^*_m(\rho_1, \varphi_1) \right\}, \tag{10}$$

where $\mathscr{F}rT$ is forward Fresnel transform and $\mathscr{F}rT^{-1}$ is inverse Fresnel transform. The decryption process is the same as the encryption shown in (10), but in the reverse direction with complex conjugate of the random phase masks and inverse Fresnel transforms. The Fresnel transform is inverted using the correct keys to obtain the original complex object information.

The 3D complex object used in the encryption system is shown in Figure 1(b). The 3D object construction can be considered as the integration of different sections of complex planes with certain features separated by a small distance d_0 which is analogous to the depth information of the object. Computationally, this is realized by combining the front and back plane with features as shown in Figure 1(b) using the Fresnel transform between the planes corresponding to a distance d_0. Then, 3D object optical encryption process can be expressed as follows:

$$G(x_0, y_0) = \mathscr{F}rT_{\lambda,d_2} \left\{ Q_m(\rho_2, \varphi_2) \cdot \mathscr{F}rT_{\lambda,d_1} \left\{ P_m(\rho_1, \varphi_1) \cdot O_2(x_i', y_i') \cdot \mathscr{F}rT_{\lambda,d_0} \{ O_1(x_i, y_i) \} \right\} \right\}. \tag{11}$$

Similarly, the 3D complex object decryption process is given in the following equations:

$$O_2(x_i', y_i') = \mathcal{F}rT^{-1}_{\lambda,d_1}\left\{\mathcal{F}rT^{-1}_{\lambda,d_2}\{G(x_0, y_0)\}.Q^*_m(\rho_2, \varphi_2)\right\} \cdot P^*_m(\rho_1, \varphi_1), \tag{12}$$

$$O_1(x_i, y_i) = \mathcal{F}rT^{-1}_{\lambda,d_0}\{O_2(x_i', y_i')\}, \tag{13}$$

where d_0 is the distance between two planes, and $O_1(x_i, y_i)$ and $O_2(x_i', y_i')$ are the decrypted 3D object fields at the front and back plane, respectively. Two important features have to be considered for optical encryption techniques. Firstly, the encrypted field must be resistant to attacks, and secondly, the end user has to decrypt the information without any difficulty at the receiver end. An authentic user with the knowledge of RPMs and their circular harmonic key distributions can only decrypt the encrypted information. Thus, circular harmonics improve the security of the optical encryption and decryption process. In this method, the decryption procedure significantly increases the key space security with the operating wavelength, and the spatial positions of the phase mask between the adjacent planes are additional keys for the robust decryption.

The proposed optical encryption system consists of a single-pixel compressive holographic imaging system based on two-step PPSDH that encrypts the complex object information using DRPE and circular harmonic keys. Figure 2 shows the schematic of the proposed optical setup using Mach–Zehnder interferometric recording geometry. The light beam from the laser is divided into two parts using a polarizing beam splitter (PBS). The half wave plates are used to control the intensity and polarization of the interfering light beams. In the object arm, the complex object information is encrypted using DRPE in the Fresnel domain using two RPMs and circular harmonic keys. A phase array device PSLM is used in the reference wave arm to give the required phase shifts to the reference wave in an interleaved manner as mentioned in Section 3. The interference field formed by the encrypted and reference beams is sampled using a DMD by modulating it with a chosen measurement matrix (i.e., sampling mask) for a specific sample ratio. The output of the DMD is coupled to a single-pixel photodetector using a convex lens. Thus, the incomplete measurements of the encrypted single digital Fresnel hologram on the photodetector are obtained. The mathematical model of the proposed encryption and decryption using PPSDH and single-pixel compressive imaging is presented in Section 3.

3. Two-Step PPSDH Approach for Proposed Encryption and Decryption Using Single-Pixel Compressive Imaging

In this section, we present mathematical framework for numerical demonstration of single-pixel digital holographic scheme based on two-step PPSDH and DRPE, in which the random phase masks use circular harmonic key in the Fresnel domain. The flow diagram of the proposed encryption and decryption procedure is shown in Figure 3. The optical encryption technique uses DRPE in the Fresnel domain based on circular harmonic key as explained in Section 2. Let us consider that the input object field $O(x_i, y_i)$ of size $M \times N$ to be encrypted is multiplied by RPM_1. Then, Fresnel transform is performed through propagation distance d_1 and a complex Fresnel field is obtained as described in the following equation:

$$U(x', y') = \mathcal{F}rT_{\lambda,d_1}\{O(x_i, y_i) \cdot \mathrm{RPM}_1\}, \tag{14}$$

where $\mathcal{F}rT$ represents Fresnel transform. $U(x', y')$ field is obtained after RPM1 is multiplied by RPM2. Then, another Fresnel transform is performed, and the obtained encrypted Fresnel field in the DMD plane can be expressed as in the following equation:

$$G(x_0, y_0) = \mathcal{F}rT_{\lambda,d_2}\{U(x', y').\mathrm{RPM}_2\}. \tag{15}$$

Here, RPM_1 and RPM_2 are two independent random phase masks. Now, linear two-step PPSDH [54, 55, 58, 59] is applied for obtaining single-shot inline hologram on the DMD plane, in which a phase array device such as spatial light modulator is used to give phase shifts to the reference wave in an interleaved manner with a periodic phase of $\theta = \{0, -\pi/2\}$. The complex encrypted field $G(x_0, y_0)$ is interfered by the reference wave $R_\theta(x_0, y_0)$. The single-shot inline hologram $H_\theta(x_0, y_0)$ generated on the DMD plane can be expressed as follows:

$$H_\theta(x_0, y_0) = \left|G(x_0, y_0) + R_\theta(x_0, y_0)\right|^2, \tag{16}$$

where

$$R_\theta(x_0, y_0) = \left\{\frac{R_0(x_0, y_0) \text{ when } (x, y) = (\text{even}, \text{even})}{R_{-(\pi/2)}(x_0, y_0) \text{ when } (x, y) = (\text{odd}, \text{even})}\right\}, \quad \text{For}, x_0, y_0 = 0 \text{ to } N-1. \tag{17}$$

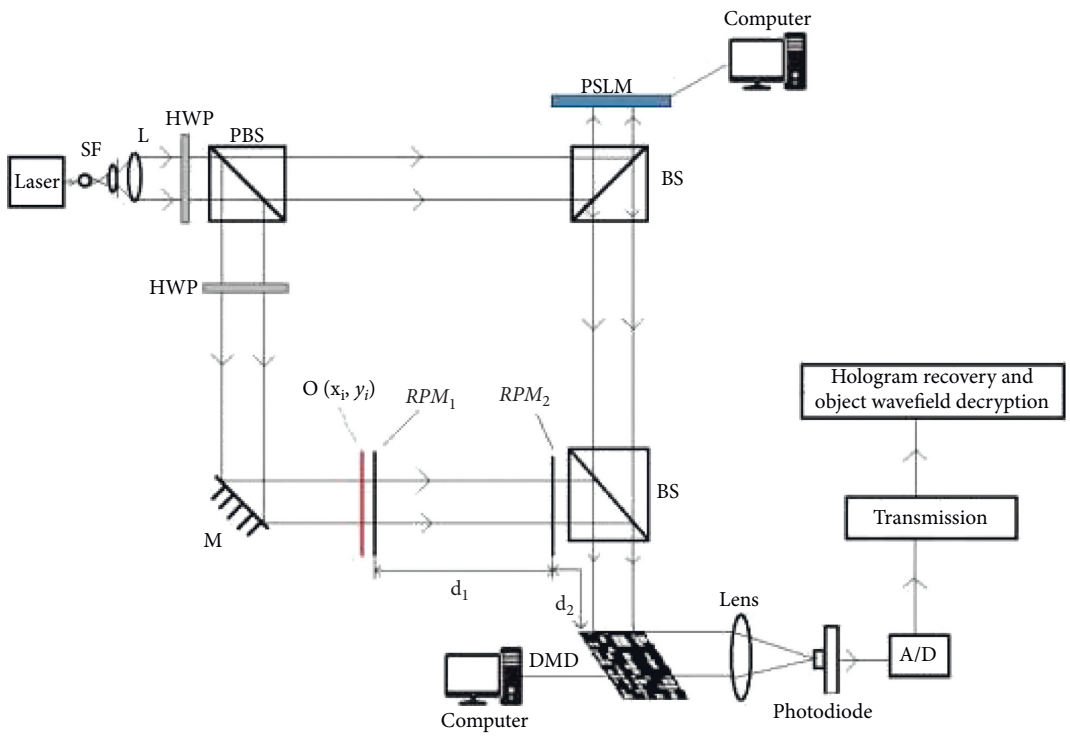

Figure 2: Schematic setup of PPSDH and single-pixel compressive imaging for encryption and decryption. SF: spatial filtering, L: collimation lens, PBS: polarizing beam splitter, HWP: half wave plate, M: mirror, RPM: random phase mask, PSLM: phase-only spatial light modulator, BS: beam splitter, DMD: digital micromirror device.

Therefore, the digital hologram on the DMD plane is governed by the following equation:

$$H_\theta(x_0, y_0) = \left\{ \begin{matrix} H_0(x_0, y_0; 0) \text{ when } (x, y) = (\text{even, even}) \\ H_{-(\pi/2)}(x_0, y_0; -(\pi/2)) \text{ when } (x, y) = (\text{odd, even}) \end{matrix} \right\}, \quad \text{For, } x_0, y_0 = 0 \text{ to } N-1. \tag{18}$$

Now, the measurement matrix Ψ in the DMD is modulated with single-shot hologram $H_\theta(x_0, y_0)$. The random measurement matrix is generated numerically using pseudorandom generator sequences of 0 and 1. Then, the modulated light field reflected from a DMD is measured by a single-pixel detector through M computations of the measurement matrix, and $M \times 1$ linear measurements Y are obtained. The output of the single-pixel detector [41, 59] can be numerically obtained by computing the inner product of the interference filed H_θ and the M computations of the random measurement matrix Ψ with various sample ratios in the DMD plane:

$$Y = \Psi \cdot H_\theta, \tag{19}$$

where $Y \in R^{M\times 1}$ is incomplete measurement data, $\Psi \in R^{M\times N}$ is random vector generated in the DMD, and $H_\theta \in R^{N\times 1}$ is interference filed on the DMD plane.The encrypted incomplete linear measurements are transmitted through the channel and are decrypted at the receiver end. Both sender and receiver share secret keys to decrypt the encrypted information. In the encryption process, the linear measurements $K \ll M$ samples with K nonzero entries are considered less than the Nyquist sampling rate. In the decryption process, first the CS framework is used to recover the original single-shot hologram H_θ from incomplete measurements Y by solving optimization problem [24].

$$\widetilde{H}_\theta = \underbrace{\min}_{H_\theta} \sum_{i=1}^{N^2} \left\| D_i H_\theta \right\|_1 \text{ subject to } Y = \Psi \cdot H_\theta, \tag{20}$$

where D_i denotes discrete gradient of the vector H_θ at position i. Here, $\widetilde{H}_\theta$ denotes the recovered single-shot hologram using CS method. Now, the individual phase shift holograms $\widetilde{H}_0(x_0, y_0)$ and $\widetilde{H}_{-(\pi/2)}(x_0, y_0)$ are separated from single hologram with periodic loss of pixels, and then the separated holograms' values of the vacant pixels are interpolated to obtain the new guess values. The complex Fresnel field $G(x_0, y_0)$ on the DMD plane is obtained using Meng's two-step PSDH formula [43, 60] as given in (21)–(24) and then inverts the encryption process to reconstruct the original object field.

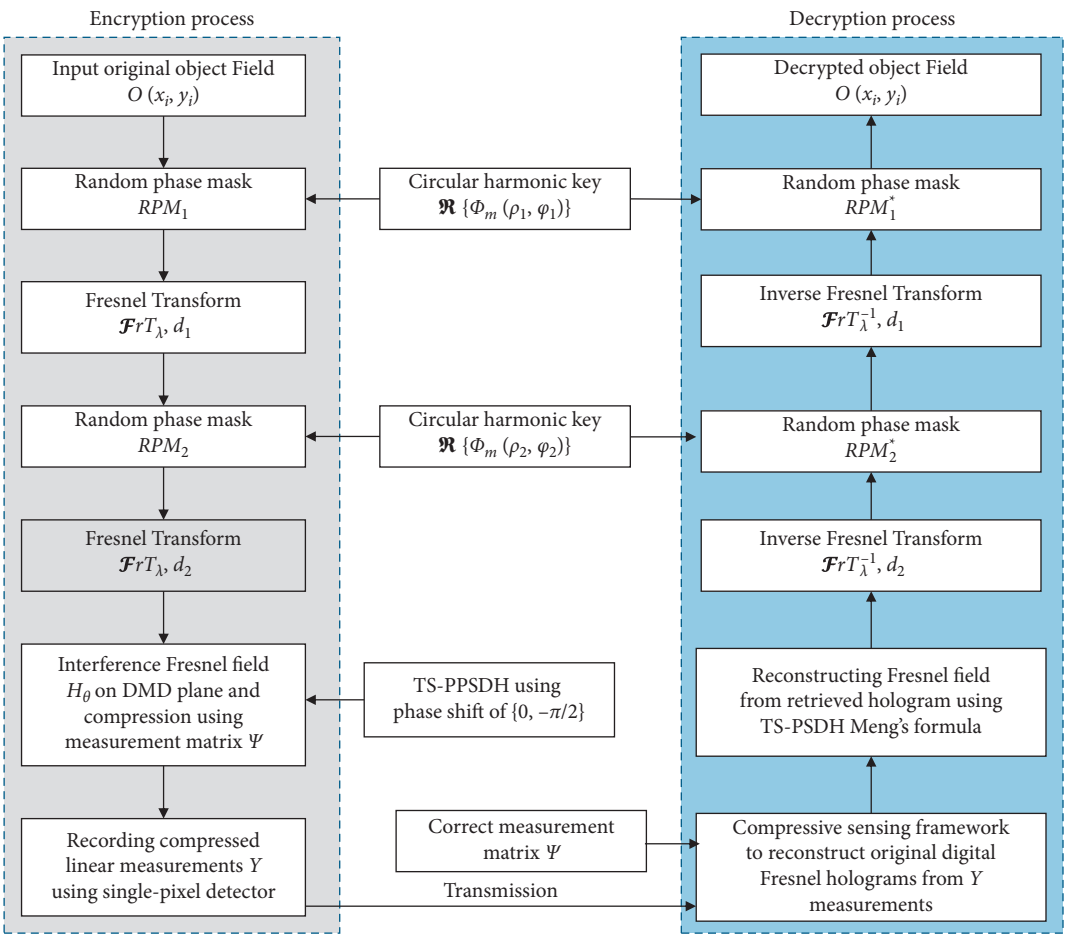

Figure 3: Flowchart of compressive digital holographic encryption and decryption system.

$$G(x_0, y_0) = \frac{\{\tilde{H}_0(x_0, y_0) - a(x_0, y_0)\} - i\{\tilde{H}_{-(\pi/2)}(x_0, y_0) - a(x_0, y_0)\}}{2A_r}, \tag{21}$$

where

$$a(x_0, y_0) = 0.5 * \left\{v - \left(v^2 - 2w\right)^{0.5}\right\}, \tag{22}$$

$$v = \tilde{H}_0(x_0, y_0) + \tilde{H}_{-(\pi/2)}(x_0, y_0) + 2A_r^2, \tag{23}$$

$$w = \tilde{H}_0(x_0, y_0)^2 + \tilde{H}_{-(\pi/2)}(x_0, y_0)^2 + 4A_r^2. \tag{24}$$

The retrieved complex field $G(x_0, y_0)$ is inverse Fresnel propagated by a distance d_2 and multiplied by conjugate of RPM_2 to obtain original field $U(x', y')$:

$$U(x', y') = \mathcal{F}rT_{\lambda,d_2}^{-1}\{G(x_0, y_0)\} \cdot \mathrm{RPM}_2^*. \tag{25}$$

To reconstruct the original encrypted object filed, $U(x', y')$ is inverse-Fresnel-transformed by the distance d_1 and then multiplied by the conjugate phase of the RPM_1.

$$O(x_i, y_i) = \mathcal{F}rT_{\lambda,d_1}^{-1}\{U(x', y')\} \cdot \mathrm{RPM}_1^*. \tag{26}$$

The sample ratio of the measurement matrix is calculated using the formula $(C/L)^*100$, where C is the sample size of compression and L is the size of the original object M^*N. We reduced the sample ratio parameter "C" to study the performance of the hologram compression. The higher the sample size "C," the higher the image quality. To measure the quality of the decrypted complex images, we calculated mean square error (MSE) and relative error (RE) between the original object image and decrypted image, expressed as follows:

$$\mathrm{MSE} = \frac{1}{M \times N} \sum_{x_i=1}^{M} \sum_{y_i=1}^{N} \left[\tilde{O}(x_i, y_i) - O(x_i, y_i)^2\right], \tag{27}$$

$$\mathrm{RE} = \frac{\sum_{x_i=1}^{M} \sum_{y_i=1}^{N} \left|\left|\tilde{O}(x_i, y_i)\right| - \left|O(x_i, y_i)\right|\right|^2}{\sum_{x_i=1}^{M} \sum_{y_i=1}^{N} \left|O(x_i, y_i)\right|^2}, \tag{28}$$

where M and N are the size of the original object, $\widetilde{O}(x_i, y_i)$ is the decrypted complex object wave with compression, and $O(x_i, y_i)$ is the original complex object wave. It can be seen from encryption and decryption system that five keys are used: RPM keys with angles φ_2 and φ_2, distance between two adjacent planes d_1 and d_2, measurement matrix Ψ, and wavelength λ, and the radii of circular harmonic ρ_1 and ρ_2 values stored in the encryption process act as the additional keys in the decryption process. Thus, the proposed system improves the security of the encryption effectively. In the proposed technique, the two-step PPSDH and circular harmonic key in DRPE are combined to improve the reconstruction accuracy and security performance of the decrypted information. The main idea of the digital holographic technique integrated with the single-pixel detector and CS theory is to obtain both the intensity and phase information of a complex 2D or 3D scene under recording.

4. Simulation Experiments and Discussion

To verify the proposed scheme, two numerical simulations were conducted. The parameters used in the simulations were the wavelength $\lambda = 632.8$ nm; the order of circular harmonic key $m = 2$; the rotation angles and radii of the two circular harmonic keys: $\varphi_1 = 3^\circ$, $\varphi_2 = 6^\circ$ and $\rho_1 = 6.38$, $\rho_2 = 8.29$; and the distance between two adjacent planes is $d_1 = d_2 = 40$ mm from the DMD plane.

4.1. 2D Complex Object Encryption and Decryption Results. A binary 2D complex object field "E" of size 64×64 was used in the simulation. The intensity of the 2D object was taken as 0.5, and the corresponding phase was considered as e^{1j}. In order to visualize the quality of the phase in the reconstruction process, we have chosen constant phase value in the object function. The original complex object field is encrypted using (9) in the proposed system. The original intensity and the phase of the input complex object field are shown in Figures 4(a) and 4(b), respectively. The circular harmonic key of order $m = 2$ was used in the random phase mask as shown in Figure 4(c). The encrypted Fresnel field at the DMD plane was produced by using Fresnel transform equations (7)-(8). The measurement matrix Ψ was used in the simulation with random sequences of 0 and 1. The encrypted complex Fresnel field from the object path was interfered with the retarded reference wave to obtain the interference filed and then modulated with the measurement matrix. The simulated single-shot inline digital Fresnel hologram on DMD plane is shown in Figure 4(d).

At the receiver end, the compressed single-shot digital hologram is recovered with correct Ψ matrix by solving the unconstrained CS optimization equation as given in (20). The recovered digital holograms from 50% measurements after interpolation are shown in Figures 4(e) and 4(f). The complex Fresnel field was retrieved from the recovered digital holograms using (21)–(24) and inverted the DRPE process as specified in (10). When one of RPM_2 is incorrect, the decrypted intensity and phase distribution are shown in Figures 5(a) and 5(b), respectively. A small change in the decryption distance $d_1 = 41$ mm used in the reconstruction process results in noisy intensity and phase distribution as shown in Figures 5(c) and 5(d). Figures 5(e) and 5(f) show the intensity and phase of the incorrect measurement matrix which is replaced with the original matrix Ψ. The decrypted simulation results with correct keys are shown in Figures 6 and 7.

4.2. 3D Complex Object Encryption and Decryption Simulation Results. The encryption and decryption simulation procedure of the 3D complex object is explained in Section 2. To simulate the 3D complex object, we have considered two transparent objects, "D" and "H," made of binary images. The light propagates through the first object plane and obtains the features of the first complex object "D." Then, the obtained features of first object plane are propagated through a distance of $d_0 = 5$ mm using Fresnel propagation (Fresnel transform) and obtain another complex object features "H" in the second plane. Therefore, finally the 3D complex object information is obtained immediately after the second plane which contains depth information of the objects. The intensity and complex phase of the two objects are taken as 1.0 and e^{1j}, respectively. The simulation process of DRPE and compression of the interferograms are carried out as explained in Section 4.1. Finally, the 3D complex object scene at two different sections can be reconstructed back with single digital hologram using CS algorithm and then invert the two-step PPSDH process with original keys.

The decrypted results with incorrect keys are shown in Figure 8. The intensity and phase distribution of 3D complex object scene are decrypted at first plane with one of the incorrect RPM_2 keys. The decrypted intensity and phase distribution are shown in Figures 8(a) and 8(b). Figures 8(c) and 8(d) shows the intensity and phase distribution of incorrect distance key, $d_1 = 41$ mm, was used for decrypting the complex object at first plane. When an incorrect Ψ is replaced with measurement matrix, the intensity and phase distribution of 3D object scene decrypted at first plane are shown in Figures 8(e) and8(f).

4.3. Compressive Ratio Performance. Figure 6 shows the relationship between MSE and sample ratio of the decrypted intensity and phase images for different sample ratios. From Figure 6, it can be seen that when the compression ratio is less than 30% measurements than its intensity, phase reconstruction accuracy is feasible for both the simulations, as shown in Figures 7(a)–7(c) and Figures 9(a) and 9(b). Its corresponding phase images are shown in Figures 10(a)–10(c) and Figures 11(a) and 11(b). When the sample ratio is between 30% and 40% measurements, then the decrypted intensity and phase images' accuracy is acceptable, as shown in Figures 7(c), 10(c), 9(c) and 9(d), and 11(c) and 11(d), respectively.

When the sample ratio is greater than 40% measurements, then the intensity and phase reconstruction quality is

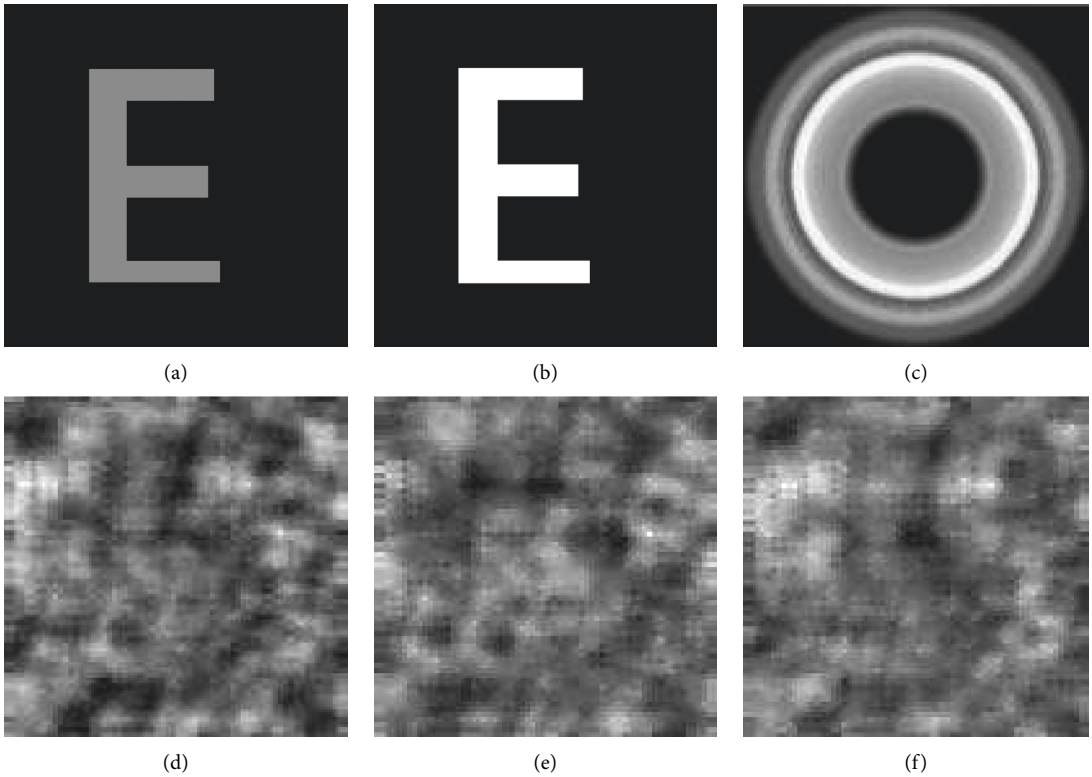

Figure 4: Simulation results based on the proposed encryption system: (a) intensity and (b) the corresponding phase of Figure 4(a), (c) one of the circular harmonic keys $P_m(\rho_1, \varphi_1)$ of order $m = 2$ and $\varphi_1 = 3^\circ$, (d) simulated two-step PPSDH on DMD plane, (e) recovered $\widetilde{H}_0$ digital hologram, and (f) recovered $\widetilde{H}_{-(\pi/2)}$ digital hologram after interpolation from $64 \times 64 \times 50\%$ measurements using CS framework.

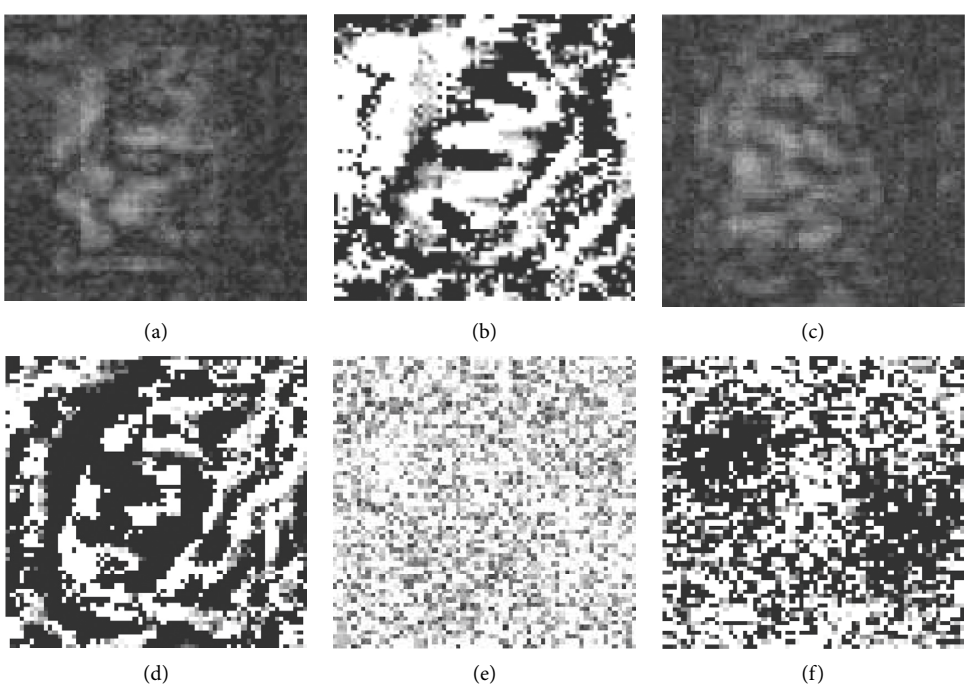

Figure 5: Decryption results using incorrect keys with $64 \times 64 \times 50\%$ measurements: (a) reconstructed intensity distribution when one of RPM_2 is wrong and (b) the corresponding phase, (c) reconstructed intensity distribution when one of the d_1 decryption distances is wrong and (d) the corresponding phase, and (e) reconstructed intensity distribution when the measurement matrix Ψ is incorrect and (f) the corresponding phase.

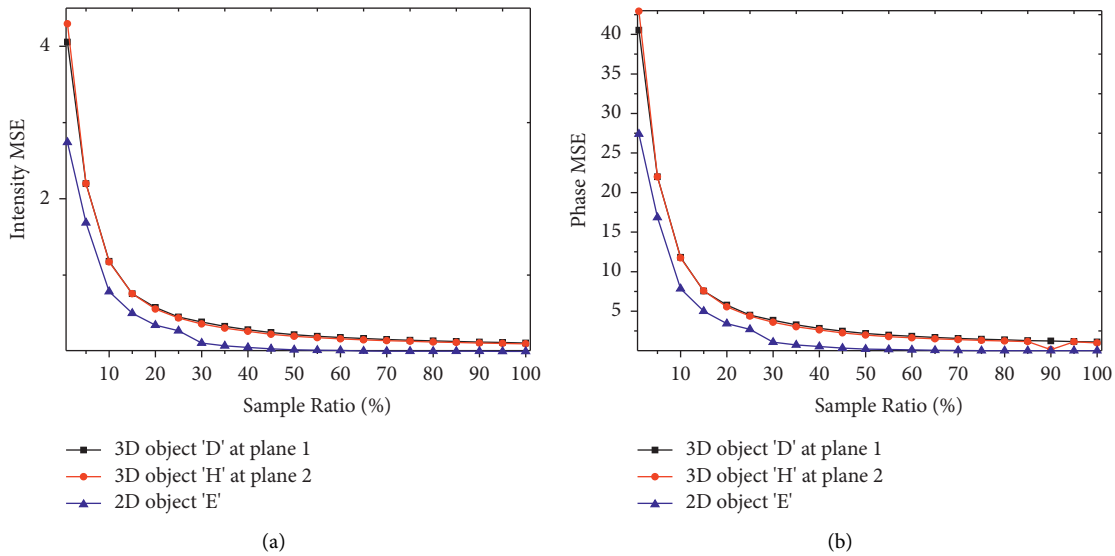

Figure 6: Performance of sample ratio versus MSE between decrypted and original complex wave: (a) MSE of intensity deviation; (b) MSE of phase deviation.

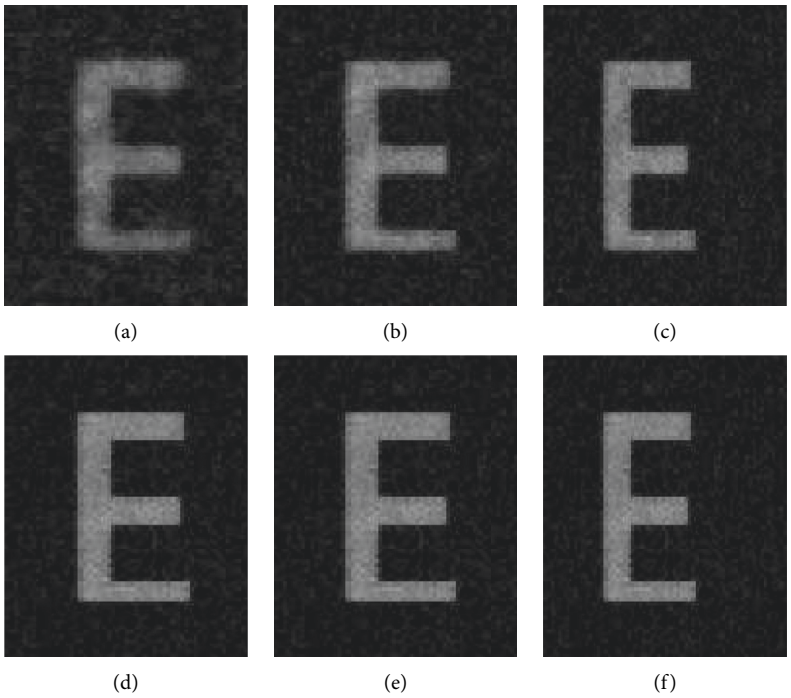

Figure 7: Intensity distribution of the decrypted 2D object using correct keys: (a) $64 \times 64 \times 5\%$ measurements; (b) $64 \times 64 \times 10\%$ measurements; (c) $64 \times 64 \times 15\%$ measurements; (d) $64 \times 64 \times 35\%$ measurements; (e) $64 \times 64 \times 45\%$ measurements; (f) $64 \times 64 \times 65\%$ measurements.

similar to the original image, as shown in Figures 7(e) and 7(f), 10(e) and 10(f), 9(e) and 9(f), and 11(e) and 11(f), respectively. Figures 7–11 show the decrypted intensity and phase distribution of both 2D and 3D object simulation cases from various sample ratios. If the correct keys such as wavelength, propagation distance, RPMs, and measurement matrix are used, then the decrypted intensity and phase images for both 2D and 3D simulation cases are shown in Figures 7–11. If the different wrong keys are used in the decryption process, the quality of the decrypted intensity and phase images are affected and fail to reconstruct the originalobject wavefield as shown in Figures 12–18.

4.4. Key Space Security and Sensitivity Analysis. Figures 12–18 show the sensitivity of the keys with a small deviation δ when the correct keys fail to decrypt the original

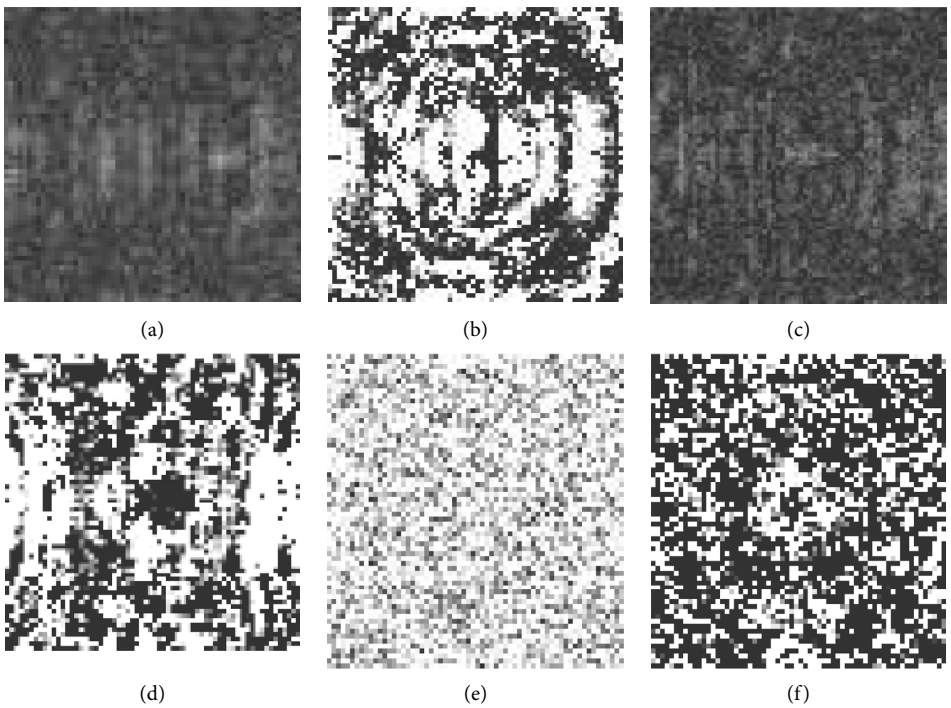

Figure 8: Decrypted simulation results: (a) intensity information when one of the circular harmonic keys, RPM_2, is wrong and (b) the corresponding phase; (c) intensity information when one of the d_1 distances is wrong and (d) the corresponding phase; (e) intensity information when the measurement matrix Ψ is incorrect and (f) the corresponding phase.

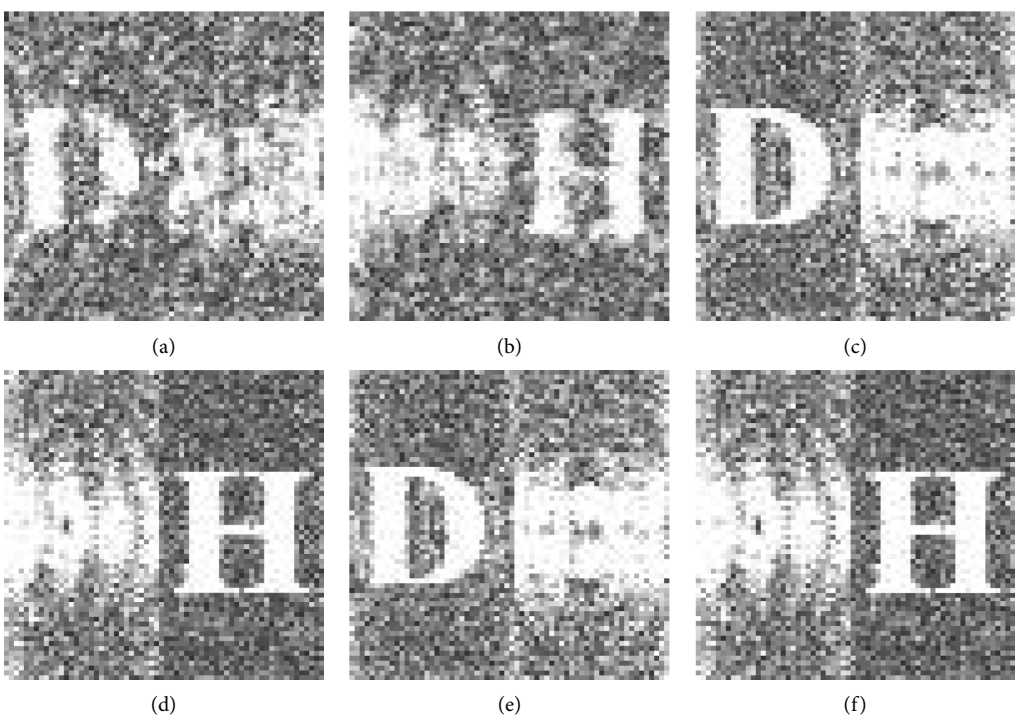

Figure 9: Intensity of the decrypted 3D object scene using correct keys: (a) reconstructed at first plane with $64 \times 64 \times 8\%$ measurements; (b) reconstructed at second plane with $64 \times 64 \times 8\%$ measurements; (c) reconstructed at first plane with $64 \times 64 \times 25\%$ measurements; (d) reconstructed at second plane with $64 \times 64 \times 25\%$ measurements; (e) reconstructed at first plane with $64 \times 64 \times 65\%$ measurements; (f) reconstructed at second plane with $64 \times 64 \times 65\%$ measurements.

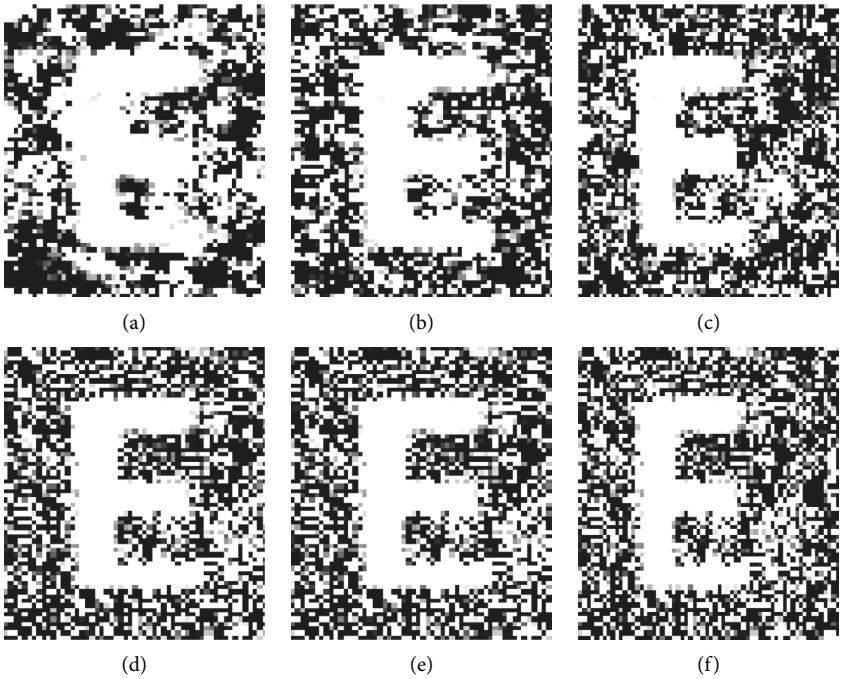

Figure 10: Phase distribution of the decrypted 2D object using correct keys: (a) $64 \times 64 \times 5\%$ measurements; (b) $64 \times 64 \times 10\%$ measurements; (c) $64 \times 64 \times 15\%$ measurements; (d) $64 \times 64 \times 35\%$ measurements; (e) $64 \times 64 \times 45\%$ measurements; (f) $64 \times 64 \times 65\%$ measurements.

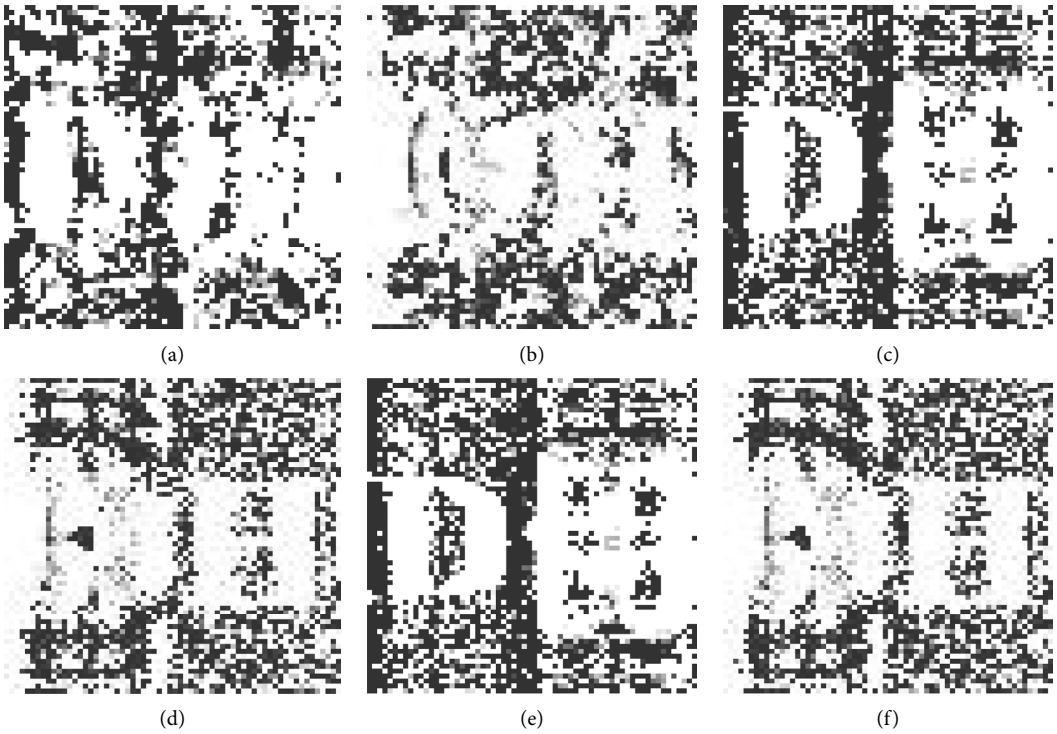

Figure 11: Phase distribution of the decrypted 3D object using correct keys: (a) reconstructed at first plane with $64 \times 64 \times 8\%$ measurements; (b) reconstructed at second plane with $64 \times 64 \times 8\%$ measurements; (c) reconstructed at first plane with $64 \times 64 \times 25\%$ measurements; (d) reconstructed at second plane with $64 \times 64 \times 25\%$ measurements; (e) reconstructed at first plane with $64 \times 64 \times 65\%$ measurements; (f) reconstructed at second plane with $64 \times 64 \times 65\%$ measurements.

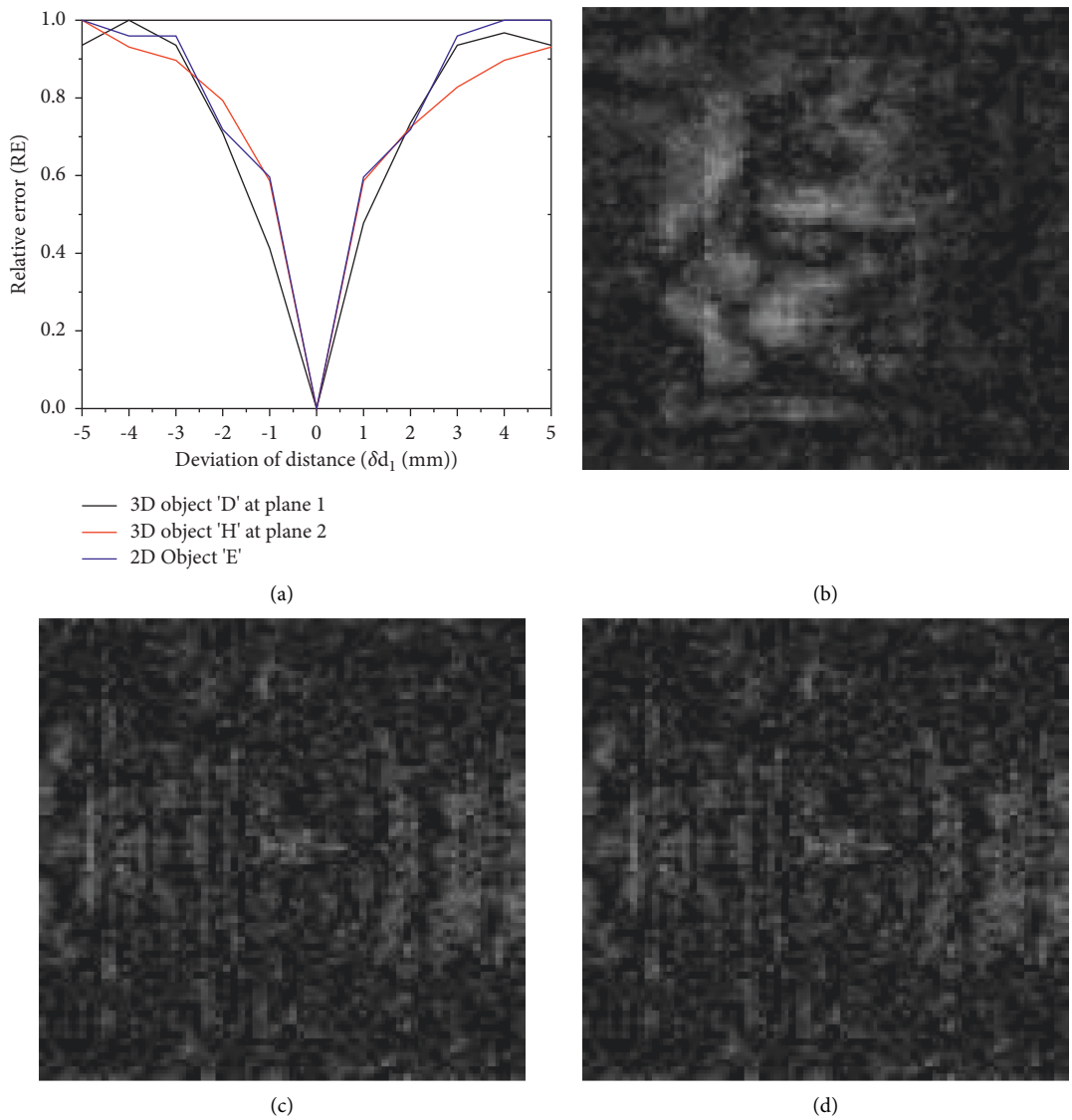

Figure 12: Decrypted results with incorrect d_1 distances: (a) the RE plot corresponding to the deviation of distance; (b) reconstructed 2D object with wrong distance d_1 = 41 mm; (c), (d) reconstructed 3D object wave with wrong distance d_1 = 41 mm at first plane and second plane, respectively.

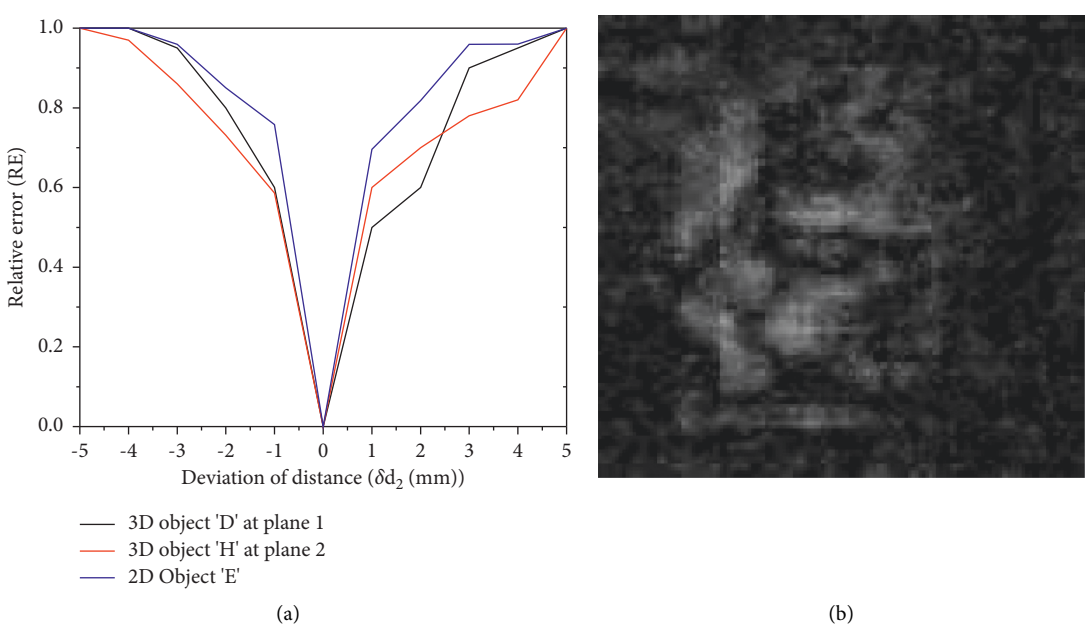

Figure 13: Continued.

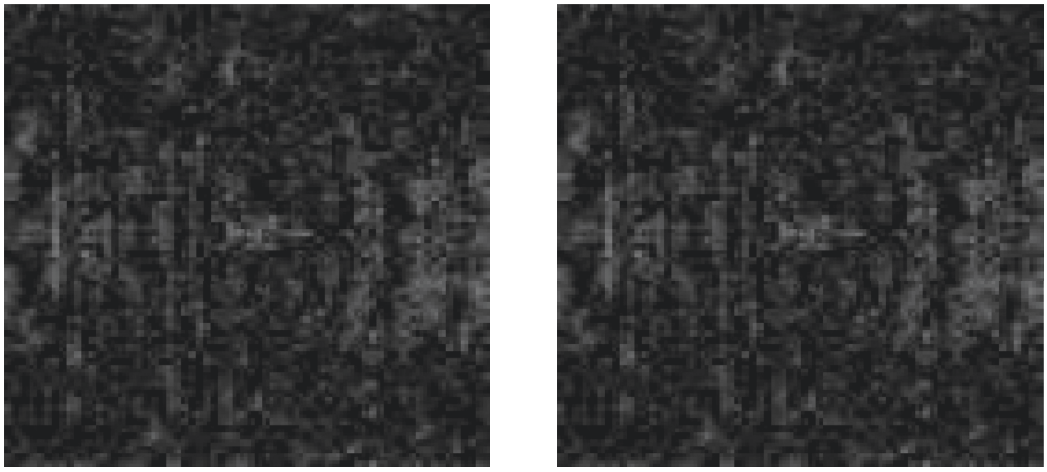

(c) (d)

Figure 13: Decrypted results with incorrect d_2 distances: (a) the RE plot corresponding to the deviation of distance; (b) reconstructed 2D object with wrong distance $d_2 = 41$ mm; (c), (d) reconstructed 3D object wave with wrong distance $d_2 = 41$ mm at first plane and second plane, respectively.

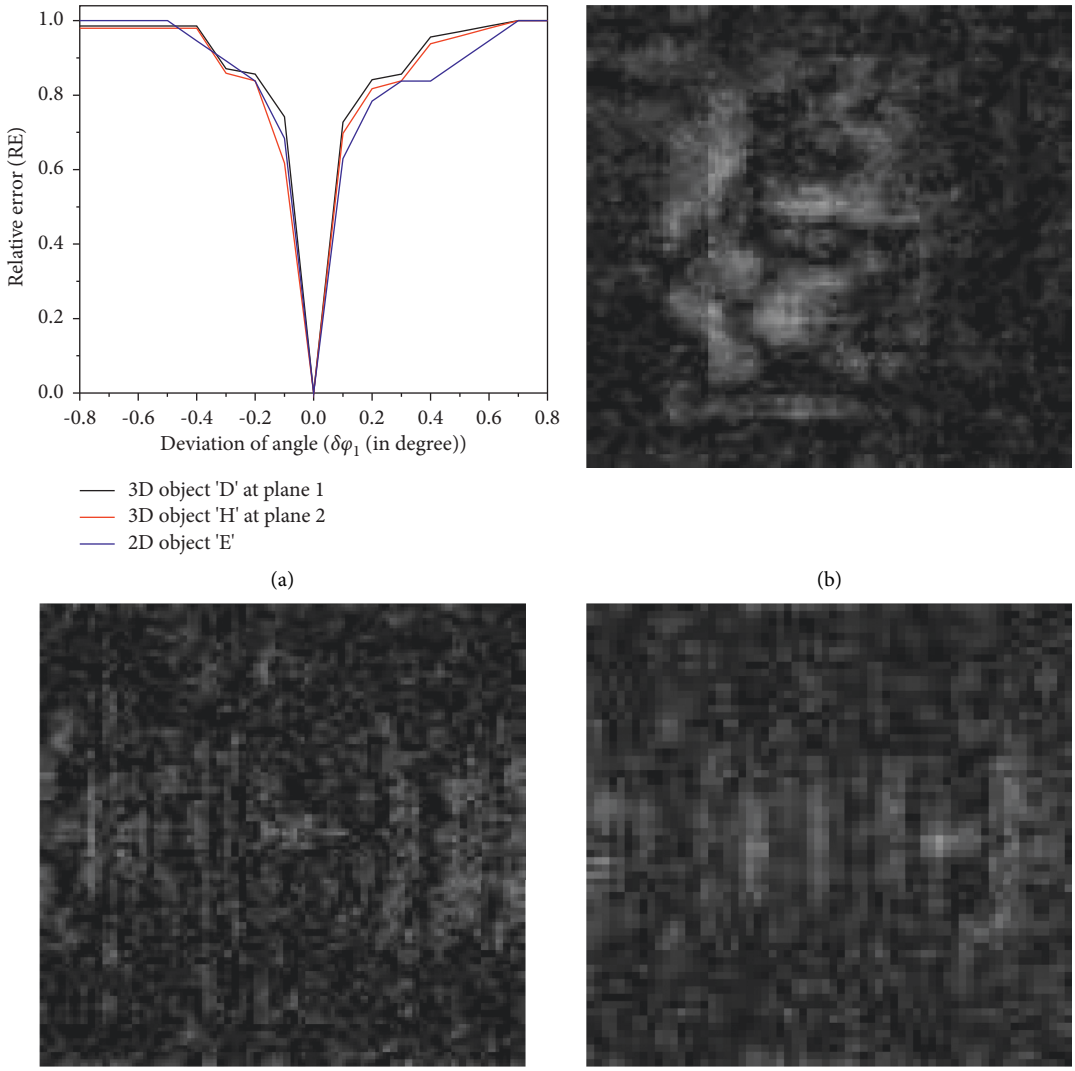

Figure 14: Decrypted results with wrong angle of $p_m(\rho_1, \varphi_1)$: (a) the RE plot corresponding to the deviation of distance; (b) reconstructed 2D object with wrong angle $\varphi_1 = 3.1^\circ$; (c), (d) reconstructed 3D object with wrong angle $\varphi_1 = 3.1^\circ$ at first plane and second plane, respectively.

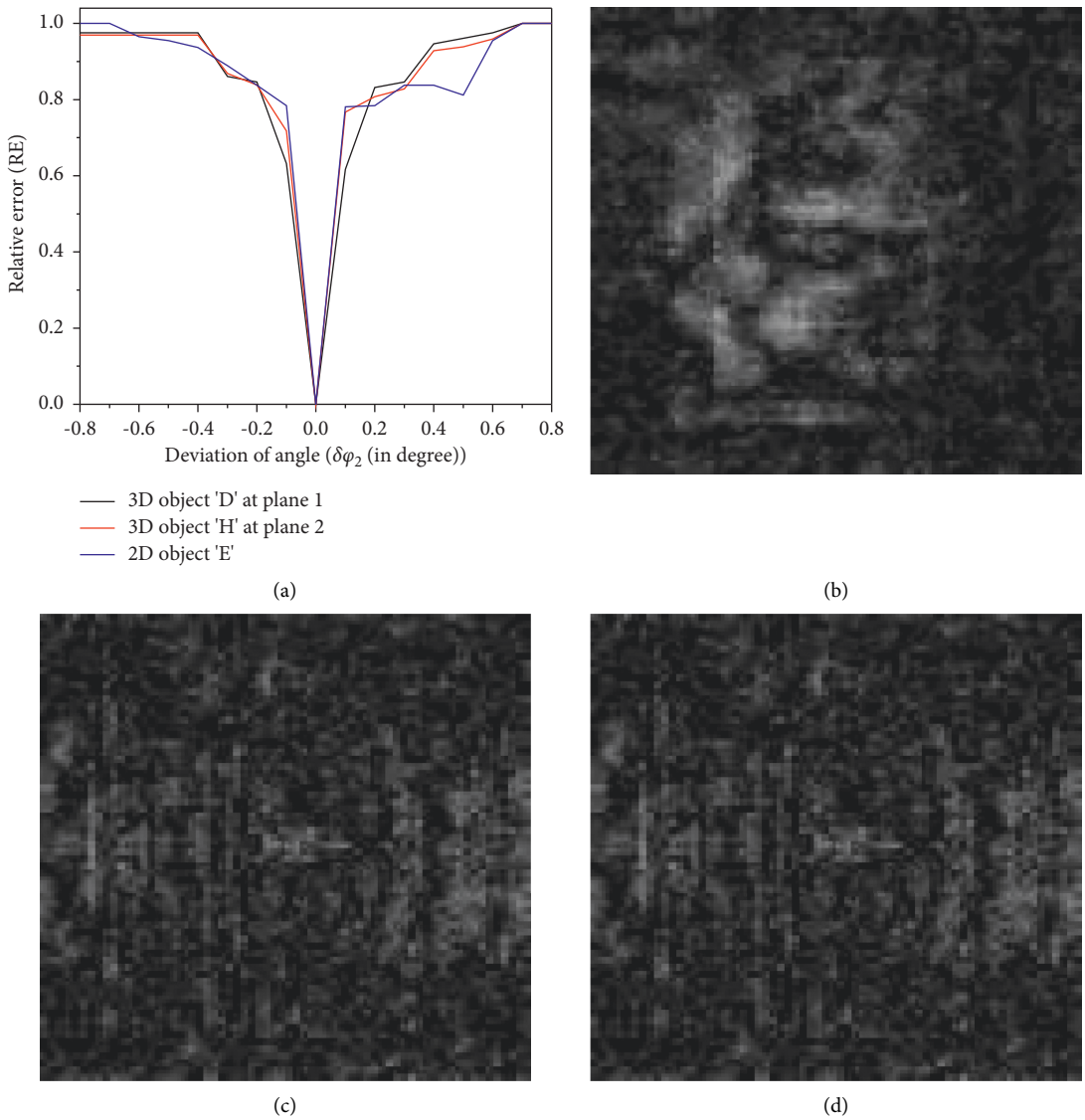

Figure 15: Decrypted results with wrong angle of $Q_m(\rho_2, \varphi_2)$: (a) the RE plot corresponding to the deviation of angle; (b) reconstructed 2D object with wrong angle $\varphi_2 = 6.1^\circ$; (c), (d) reconstructed 3D object with wrong angle $\varphi_2 = 6.1^\circ$ at first plane and second plane, respectively.

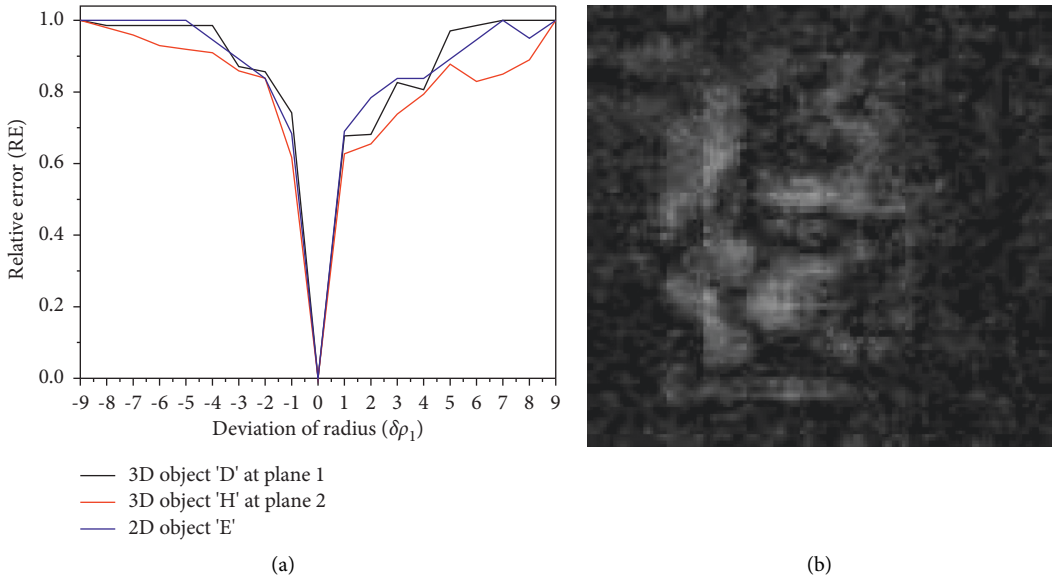

Figure 16: Continued.

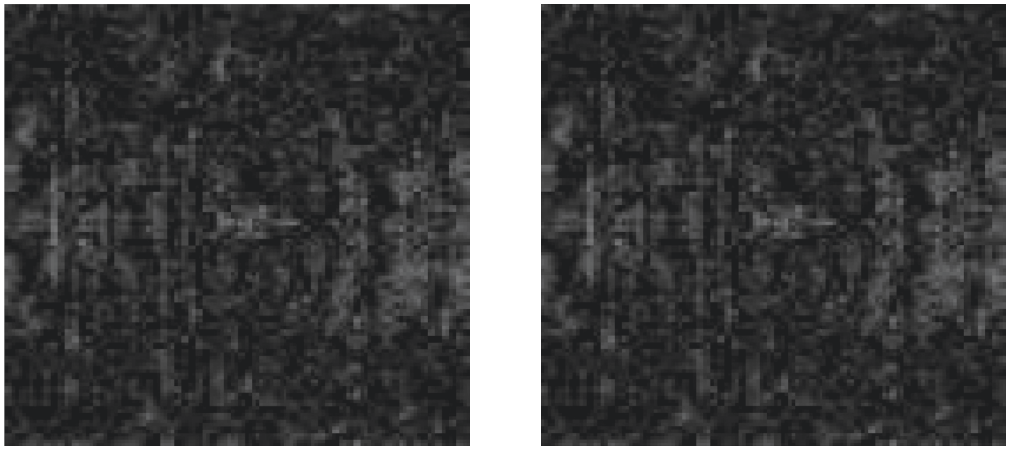

(c) (d)

Figure 16: Decrypted results with incorrect radius of $P_m(\rho_1, \varphi_1)$: (a) the RE plot corresponding to the deviation of radius; (b) reconstructed 2D object with incorrect radius $\rho_1 = 7.38$; (c), (d) reconstructed 3D object with incorrect radius $\rho_1 = 7.38$ at first plane and second plane, respectively.

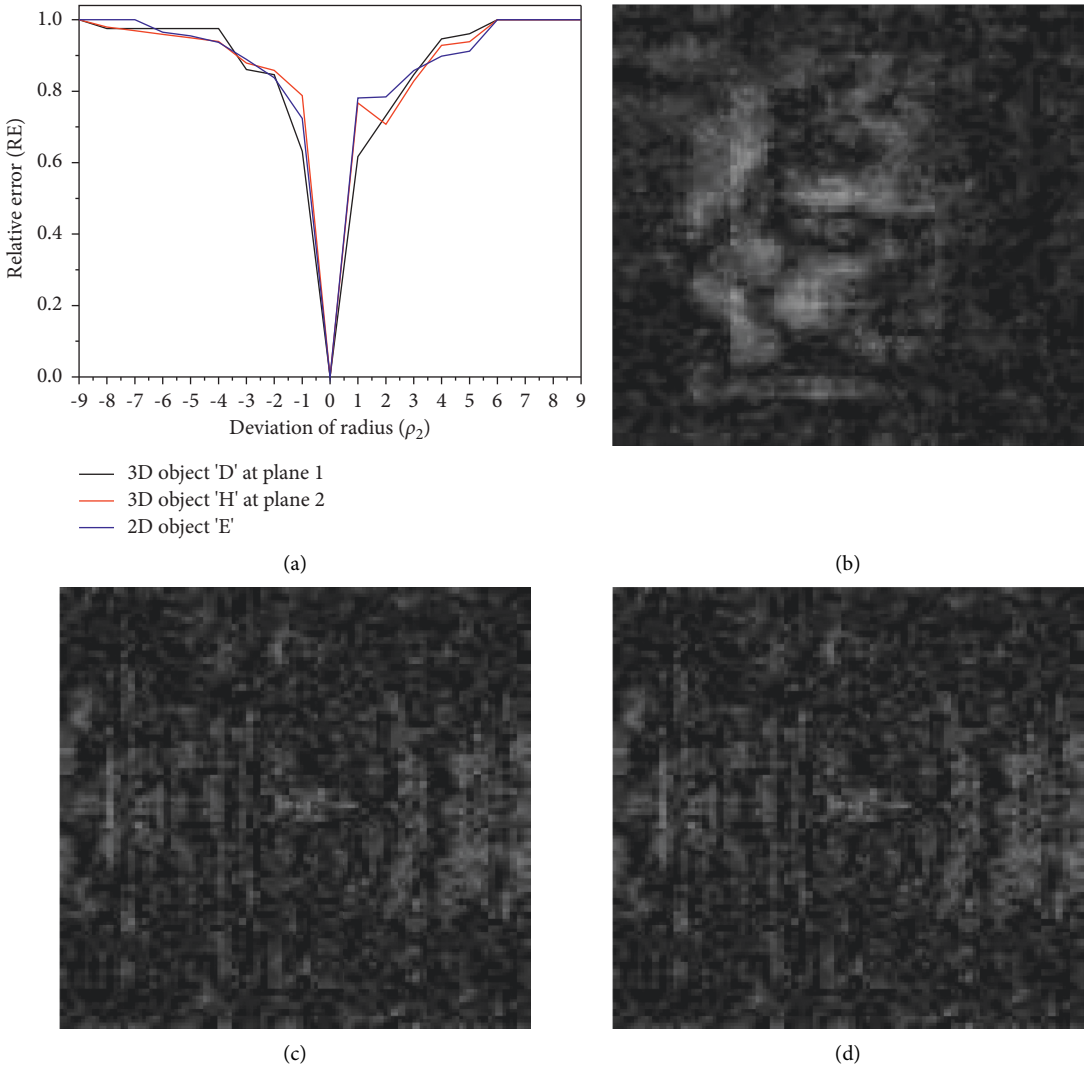

Figure 17: Decrypted results with wrong radius of $Q_m(\rho_2, \varphi_2)$: (a) the RE plot corresponding to the deviation of radius; (b) reconstructed 2D object with incorrect radius $\rho_2 = 9.29$; (c), (d) reconstructed 3D object with incorrect radius $\rho_2 = 9.29$ at first plane and second plane, respectively.

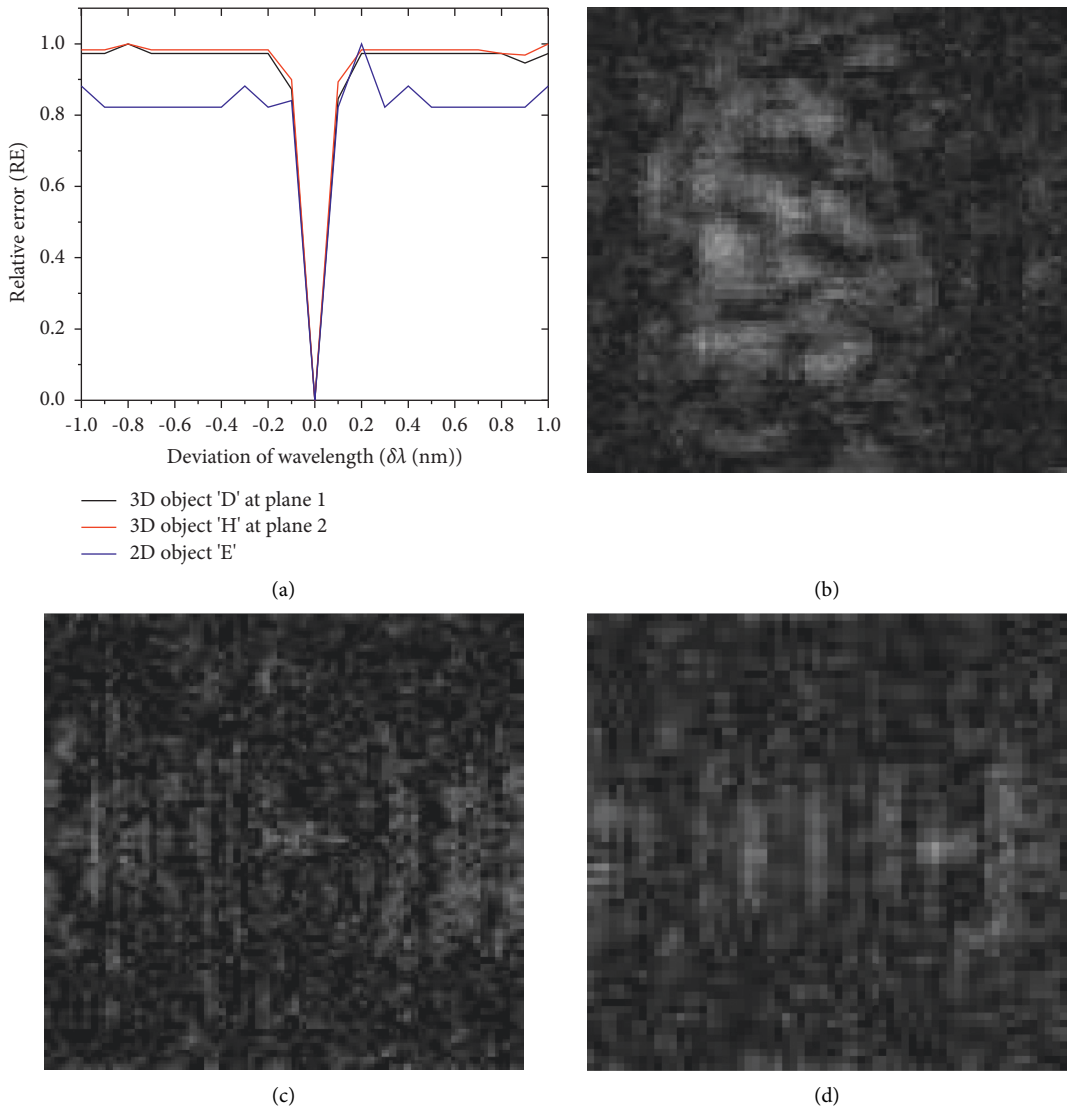

Figure 18: Decrypted results with wrong wavelength: (a) the RE plot corresponding to the deviation of wavelength; (b) reconstructed 2D object with wrong wavelength $\lambda = 632.81$ nm; (c), (d) reconstructed 3D complex object with wavelength $\lambda = 632.81$ nm at first plane and second plane, respectively.

complex object and completely looks like a noisy image. It can be seen that the RE plot value reaches minimum only when the decrypted keys are the same as the encrypted keys; otherwise, the RE value is maximum. The quality of the decrypted complex object is high when RE value is minimum; otherwise, it appears like a noisy image. Figures 12–18 show the RE plot of the decrypted complex object with deviation in the decrypted keys for both 2D and 3D simulation cases.

From Figures 12 and 13, it can be observed that the RE plot decreases to zero sharply only when the decrypted distance is the same as the simulation recording distance. Figures 12(b) and 13(b) show that the decrypted 2D complex object looks like a noisy image when a wrong distance key, $d_1 = d_2 = 41$ mm, is used. On the other hand, Figures 12(c), 12(d), 13(c), and 13(d) show the decrypted complex object of the 3D object with wrong distance key, $d_1 = d_2 = 41$ mm, at first plane and second plane, respectively.

It can be seen from Figures 14 and 15 that the RE plot value decreases to zero sharply with a small variation in the angle of $\pm 0.1^\circ$ for both simulation cases. When the wrong angle of the RPM_1 key $\varphi_1 = 3.1^\circ$ is used instead of the correct key value 3°, the decrypted results are shown in Figure 14. Similarly, when the wrong angle of another RPM_2 key $\varphi_2 = 6.1^\circ$ is used to decrypt the complex object for both the simulation cases, it fails to reconstruct original object wave as shown in Figure 15.

It can be seen from Figures 16 and 17 that the RE plot value decreases to zero sharply with a small variation in the radius of ± 1.0 for both 2D and 3D simulation cases. The decrypted results for the incorrect radius of the RPM_1 key when $\rho_1 = 7.38$ are shown in Figure 16. Similarly, the wrong radius of the other mask RPM_2 key, when $\rho_2 = 9.29$, was used for decryption, and it failed to reconstruct the original object wave, as shown in Figure 17.

The sensitivity of the recording wavelength was also studied. The wrong wavelength of $\lambda = 632.81$ nm was used, and its corresponding decrypted complex object result is shown in Figure 18. Here, it can be seen that the RE plot of the wavelength decreases to zero sharply with a small deviation of ±0.01 nm as shown in Figure 18(a). From the above results, it can be concluded that the proposed compressive digital Fresnel holographic encryption system is sensitive to the small variations in the decrypted keys such as measurement matrix, distance, wavelength, and rotation of the RPM using circular harmonic key. Therefore, the increase in the sensitivity of the keys results in the difficulty of duplicating the keys in the decryption process.

5. Conclusion

In this paper, an efficient 2D and 3D information security system is proposed using single-pixel compressive digital holography. The proposed system combines CS and digital holography for complex data encryption using minimal pixel detection. The hologram encryption process uses a DRPE scheme in the Fresnel domain using circular harmonic key, and this scheme enhances the security performance of the decryption process with the variation of the rotation key as presented in the simulation results. In addition, the measurement matrix and other digital holographic secret keys make the system more secure than the conventional method. The two-step PPSDH technique and CS based system are combined to improve the resolution of the reconstructed images. Due to the single-pixel imaging and PPSDH, the 3D information transmission and data storage are effectively reduced. The numerical simulation results show that the proposed cryptosystem has capability to decrypt the intensity and phase information of the object wave accurately from highly compressed digital Fresnel hologram. To quantify the reconstructed complex images, MSE and RE are analyzed for different compression ratios and different key attacks. A small deviation in the decrypted key leads to a considerable increase in the RE value and thus failure to reconstruct the original object information. It is verified from the results that the encryption system has high security and robustness and can be used in many information security applications.

Data Availability

The data used to support the findings of this study are included within the article.

Conflicts of Interest

The authors declare that they have no conflicts of interest.

Acknowledgments

This work was supported by Science and Engineering Research Board (SERB), Department of Science and Technology, Government of India, under the sanction order no. CRG/2018/003906.

References

[1] U. Schnars and W. Jueptner, *Digital Holography*, Springer, Berlin, Germany, 2005.

[2] U. Schnars and W. Jüptner, "Direct recording of holograms by a CCD target and numerical reconstruction," *Applied Optics*, vol. 33, no. 2, pp. 179–181, 1994.

[3] P. Picart and J. Leval, "General theoretical formulation of image formation in digital Fresnel holography," *Journal of the Optical Society of America*, vol. 25, no. 7, pp. 1744–1761, 2008.

[4] J. W. Goodman, *Introduction to Fourier Optics*, Roberts and Company Publishers, Greenwood, CO, USA, 2005.

[5] A. Nelleri, J. Joseph, and K. Singh, "Recognition and classification of three-dimensional phase objects by digital Fresnel holography," *Applied Optics*, vol. 45, no. 17, pp. 4046–4053, 2006.

[6] A. Nelleri, U. Gopinathan, J. Joseph, and K. Singh, "Three-dimensional object recognition from digital Fresnel hologram by wavelet matched filtering," *Optics Communications*, vol. 259, no. 2, pp. 499–506, 2006.

[7] Y. Zhang, Y. Zhu, and E. Y. Lam, "Holographic 3D particle reconstruction using a one-stage network," *Applied Optics*, vol. 61, no. 5, pp. B111–B120, 2022.

[8] T. Tahara, Y. Kozawa, A. Matsuda, and R. Oi, "Quantitative phase imaging with single-path phase-shifting digital holography using a light-emitting diode," *OSA Continuum*, vol. 4, no. 11, pp. 2918–2927, 2021.

[9] N. Hai and J. Rosen, "Single-plane and multiplane quantitative phase imaging by self-reference on-axis holography with a phase-shifting method," *Optics Express*, vol. 29, no. 15, pp. 24210–24225, 2021.

[10] V. F. Rad, A. Babaei-Ghazvini, R. Jamali, I. Shahabi-Ghahfarrokhi, and A.-R. Moradi, "Digital holographic microscopy for real-time investigation of 3D microstructural dynamics of starch-kefiran-based nanocomposite," *Applied Optics*, vol. 60, no. 16, pp. 4706–4715, 2021.

[11] M. Panahi, R. Jamali, V. F. Rad, M. Khorasani, A. Darudi, and A. R. Moradi, "3D monitoring of the surface slippage effect on micro-particle sedimentation by digital holographic microscopy," *Scientific Reports*, vol. 11, no. 1, pp. 1–11, 2021.

[12] B. Javidi and D. Kim, "Three-dimensional-object recognition by use of single-exposure on-axis digital holography," *Optics Letters*, vol. 30, no. 3, pp. 236–238, 2005.

[13] B. Javidi, *Optical and Digital Techniques for Information Security*, Springer Science & Business Media, Berlin, Germany, 2005.

[14] A. Nelleri, J. Joseph, and K. Singh, "Lensless complex data encoding for digital holographic whole information security," *Optical Engineering*, vol. 47, no. 11, Article ID 115801, 2008.

[15] N. Yoshikawa and T. Miyake, "Omnidirectional 3D shape measurement using image outlines reconstructed from gabor digital holography," https://papers.ssrn.com/sol3/papers.cfm?abstract_id=4075081.

[16] B. Lokesh Reddy, P. Ramachandran, and A. Nelleri, "Compressive complex wave retrieval from a single off-axis digital Fresnel hologram for quantitative phase imaging and microlens characterization," *Optics Communications*, vol. 478, Article ID 126371, 2021.

[17] L. R. Bodi, P. Ramachandran, and A. Nelleri, "Optimal Fresnelet sparsification for compressive complex wave

retrieval from an off-axis digital Fresnel hologram," *Optical Engineering*, vol. 60, no. 7, Article ID 073102, 2021.

[18] V. S. V. Allaparthi, A. Vishnoi, and G. Rajshekhar, "Phase derivative estimation in digital holographic interferometry using deep," *Applied Optics*, vol. 4, 2022.

[19] K. S. Vengala, N. Paluru, and R. K. S. Subrahmanyam Gorthi, "3D deformation measurement in digital holographic interferometry using a multitask deep learning architecture," *Journal of the Optical Society of America A*, vol. 39, no. 1, pp. 167–176, 2022.

[20] E. J. Candès, "Compressive sampling," in *Proceedings of the International Congress of Mathematicians*, Madrid, Spain, 2006, https://doi.org/10.4171/022-3/69.

[21] D. L. Donoho, "Compressed sensing," *IEEE Transactions on Information Theory*, vol. 52, no. 4, pp. 1289–1306, 2006.

[22] E. Candès and J. Romberg, "Sparsity and incoherence in compressive sampling," *Inverse Problems*, vol. 23, no. 3, 2007.

[23] E. J. Candes and M. B. Wakin, "An introduction to compressive sampling," *IEEE Signal Processing Magazine*, vol. 25, no. 2, 2008.

[24] L. I. Chengbo, W. Yin, and Z. Yin, "TV minimization by augmented Lagrangian and alternating direction algorithms," 2009, https://www.caam.rice.edu/%7Eoptimization/L1/TVAL3/v.beta/User_Guide_beta2.4.pdf.

[25] J. M. Bioucas-Dias and M. A. T. Figueiredo, "A new TWIST: two-step iterative shrinkage/thresholding algorithms for image restoration," *IEEE Transactions on Image Processing*, vol. 16, no. 12, pp. 2992–3004, 2007.

[26] G. Unnikrishnan, J. Joseph, and K. Singh, "Optical encryption by double-random phase encoding in the fractional Fourier domain," *Optics Letters*, vol. 25, no. 12, pp. 887–889, 2000.

[27] G. Situ and J. Zhang, "Double random-phase encoding in the Fresnel domain," *Optics Letters*, vol. 29, no. 14, pp. 1584–1586, 2004.

[28] D. S. Monaghan, G. Situ, U. Gopinathan, T. J. Naughton, and J. T. Sheridan, "Role of phase key in the double random phase encoding technique: an error analysis," *Applied Optics*, vol. 47, no. 21, pp. 3808–3816, 2008.

[29] A. Nelleri, J. Joseph, and K. Singh, "Error analysis for a lensless in-line digital holographic complex information security system based on double random phase encoding," *Optics and Lasers in Engineering*, vol. 47, 2009.

[30] S. K. Rajput and N. K. Nishchal, "Known-plaintext attack-based optical cryptosystem using phase-truncated Fresnel transform," *Applied Optics*, vol. 52, no. 4, pp. 871–878, 2013.

[31] G. Li, W. Yang, D. Li, and G. Situ, "Cyphertext-only attack on the double random-phase encryption: experimental demonstration," *Optics Express*, vol. 25, no. 8, pp. 8690–8697, 2017.

[32] J. Li, T. Zheng, Q.-Z Liu, and R. Li, "Double-image encryption on joint transform correlator using two-step-only quadrature phase-shifting digital holography," *Optics Communications*, vol. 285, no. 7, pp. 1704–1709, 2012.

[33] D. Kumar and N. K. Nishchal, "Digital holography based three-dimensional object recognition using binary differential joint transform correlator," in *Proceedings of the 12th International Conference on Fiber Optics and Photonics*, Washington, DC, USA, 2014.

[34] P. Clemente, V. Durán, E. Tajahuerce, V. Torres-Company, R. Martínez-Cuenca, and J. Lancis, *Digital Holography by Ghost Imaging*, Optica Publishing Group, Washington, DC, USA, 2011.

[35] A. Nelleri, "Digital Fresnel field encryption for three-dimensional information security," *Optical Engineering*, vol. 46, no. 4, Article ID 045801, 2007.

[36] S. K. Rajput and N. K. Nishchal, "Fresnel domain nonlinear optical image encryption scheme based on Gerchberg-Saxton phase-retrieval algorithm," *Applied Optics*, vol. 53, no. 3, pp. 418–425, 2014.

[37] B. Hennelly and J. T. Sheridan, "Optical image encryption by random shifting in fractional Fourier domains," *Optics Letters*, vol. 28, no. 4, pp. 269–271, 2003.

[38] N. K. Nishchal, J. Joseph, and K. Singh, "Securing information using fractional Fourier transform in digital holography," *Optics Communications*, vol. 235, no. 4–6, pp. 253–259, 2004.

[39] N. K. Nishchal, J. Joseph, and K. Singh, "Fully phase-based encryption using fractional order Fourier domain random phase encoding: error analysis," *Optical Engineering*, vol. 43, no. 10, p. 2266, 2004.

[40] S. K. Rajput and N. K. Nishchal, "Image encryption based on interference that uses fractional Fourier domain asymmetric keys," *Applied Optics*, vol. 51, no. 10, pp. 1446–1452, 2012.

[41] M. F. Duarte, M. A. Davenport, D. Takhar et al., "Single-pixel imaging via compressive sampling," *IEEE Signal Processing Magazine*, vol. 25, no. 2, pp. 83–91, 2008.

[42] M. N. Kulakov, R. S. Starikov, and P. A. Cheremkhin, "Objects reconstruction by compressive sensing from single-pixel registrations using DMD," *KNE Energy*, vol. 3, no. 3, pp. 509–522, 2018.

[43] Y. Bromberg, O. Katz, and Y. Silberberg, "Ghost imaging with a single detector," *Physical Review*, vol. 79, no. 5, Article ID 053840, 2009.

[44] H. Di, K. Zheng, X. Zhang et al., "Multiple-image encryption by compressive holography," *Applied Optics*, vol. 51, no. 7, pp. 1000–1009, 2012.

[45] P. Clemente, V. Durán, E. Tajahuerce, P. Andrés, V. Climent, and J. Lancis, "Compressive holography with a single-pixel detector," *Optics Letters*, vol. 38, no. 14, pp. 2524–2527, 2013.

[46] J. Li, J. Sheng Li, Y. Yang Pan, and R. Li, "Compressive optical image encryption," *Scientific Reports*, vol. 5, no. 1, Article ID 10374, 2015.

[47] L. Jun, B. Jia, X. Dai et al., "Compressive optical image encryption using phase-shifting interferometry on a joint transform correlator," *Optica Applicata*, vol. 47, 2017.

[48] Z. Leihong, X. Rui, Z. Dawei, and C. Jian, "Optical encryption based on the algorithm of compressive ghost imaging and phase-shifting digital holography," *Ukrainian Journal of Physical Optics*, vol. 19, no. 3, pp. 179–190, 2018.

[49] Y. Wang, Q. Liu, J. Wang, and Q.-H. Wang, "Optical encryption of multiple three-dimensional objects based on multiple interferences and single-pixel digital holography," *Chinese Physics B*, vol. 27, no. 3, Article ID 034202, 2018.

[50] J. Du, Y. Xiong, C. Wu, and C. Quan, "Optical image encryption with high efficiency based on variable-distance ghost imaging," *Optik*, vol. 252, Article ID 168484, 2021.

[51] P. Zheng, Q. Dai, Z. Li et al., "Metasurface-based key for computational imaging encryption," *Science Advances*, vol. 7, no. 21, Article ID eabg0363, 2021.

[52] S. Jiao, J. Feng, Y. Gao, T. Lei, and X. Yuan, "Visual cryptography in single-pixel imaging," *Optics Express*, vol. 28, no. 5, pp. 7301–7313, 2020.

[53] C. Zhang, B. Han, W. He, X. Peng, and C. Xu, "A novel compressive optical encryption via single-pixel imaging," *IEEE Photonics Journal*, vol. 11, no. 4, pp. 1–8, 2019.

[54] Y. Awatsuji, M. Sasada, and T. Kubota, "Parallel quasi-phase-shifting digital holography," *Applied Physics Letters*, vol. 85, no. 6, pp. 1069–1071, 2004.

[55] Y. Awatsuji, T. Tahara, A. Kaneko et al., "Parallel two-step phase-shifting digital holography," *Applied Optics*, vol. 47, no. 19, pp. D183–D189, 2008.
[56] T. Tahara, K. Ito, T. Kakue et al., "Parallel phase-shifting digital holographic microscopy," *Biomedical Optics Express*, vol. 1, no. 2, pp. 610–616, 2010.
[57] J. E. Rueda-Parada and J. Enrique, "Encryption using circular harmonic key," *Dyna*, vol. 82, no. 190, pp. 70–73, 2015.
[58] Q. Wang, Q. Guo, L. Lei, and J. Zhou, "Optical interference-based image encryption using circular harmonic expansion and spherical illumination in gyrator transform domain," *Optics Communications*, vol. 346, pp. 124–132, 2015.
[59] B. Lokesh Reddy and A. Nelleri, "Complex object wave retrieval using single-pixel compressive imaging of an off-axis Fresnel hologram," *Journal of Modern Optics*, vol. 69, no. 10, pp. 541–553, 2022.
[60] P. Ramachandran, Z. C. Alex, and A. Nelleri, "Phase reconstruction using compressive two-step parallel phase-shifting digital holography," *Optical Engineering*, vol. 57, no. 4, Article ID 043105, 2018.

Hindawi
International Journal of Optics
Volume 2022, Article ID 3790494, 11 pages
https://doi.org/10.1155/2022/3790494

Research Article

Three-Dimensional Reconstruction of Rolling Contact Fatigue Characteristics

Chengkai Zeng, Gaopeng Xu, Hai Li, Gang Zhu, and Yan Yang

College of Mechanical Engineering, Chongqing University of Technology, 69 Hongguang Ave, Chongqing 40005, China

Correspondence should be addressed to Yan Yang; yangyan@cqut.edu.cn

Received 25 October 2021; Revised 30 December 2021; Accepted 31 December 2021; Published 24 January 2022

Academic Editor: Xiaowei Li

Focusing on the 3D topographic characteristics of rolling contact fatigue, a reconstruction method of the fatigue surface of roller based on point cloud data was proposed in this research. A 3D laser scanner was used to capture the data of point cloud on the surface of the fatigue roller. The gradient segmentation method was used to achieve segmentation of the fatigue contact surface, and the Kd-Tree algorithm in Statistical Outlier Removal filter was adopted to remove different types of noise. The greedy triangulation and hole repair and reconstruction of the curled point cloud were conducted. The experimental results showed that the segmentation accuracy of the fatigue contact surface was above 97.7%, the curling error rate of point cloud was 0.09%, and the maximum deviation of the reconstructed fatigue roller surface was 0.0199 mm. These methods can be applied to analyze the working conditions of roller specimen and contact fatigue.

1. Introduction

Contact fatigue is a kind of surface fatigue damage phenomenon in which the contact surface of contact material forms pits with the influence of long-term cyclic contact stress [1, 2]. In engineering fields, such as machinery, vehicles, ships, and aviation, some parts under rolling contact conditions, such as rolling bearings, shafts, cams, and gears, which often fail due to contact fatigue, are frequently used [3, 4]. According to statistics, 80% to 95% of mechanical failures were the results of metal fatigue. The annual GDP loss is as high as 4% worldwide [5–7]. Hence, accurate acquisition of the contact fatigue performance parameters of metal materials is of great significance to prevent contact fatigue accidents [8, 9]. In addition, methods to determine fatigue failure in the fatigue contact test are mainly realized through human eye observation, vibration signal, temperature signal, friction torque signal analysis, and acoustic emission detection [10–12]. The direct detection method is manual visual detection. The rest are the indirect detection method. Although they are widely used at present, they all are unable to quantify the problem of fatigue pitting defect information and visualize issues, such as fatigue status.

In order to obtain the capability to detect and identify the fatigue defects of parts in real time and in an accurate manner, the machine vision-based detection technology has been introduced for the rolling contact fatigue test. Sun et al. [13] made use of neighborhood weighted segmentation to extract surface defects and detected camshaft surface defects, which has been a success. Xie et al. [14] came up with an algorithm to extract key parameters of carrot surface defects based on machine vision. In this case, carrot surface defect detection and online classification have been realized. Nirbhar et al. [15] came up with a global adaptive threshold method based on gradient images to detect steel surface defects. Given that this method failed to pay sufficient attention to the local features of the image during the threshold selection process, the edges of some defects were not correctly identified. In addition, an improved Otsu algorithm based on automatic weighted threshold proposed by Xu et al. [16] can achieve a good segmentation of rolling contact fatigue defect detection. The above detection methods only detect the surface defects of the workpiece in two dimensions, without detecting important information such as the three-dimensional shape of the defect, or

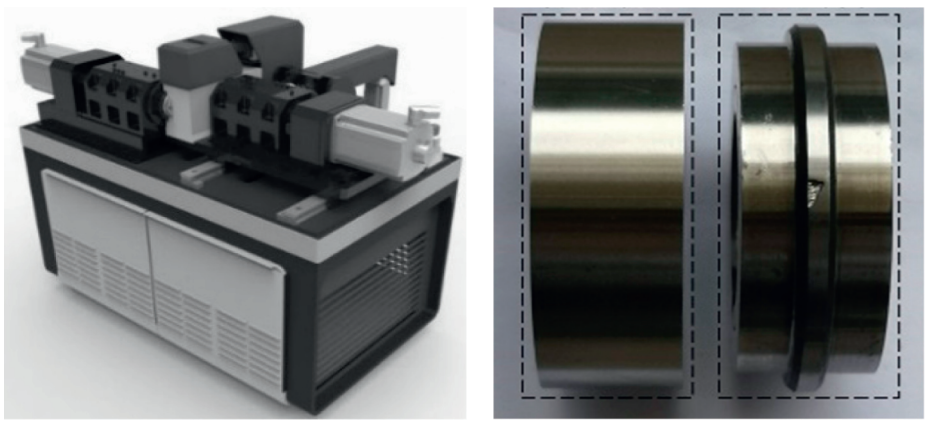

(a) (b)

Figure 1: Test equipment and samples. (a) Contact fatigue testing machine and (b) main specimen and companion specimen.

visualize the defects. Certainly, these methods have limitations.

The 3D reconstruction technology based on machine vision features high accuracy, good real time performance, and fast speed [17, 18]. Scholars at home and abroad have performed extensive research on it. Although the 3D reconstruction technology based on machine vision has been widely used in various fields, there is no research on its application in rolling contact fatigue test. The 3D reconstruction technology in other fields can be used as references. Snavely et al. [19] developed an interactive 3D reconstruction system. The system is able to automatically calculate the viewpoint of each photo and the sparse model between the scene and the image. Nonetheless, the reconstruction effect is not clear enough and the degree of visualization is low, which are the disadvantages. Furukawa et al. [20] proposed a method to obtain a complex 3D model from multiple calibrated pictures. Microsoft Research launched the Kinect Fusion project [21], in which the Kinect sensor was used for the sake of acquiring the depth image data of the scene in multiple directions, and reconstructing the 3D model of the scene in real time. Microsoft Research announced the Mobile Fusion project [22] to collect data through the mobile phone RGB camera. Also, reconstruction technology can be used to complete the reconstruction of the target object. In the current rolling contact fatigue test, the acquired fatigue pitting defect information is not perfect. Problems such as the inability to visualize the fatigue pitting corrosion state and display the three-dimensional morphological characteristics of the sample after failure are both important issues.

A method of 3D topography reconstruction of the fatigue roller surface based on point cloud data was conducted for the sake of resolving the problems above. The method in the present study is based on point cloud data and researches the processing algorithm of 3D point cloud data. A denoising algorithm for the fatigue roller surface point cloud based on conditions and statistics was designed aiming at the different types of noise in the roller surface point cloud data. The algorithm can improve the quality of the point cloud. In order to realize the reconstruction of the three-dimensional topography of the fatigue roller surface, this paper studies the 3D reconstruction algorithm, which can visualize the three-dimensional topography of the failure surface of the roller sample. Then the experimental results of the three-dimensional shape reconstruction of the roller sample are illustrated and analyzed. Some discussions and conclusions are given finally.

2. Fatigue Test System

Figure 1(a) shows the contact fatigue testing machine developed by our research group. It collected sample surface information in real time through the image acquisition system. Figure 1(b) shows the original image of the sample. Then the collected images have been analyzed after computer processing. After that, users may determine whether the sample has fatigue failure according to the result. The machine will be shut down immediately when the fatigue goes beyond the standard. This machine made use of 2D image area to judge failure. In addition, the 3D topographic characteristics of rolling contact fatigue are an urgent need as per the deep research on the failure.

3. Methods

3.1. Data Collection and Preprocessing

3.1.1. Point Cloud Data Acquisition. In recent years, 3D laser scanning technology has developed rapidly. 3D reconstruction based on point cloud data has long become a hot and thought-provoking research topic [23–25]. The 3D laser scanning technology made use of noncontact active measurement method to collect point cloud data, which has the characteristics of strong real time, fast scanning speed, and high precision. For the rolling contact fatigue test, in the present study, the fatigue failure of the roller specimen was taken as the research object. The Gocator2420 laser scanners produced by the LMI Technologies company (LMI) was used to obtain the three-dimensional information of the fatigue roller surface. The intact and defect-free standard roller surface were firstly used as the reference surface before

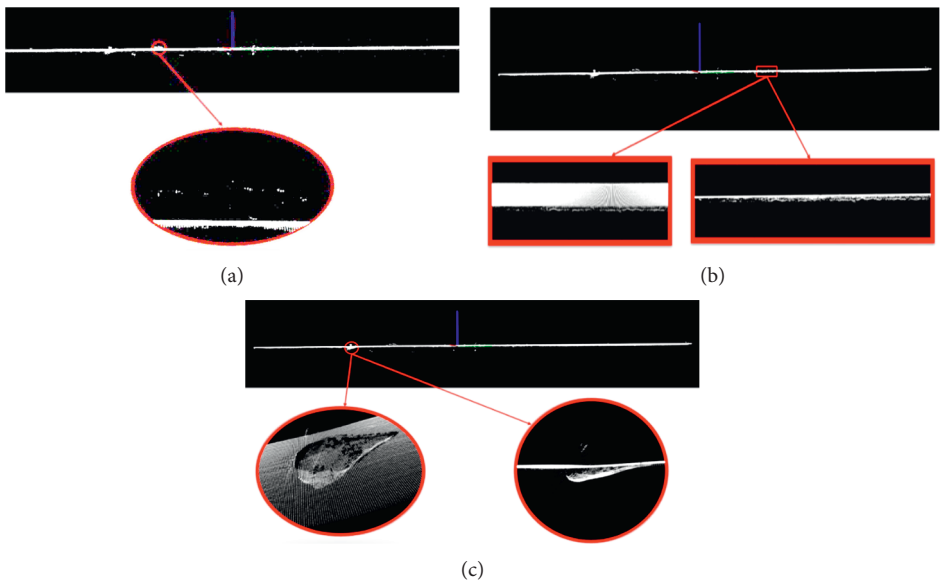

Figure 2: Types of noise points on the surface of fatigue rollers. (a) *YZ* plane view of isolated point, (b) different angle views of noise on the chamfered edge, and (c) different angle views of outlier noise.

acquiring the point cloud data. After that, the Z-direction zero value was calibrated via the software equipped with the laser sensor. Then the external encoder pulse signal was used at appropriate speed to trigger the laser scanner and scan the surface of the test piece. Finally, the original point cloud image of the test piece was obtained.

3.1.2. Data Preprocessing

Fatigue Contact Surface Segmentation. High accuracy of the Gocator laser scanner contributes to large amount of point cloud data acquired. Too much point cloud data tends to reduce the operating speed of the computer. Therefore, it is necessary to segment the point cloud of the fatigue contact surface from the acquired point cloud data. It can be found that the roller boss part is the fatigue contact surface upon the analysis of the roller structure and the original data. Also, the fatigue contact surface point cloud and the nonfatigue contact surface point cloud in the point cloud data obtained are not in the same plane, but in the Z-axis direction. Besides, a certain gradient is present, which is shown in Figure 1. Hence, this present study made use of gradient segmentation [26] to extract the point cloud data of fatigue contact surface. Given that the origin of the point cloud is at the center of the original point cloud, the X coordinates of the points where the Z-direction coordinate changes on the original point cloud graph were counted respectively. Also, the average values of the X coordinates of these sudden changes were calculated respectively as the upper and lower thresholds of the gradient segmentation. The expression of the gradient segmentation function to extract the point cloud data of the fatigue contact surface is

$$ds\ t(x, y, z) = \begin{cases} \mathrm{src}(x, y, z), & t \le x \le T, \\ 0, & \text{otherwise}, \end{cases} \quad (1)$$

where $\mathrm{src}(x, y, z)$ is the original coordinate of the point cloud and t and T are the upper and lower thresholds of gradient segmentation, respectively.

Point Cloud Denoising. The above method was used to segment and extract the obtained fatigue roller surface point cloud data. However, some noises can still be heard in the extracted roller fatigue contact surface point cloud owing to the influence of equipment and external environmental factors, such as light, vibration, and occlusion. These factors have been proven to be able to affect the segmentation and extraction of point cloud data and reduce the quality of point cloud. According to the analysis of the obtained point cloud image of the fatigue roller surface, it has been found that these noises mainly exist in three types: solitary points, chamfer edge noise, and outlier noise, as shown in Figures 2(a)–2(c).

In the present research, after analyzing the types of noise points on the point cloud on the surface of the fatigue roller, a set of denoising algorithms was designed specifically for the point cloud on fatigue roller surface. After that, a standard roller sample was further used as a calibration part to calibrate the measurement system before obtaining the point cloud data. The removal of different types of noise on the surface of the fatigue roller has been achieved through a combination of conditions and statistics. Among them, for isolated points and chamfer edge noise, the value of the point cloud coordinate axis direction is used as the judgment condition by setting corresponding conditions, thus realizing the removal of these two types of noise.

For outlier noise points, the average distance from each point to its neighbors is counted. In addition, the result approximately conformed to the Gaussian distribution. The distribution of adjacent point clouds shows a feature of symmetry and uniformity. The probability density function is

$$f(x_i) = \frac{1}{\sqrt{2\pi}\sigma}\exp\left(-\frac{(x_i-\mu)^2}{2\sigma^2}\right), \quad (i = 1, 2, 3, \ldots), \tag{2}$$

where x_i is the average distance of the neighborhood of any point, μ is the mean value of the average distance of the neighborhood, and σ is the standard deviation.

Given that outlier noise features uneven density and relatively sparse property, the calculation of the distance distribution from one point to its adjacent point in the input data can be used to eliminate the noise. Hence, the Kd-Tree algorithm in the Statistical Outlier Removal filter [27] was used to remove outlier noise. First traverse the point cloud and find the K adjacent points corresponding to each point $P_i(x_i, y_i, z_i)$ $(i = 1, 2, \ldots, n)$. For each point, calculate the average distance from it to all its adjacent points; remove the points with the average distance from K adjacent points exceeding the standard range D, $D = \mu \pm \alpha\sigma$, and α is a constant, which is a multiple of the standard deviation.The average distance d_i, mean μ, and the calculation expression of standard deviation σ is

$$\begin{aligned} d_i &= \frac{1}{k}\sum_{j=1}^{k}\sqrt{(x_i-x_j)^2+(y_i-y_j)^2+(z_i-z_j)^2}, \\ \mu &= \sum_{i=1}^{n}\frac{1}{n}d_i, \sigma = \sqrt{\frac{1}{n}\sum_{i=1}^{n}(d_i-\mu)^2}. \end{aligned} \tag{3}$$

3.2. 3D Reconstruction of the Fatigue Roller Surface

3.2.1. Point Cloud Curling. Given that the test piece is a rotating body roller specimen, point cloud crimping was come up with to make the reconstruction result consistent with the original specimen shape:

(1) Find the curl radius R: first, obtain the point with the largest absolute value of the coordinate in the Y-axis direction of the point cloud according to the input point cloud image. This point is the end point of the input point cloud image. Since the coordinate origin of the input point cloud image is at the center of the point cloud image, the Y coordinate value of the end point is half the circumference of the point cloud, so the radius R after rolling up is obtained.

(2) Find the radian: take the point cloud coordinate origin O as the starting point of the first curl, find the radian value α_i corresponding to the arc length from any point $P_i(x_i, y_i, z_i)$ $(i = 1, 2, \ldots, n)$ to this point, and find the sine $\sin\alpha_i$ and cosines $\cos\alpha_i$ corresponding to the angle, where $\alpha_i = (L_i/R)$, $(i = 1, 2, \ldots, n)$.

(3) Find the center of the curling circle: take the point O and let it be perpendicular to the XY plane, with the point with a length of R as the center of the first curling circle. The obtained center coordinates are the X and Y coordinates of the origin point cloud. Add R to the coordinate value.

(4) Point cloud curling: the curling process is actually the process of point cloud coordinates changing. Take the first circle of curling as an example, where the X coordinate of each point remains unchanged. The Y coordinate of each point is the curl radius plus the distance from each point in the Z direction to the starting point in the Z direction, multiplied by its sine value, and finally the center coordinate Y value is added. The Z coordinate of each point is the curl radius plus the distance from the Z direction of each point to the Z direction of the starting point, multiplied by the cosine value, and finally the center coordinate Z value, thus completing a circle of point cloud curling.

(5) Change the coordinates of the center of the circle, traverse all the points, then repeat step (4). In this way, the point cloud would be curled.

3.2.2. Point Cloud Gridding. The current surface reconstruction methods based on point cloud data are divided into three categories mainly: implicit surface reconstruction [28], parametric surface reconstruction [29], and mesh surface reconstruction [30]. In the present study, the mesh surface reconstruction method based on the greedy algorithm is used to triangulate the preprocessed point cloud to reconstruct the three-dimensional mesh surface of the fatigue roller.

The greedy triangulation algorithm is a fast and efficient method for 3D surface reconstruction. It projects 3D points to the corresponding plane through the normal direction to triangulate, thereby obtaining the topological structure between the original 3D points. The algorithm steps are as follows:

(1) Let the point cloud data set be $Q = \{Q_i, i = 1, 2, 3, \ldots, n\}$. Use k-d tree to establish spatial neighborhood index.

(2) Choose one of the points Q_i as the starting point, and use the point and its k adjacent points to fit the point-domain normal vector N. From the point and the normal vector N, the tangent plane of the point can be obtained.

(3) Project the point Q_i and its k adjacent points on the plane V_1, obtain the original point Q_j corresponding to the nearest point of the point Q_i according to the neighboring relationship of the projected point, and connect with Q_i and Q_j as the starting edge of the triangulation.

(4) Fit the tangent plane from the connection between Q_i and Q_j and the adjacent points to acquire the tangent plane V_2.

(5) Project the adjacent points near the line Q_iQ_j segment onto the plane, then use the Delaunay triangulation method to find the corresponding third original point Q_k, and connect the three points to form the first triangle.

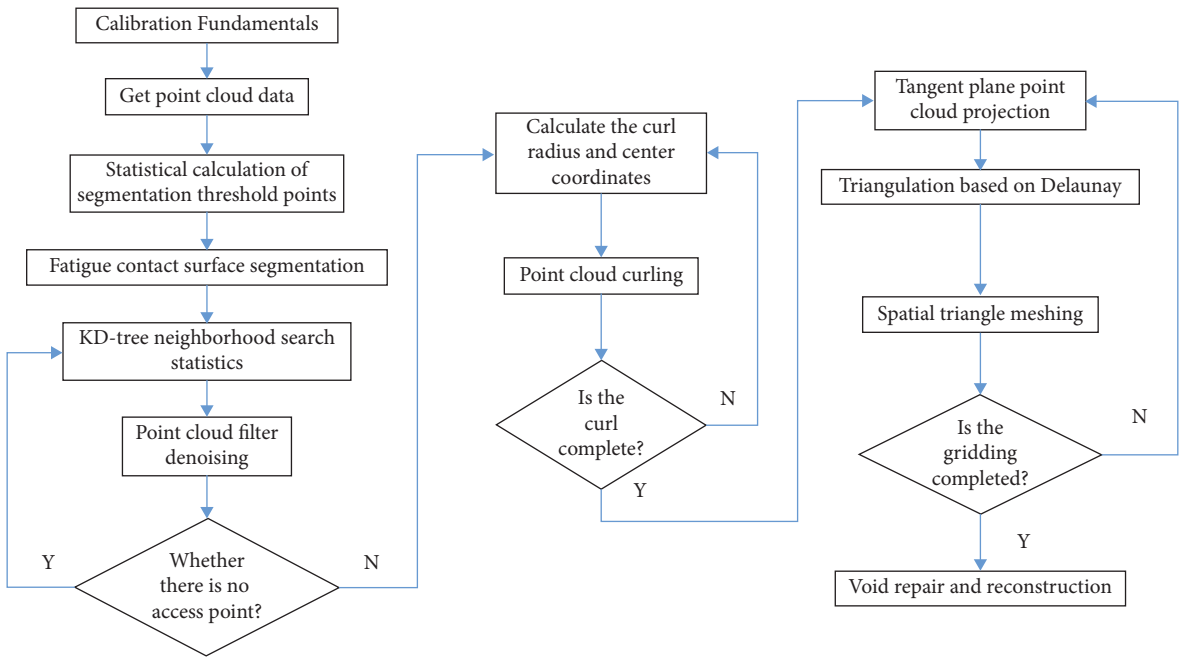

Figure 3: Flow chart of point cloud processing and 3D reconstruction.

(6) The three sides of the first triangle are taken as the starting side, then repeat step (5) to traverse all the spatial points to complete the point cloud gridding.

3.2.3. Point Cloud Hole Repair and Reconstruction. Holes show up in the missing parts of the point cloud data after point cloud gridding. The quality of the reconstruction would be directly affected if these missing areas were not repaired [31]. There are two main types of hole repair methods in 3D reconstruction. One type of methods is the hole repair based on scattered point clouds [32]. The other type is the repair of surface holes based on triangular meshes [33]. To create a surface patch, the hole repair based on scattered point cloud is based on the scattered points at the boundary of the hole. This repair method is suitable for surfaces with small curvature changes, while the surface hole repair based on triangular meshes tends to present more uniform distribution of point clouds. The curved surface has a remarkable effect. The repair has been implemented in the present study Geomagic Studio software. The repair and reconstruction process mainly uses meshing to find the boundary of the hole and fill the hole based on the curvature. According to the reconstruction results, the shape characteristics of the roller fatigue contact surface have been soundly maintained, marking an important support for analyzing the contact fatigue performance of the roller specimen under simulated working conditions.

4. Results and Discussion

4.1. Test Conditions. In order to verify the point cloud processing method and reconstruction effect for rolling contact fatigue rollers proposed in the present study, 4 types of fatigue rollers with different widths and different fatigue effects were selected for experimental tests. The test process is to install VS2015 on a PC with 3.2 GHz processor and 8 GB memory and, on this basis, configure the PCL1.8.0 environment. The overall flow chart of point cloud processing and 3D reconstruction are shown in Figure 3.

4.2. Denoising Results of Point Cloud on the Fatigue Roller Surface. The choice of the value of k and α will directly affect the denoising effect. If the selected value of k is too large or the value of α is too small, the denoising would be prone to becoming excessive denoising. If the selected value of k is too small and the value of α is too large, the denoising effect will not be good. This paper uses many different experiments to determine the appropriate value of k and α. The denoising effect tends to be better as the k value is selected in the range of 20–40. Similarly, when the α value is selected in the range of 1–3, the denoising effect is better. The experimental pictures are shown in Figure 4 in the range of k and α. Table 1 shows the experimental data. In addition, according to the effect of these pictures, when $k = 40$, $\alpha = 1$, part of the point cloud at the pitting defect is regarded as the excessive point. When $k = 20$, $\alpha = 3$, the noise at the pitting defect is not completely removed, and there are still noises at the position of the yellow circle in the picture. The denoising results of point cloud on fatigue roller surface show up as $k = 30$ and $\alpha = 2$.

The point cloud of the four types of fatigue roller contact surface after segmentation is shown in Figures 5(a), 6(a), 7(a), and 8(a). By means of the condition and statistics-based method of denoising the point cloud of the fatigue roller surface in the present study, the noise points in the point cloud have undergone denoising experiments. The experimental results are shown in Figures 5(b), 6(b), 7(b), and 8(b).

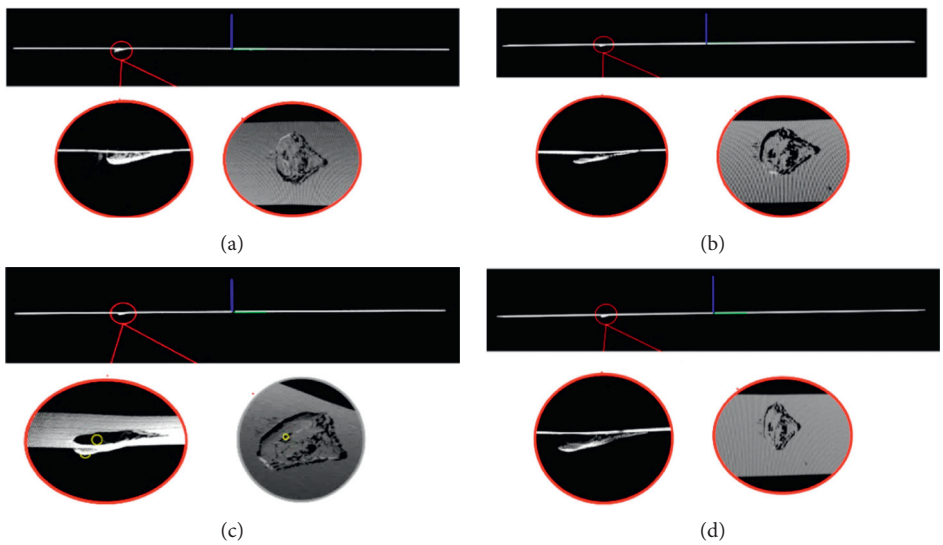

Figure 4: Denoising effect of discrete noise on the contact surface of fatigue roller with different parameters. (a) Discrete noise map of fatigue roller contact surface; (b) denoising effect picture when $k = 40$ and $\alpha = 1$; (c) denoising effect picture when $k = 20$ and $\alpha = 3$; and (d) denoising effect picture when $k = 30$ and $\alpha = 2$.

Table 1: Comparison of noise reduction with different K values and α values.

K	α	Number of point clouds after denoising/piece	Denoising ratio/%
40	1	871872	3.231
40	2	883319	1.961
40	3	892701	0.920
30	1	872010	3.216
30	2	885705	1.695
30	3	892694	0.920
20	1	879655	0.236
20	2	889049	0.132
20	3	894426	0.072

The number of point clouds before denoising is 900991/piece.

For the denoising algorithm in the present study, the confusion matrix method is used to calculate the accuracy rate P and the recall rate R of the experimental results to evaluate the effectiveness of the denoising algorithm. The precision rate P represents the accuracy of the prediction in the result of the positive sample, and the recall rate R measures the classifier's ability to recognize positive examples. Among them, TP means that the positive class is judged to be a positive class, and the positive class here is a nonnoise point. FP means that the negative class is judged to be a positive class. FN means that the positive class is judged to be a negative class. TN is judged to be a negative class.

$$P = \frac{\mathrm{TP}}{\mathrm{TP} + \mathrm{FP}} \times 100\%,$$
$$R = \frac{\mathrm{TP}}{\mathrm{TP} + \mathrm{FN}} \times 100\%. \tag{4}$$

It can be found that after denoising the fatigue roller contact surface point cloud by using the method in the present study, the isolated points, chamfer edge noise, and outlier noise in the fatigue roller contact surface point cloud are effectively removed. After comparing the point cloud images of different types of fatigue roller contact surface before and after denoising, it can be found that the point cloud of the fatigue roller contact surface after denoising maintains the basic characteristics of the point cloud model.

In order to compare with traditional denoising algorithms, this paper uses conditional denoising and statistical denoising methods to carry out denoising experiments on the contact surface of the fatigue roller. Table 2 shows the accuracy rate P and the recall rate R calculated by using the conditional denoising and statistical denoising algorithms, respectively. Figure 9 is the comparative effect diagram of a fatigue roller with a contact surface width of 4 mm after using conditional denoising and statistical denoising.

Upon comparison of Tables 2 and 3, the precision rate P and the recall rate R in the conditional denoising or statistical denoising algorithm are lower than those of the fatigue roller surface point cloud denoising algorithm based on conditions and statistics. In addition, according to Figure 9, the solitary point and chamfer edge noise can basically be removed after the conditional denoising of the fatigue roller contact surface. Nonetheless, the noise near the fatigue defect has not been effectively removed, especially the internal separation of the fatigue defect. Group noise still exists. Besides, the outlier noise inside the fatigue defect is effectively removed after using statistical denoising to denoise the point cloud of the fatigue roller contact surface. Notwithstanding, the isolated point and chamfer edge noise have not been removed. In this regard, it has been inferred that the cloud denoising algorithm has a more obvious denoising effect on the point cloud of the fatigue roller contact surface, enhancing the denoising efficiency and laying the foundation for the subsequent 3D topography reconstruction.

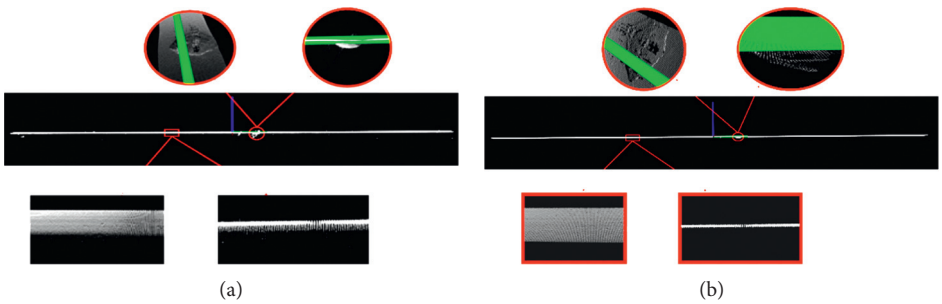

Figure 5: The results of point cloud denoising for the roller with a contact surface width of 4 mm. (a) Point cloud before the denoising roller and (b) point cloud after the denoising roller.

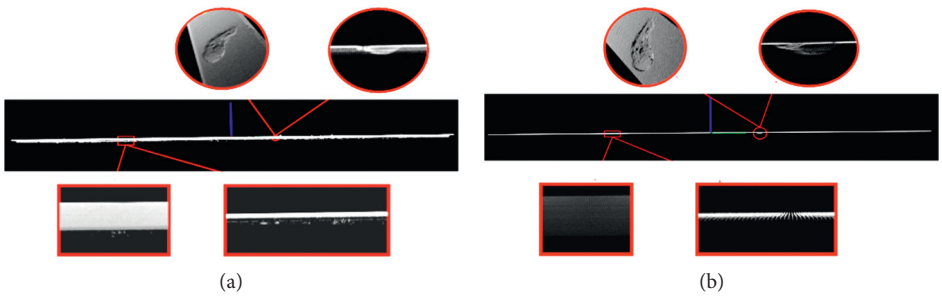

Figure 6: The results of point cloud denoising for the roller with a contact surface width of 5 mm. (a) Point cloud before the denoising roller and (b) point cloud after the denoising roller.

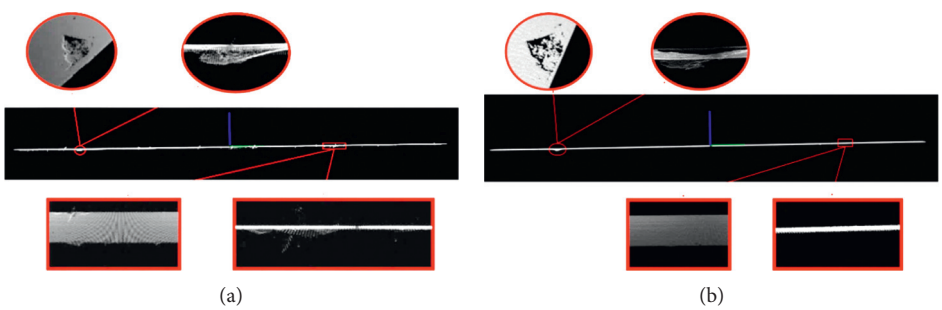

Figure 7: The results of point cloud denoising for the roller with a contact surface width of 6 mm. (a) Point cloud before the denoising roller and (b) point cloud after the denoising roller.

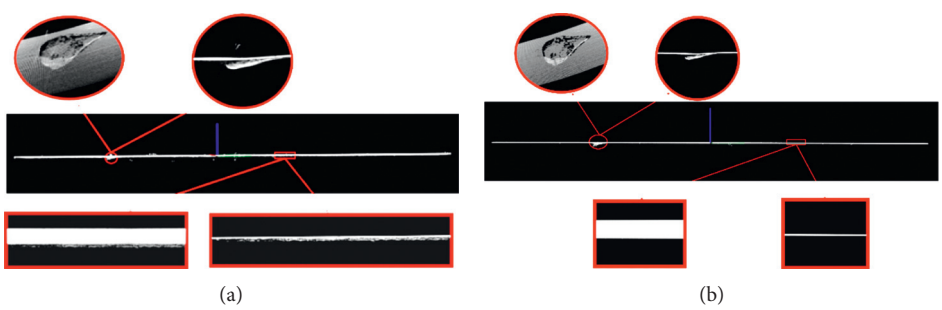

Figure 8: The results of point cloud denoising for the roller with a contact surface width of 10 mm. (a) Point cloud before the denoising roller and (b) point cloud after the denoising roller.

4.3. Reconstruction Verification of the 3D Topography of the Fatigue Roller Surface. The method in the present study was used to test the selected four different rolling contact fatigue rollers. The point cloud models are shown in Figure 10(a), and reconstruction results are shown in Figure 10(b), the deviation analysis of the results of the contact surface

Table 2: Calculation of precision rate P and recall rate R by using conditional denoising or statistical denoising.

Data group	Type	TP	FP	FN	TN	P	R (%)
①	Conditional	810573	1054	10179	280	99.87%	98.76
	Statistical	809714	1185	11038	189	99.85%	98.66
②	Conditional	881565	1528	9853	5891	99.83%	98.89
	Statistical	880870	1835	10548	5584	99.79%	98.82
③	Conditional	1181535	3254	8876	1196	99.73%	99.25
	Statistical	1179126	4025	11285	425	99.66%	99.05
④	Conditional	2014943	2217	14526	7101	99.89%	99.28
	Statistical	2014027	3856	15442	5462	99.81%	99.24
⑤	Conditional	881393	4421	17254	293	99.5%	98.08
	Statistical	878101	4620	20546	94	99.48%	97.71
⑥	Conditional	833937	1115	8896	481	99.87%	98.94
	Statistical	831380	1420	11453	176	99.83%	98.64
⑦	Conditional	908116	3051	12549	2002	99.67%	98.64
	Statistical	907141	1853	13524	3200	99.79%	98.53
⑧	Conditional	791856	2569	11548	1767	99.68%	98.56
	Statistical	788164	2485	15240	1851	99.69%	98.1

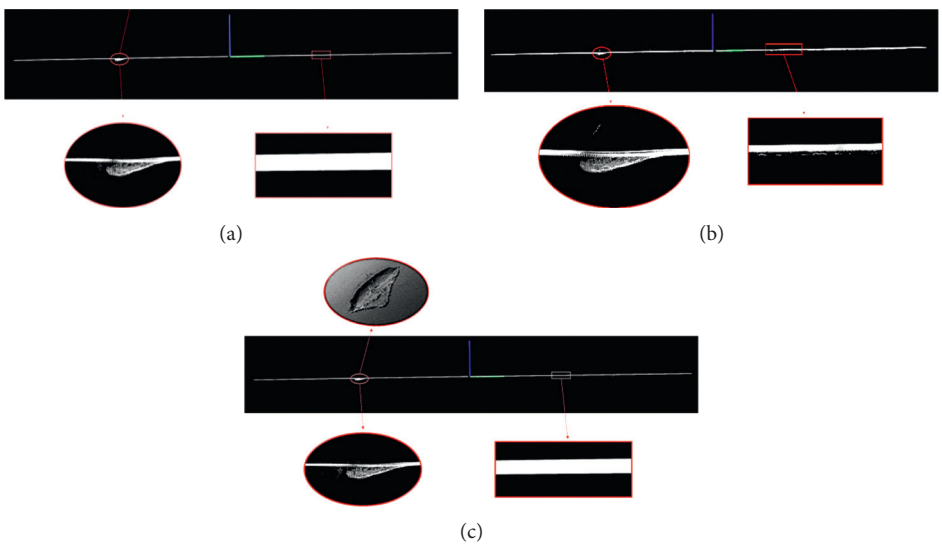

Figure 9: The results of point cloud denoising for roller with the contact surface width of 4 mm. (a) The result by using conditional denoising. (b) The result by using statistical denoising. (c) The result by using the conditional and statistical method.

Table 3: Calculation of precision rate P and recall rate R of the denoising algorithm in the present study.

Data group	TP	FP	FN	TN	P	R (%)
①	820700	72	52	1302	99.99%	99.99
②	891302	50	116	7369	99.99%	99.98
③	1190301	1095	110	3355	99.91%	99.99
④	2029413	72	56	9246	99.99%	99.99
⑤	898578	2656	69	2058	99.71%	99.99
⑥	842751	88	82	1508	99.98%	99.99
⑦	920546	802	119	4251	99.91%	99.98
⑧	803362	510	42	3826	99.94%	99.99

reconstruction of these four types of fatigue rollers were performed, and the results are shown in Figure 10(c). By comparing the model renderings of each roller, the method in the present study can use the three-dimensional point cloud data obtained by scanning to effectively segment the fatigue rollers with different widths and different fatigue effects. In this way, the outlier noise can be removed in a better way. In addition, the curling of the point cloud image was realized, and a high-quality three-dimensional model of the contact surface of the fatigue roller was finally reconstructed.

The result of the comparison of the measured value of the standard fatigue contact surface width with the segmented fatigue contact surface width model value is shown in Figure 11. The root mean square error between the two is 0.0497 mm. According to statistics, the error range of the fatigue contact surface width after segmentation is 0%–2.3%, most of which are between 0 and 1%. The accuracy of the contact surface segmentation model is relatively high, thus

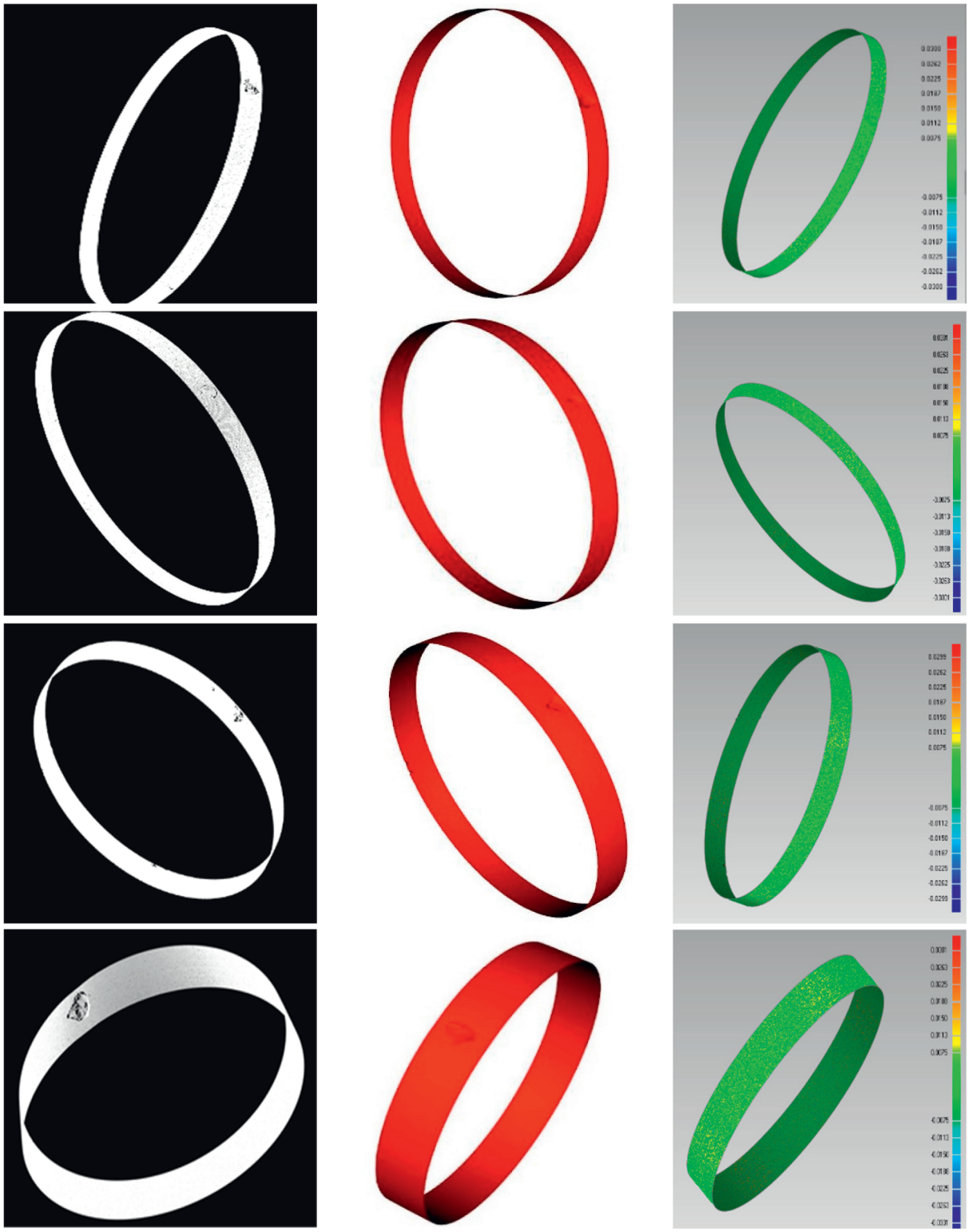

(a) (b) (c)

Figure 10: Point cloud reconstruction and deviation diagram of different fatigue roller contact surfaces. (a) Point cloud before reconstruction of different roller contact surfaces, (b) reconstruction results of different roller contact surfaces, and (c) reconstruction deviation diagram of different roller contact surface.

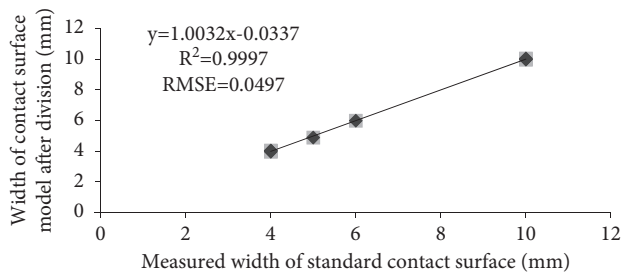

Figure 11: Accuracy analysis of the segmentation model of the fatigue roller contact surface.

directly reflecting the segmentation accuracy of the fatigue roller contact surface. According to the point cloud denoising method and the denoising model, as $K = 30$, $\alpha = 2$, the outlier noise removal effect tends to be the best. It can effectively remove the outlier noise for different fatigue rollers. Statistics of the number of point clouds before and after curling found that the number of point clouds after curling is exactly the same as the number of point clouds after denoising. It has proven that all points are curled, the radius of the point cloud after curling is 29.97 mm, the curling error rate is 0.09%, and the crimping accuracy is higher. In addition, the analysis results of the deviations of these types of fatigue rollers after reconstruction showed that the maximum deviation is 0.0199 mm. The method in the present study can reconstruct the morphological characteristics of the fatigue rollers well.

5. Conclusions

A 3D reconstruction method for fatigue roller specimens based on point cloud data was proposed in this present study. In this 3D reconstruction method, the point cloud data of the roller specimen was collected after fatigue failure through a three-dimensional laser scanner, and then the average X coordinate of the point where the Z-axis coordinate changes on the original point cloud image were counted as the point cloud segmentation threshold. Then, the fatigue contact of the roller surface point cloud was segmented, and filtering and denoising preprocessing was conducted on the segmented point cloud. In addition, the point cloud was crimped for the sake of driving the reconstructed 3D model consistent with the actual roller specimen. In the end, the crimped point cloud was greedily triangulated and hole repaired and reconstructed, thereby obtaining high-quality fatigue. Besides, 3D mesh model of the roller surface was used. This method has the following advantages:

(1) The method proposed in the present study is based on real 3D point cloud data. Hence, the reconstructed 3D model can truly reflect the 3D topography of the roller after fatigue failure.

(2) The point cloud curling method proposed in the study is also capable of effectively transforming the flat point cloud image into the point cloud image of the revolving body. In this way, the reconstructed 3D model is consistent with the actual roller shape.

(3) The point cloud data was processed by gridding, and the gridded 3D model was optimized for hole repair to realize the 3D reconstruction of the surface of the roller specimen after failure and effectively retain the shape of the failure surface. These characteristics provide a reliable basis for the later analysis of contact fatigue performance of the roller specimen under the simulated working conditions.

Data Availability

No data were used to support this study.

Conflicts of Interest

The authors declare that they have no conflicts of interest.

Authors' Contributions

Conceptualization was done by Chengkai Zeng; data curation was carried out by Chengkai Zeng and Gaopeng Xu; formal analysis was performed by Chengkai Zeng; funding acquisition was done by Yan Yang; methodology was prepared by Chengkai Zeng; supervision was done by Yan Yang; validation was carried out by Gaopeng Xu and Gang Zhu; visualization was done by Hai Li; writing of the original draft was carried out by Chengkai Zeng; review and editing were conducted by Yan Yang.

Acknowledgments

This research was funded by the National Natural Science Foundation of China (52075062 and 51875068) and by the National Key Research and Development Program of China (2020YFB2010103).

References

[1] M. Kalin and J. Vižintin, "A rolling-contact device that uses the ball-on-flat testing principle," *Wear*, vol. 256, no. 3-4, pp. 335–341, 2004.

[2] S. W. A. Dekker, "Robert long, jean-luc wybo zero vision and a western salvation narrative," *Safety Science*, vol. 88, 2016.

[3] V. Manoj, K. Manohar Shenoy, and K. Gopinath, "Developmental studies on rolling contact fatigue test rig," *Wear*, vol. 264, pp. 708–718, 2008.

[4] M. Endo, S. Okazaki, H. Matsunaga et al., "A new fatigue testing machine for investigating the behavior of small shear-mode fatigue cracks," *Experimental Techniques*, vol. 40, no. 3, pp. 1065–1073, 2015.

[5] M. Fujii, A. Yoshida, and J. B. Ma, "Rolling contact fatigue of alumina ceramics sprayed on steel roller under pure rolling contact condition," *Tribology International*, vol. 39, pp. 856–862, 2006.

[6] W McIlhagga, "Estimates of edge detection filters in human vision," *Vision Research*, vol. 153, pp. 30–36, 2018.

[7] O. Celik and F. Chuan-Zhi Dong, "Necati Catbas A computer vision approach for the load time history estimation of lively individuals and crowds," *Computers & Structures*, vol. 200, 2018.

[8] A. Borji, "Negative results in computer vision: a perspective," *Image and Vision Computing*, vol. 69, 2018.

[9] Q. Shi, L. Chang, C. Wang, H. Luo, Q. Huang, and T. Fukuda, "Design and implementation of an omnidirectional vision system for robot perception," *Mechatronics*, vol. 41, 2017.

[10] T. L. Schwartz and L. Kelly, "Rebecca Coakley Low vision rehabilitation update: new and innovative 2015," *Journal of AAPOS*, vol. 19, no. 4, 2015.

[11] J. Radcliffe, J. Cox, and M. Duke, "Bulanon Machine vision for orchard navigation," *Computers in Industry*, vol. 98, 2018.

[12] S. Shuhan Shen, "Accurate multiple view 3D reconstruction using patch-based stereo for large-scale scenes," *IEEE Transactions on Image Processing*, vol. 22, no. 5, pp. 1901–1914, 2013.

[13] X. Sun, X. Jiang, Y. Fu, C. Han, and M. Wen, "Camshaft surface defect detection system based on machine vision," *Infrared and Laser Engineering*, vol. 42, no. 06, pp. 1647–1653, 2013, Chinese.

[14] W. Xie, F. Wang, and D. Yang, "Research on carrot surface defect detection methods based on machine vision," *IFAC-PapersOnLine*, vol. 52, no. 30, pp. 24–29, 2019.

[15] N. Neogi, D. K. Mohanta, and P. K. Dutta, "Defect detection of steel surfaces with global adaptive percentile thresholding of gradient image," *Journal of The Institution of Engineers (India): Series B*, vol. 98, no. 6, pp. 557–565, 2017.

[16] H. Xu, F. Keru, L. Huang, L. Xiong, and Z. Yang, "Improved Otsu algorithm for rolling contact fatigue defect detection," *Journal of Computer Aided Design and Graphics*, vol. 31, no. 07, pp. 1130–1138, 2019, Chinese.

[17] Y. Qu, J. Huang, and X. Zhang, "Rapid 3D reconstruction for image sequence acquired from UAV camera," *Sensors*, vol. 18, no. 1, pp. 225–244, 2018.

[18] L. G. Roberts, *Machine perception of three dimensional solids*, pp. 71–75, Massachusetts Institute of Technology, Cambridge, MA, USA, 1963, Ph.D thesis.

[19] N. Snavely, S. M. Seitz, and R. Szeliski, "Photo tourism: exploring photo collections in 3D," *ACM Transactions on Graphics*, vol. 25, no. 3, pp. 835–846, 2006.

[20] Y. Furukawa and J. Ponce, "Carved visual hulls for image-based modeling," *International Journal of Computer Vision*, vol. 81, no. 1, pp. 53–67, 2009.

[21] J. Jungong Han, L. Ling Shao, D. Dong Xu, and J. Shotton, "Enhanced computer vision with microsoft kinect sensor: a review," *IEEE Transactions on Cybernetics*, vol. 43, no. 5, pp. 1318–1334, 2013.

[22] P. Ondr´ŭska, P. Kohli, and S. Izadi, "Mobile fusion: real-time volumetric surface reconstruction and dense tracking on mobile phones," *IEEE Transactions on Visualization and Computer Graphics*, vol. 21, no. 11, pp. 1251–1258, 2015.

[23] M. Pauly, M. Gross, and L. P. Kobbelt, "Efficient simplification of point-sampled surfaces," in *Proceedings of the IEEE Visualization*, pp. 163–170, Boston, MA, USA, October 2002.

[24] P. Henry, M. Krainin, E. Herbst, X. Ren, and D. Fox, "RGB-D mapping: using Kinect-style depth cameras for dense 3D modeling of indoor environments," *The International Journal of Robotics Research*, vol. 31, no. 5, pp. 647–663, 2012.

[25] X. I. Wen-Fei, Y. M. Fang, L. Shuai, and L. Jian, "A new research on data compression and simplify technology based on laser scanning point cloud," *Engineering of Surveying & Mapping*, vol. 21, no. 4, pp. 38–40, 2012.

[26] F. Villa, F. Severini, F. Madonini, and F. Zappa, "SPADs and SiPMs arrays for long-range high-speed light detection and ranging (LiDAR)," *Sensors*, vol. 21, no. 11, p. 3839, 2021.

[27] S. Nashat, A. Abdullah, and M. Z. Abdullah, "Unimodal thresholding for laplacian-based canny-deriche filter," *Pattern Recognition Letters*, vol. 33, no. 10, pp. 1269–1286, 2012.

[28] H. Balta, J. Velagic, W. Bosschaerts, G. De Cubber, and B. Siciliano, "Fast statistical outlier removal based method for large 3D point clouds of outdoor environments," *IFAC-PapersOnLine*, vol. 51, no. 22, pp. 348–353, 2018.

[29] W. Lorenson and H. Cline, "Marching cubes:A high resolution 3D surface construction algorithm," *Computer Graphics*, vol. 21, no. 4, pp. 163–169, 1987.

[30] F. Wu, J. Li, H. Yang et al., "Research of pavement topography based on NURBS reconstruction for 3D structured light," *Optik*, vol. 194, 2019.

[31] Y. Quinsat and C. Lartigue, "Filling holes in digitized point cloud using a morphing-based approach to preserve volume characteristics," *International Journal of Advanced Manufacturing Technology*, vol. 81, no. 1-4, pp. 411–421, 2015.

[32] H. Meng, C. Wang, and Y. Zhang, "A novel hole filling method based on the hybrid PSO-BP algorithm," *International Journal of Computer Applications*, vol. 156, no. 2, pp. 45–50, 2016.

[33] E. Marchandise, C. Piret, and J.-F. Remacle, "CAD and mesh repair with radial basis functions," *Journal of Computational Physics*, vol. 231, no. 5, pp. 2376–2387, 2012.

Hindawi
International Journal of Optics
Volume 2021, Article ID 7711028, 14 pages
https://doi.org/10.1155/2021/7711028

Review Article

Applications of X-Ray Holography

Bingjun Shi, Yuan Fu, and Yan Yang

College of Mechanical Engineering, Chongqing University of Technology, Chongqing 400054, China

Correspondence should be addressed to Yan Yang; yangyan@cqut.edu.cn

Received 23 October 2021; Revised 9 December 2021; Accepted 22 December 2021; Published 31 December 2021

Academic Editor: Xiaowei Li

X-ray holography is widely used in material, biology, and industry fields due to its potential to measure the microstructure and dynamic change of objects. In this review, the principle of X-ray holography and the development of this technology in different application fields are systematically summarized and discussed. Through analyzing the advancement of X-ray sources and recording medium, the research and development direction of X-ray holography are prospected and the overview on current strategies of novel X-ray holography is presented. It is proved that X-ray holography, as a powerful nondestructive measurement method, can be applied to a wide range of objects.

1. Introduction

In 1948, Gabor [1] formulated the idea of the holographic method, obtaining the first hologram and reconstructed image, for which he won the Nobel Prize in Physics. X-rays were discovered by Roentgen [2, 3] in 1895. Baez [4] combined the idea of holography with X-rays to form a new method. X-ray holography was thereafter paid increasing attention by researchers.

The development of X-ray holography was depended on the highly-bright X-ray sources, the X-ray components, and the recording medium. The idea of holography was first proposed to improve the resolution of the microscope. The first holographic experiment was performed with a visible light source. But at that time, there was no coherent light source to demonstrate all the functions of holography. To find a suitable coherent light source had become the focus of research for many years. Because of the shorter wavelength, X-rays provide a way to achieve higher resolution than visible light. The theoretical foundations of high-resolution X-ray holography were laid by Leith et al. [5–9]. By improving the resolution of the medium and the incident light source [10–15], the researchers succeeded in obtaining X-ray holograms. Especially, Tegze and Faigel [16, 17] analyzed the possibility of atomic resolution in X-ray holography and got holograms with atomic resolution, which brought X-ray holography into a new stage of development. With the improvement of coherent X-ray sources (third-generation synchrotron radiation sources, free electron lasers, and laboratory sources) [18–26] and detector [27–29], studies have shown that the spatial resolution can be greatly improved. To solve imaging artifacts translated by high spatial frequencies, Geilhufe et al. [30] introduced three approaches. They proved that image detail smaller than the source size of the reference beam could be restored to the diffraction limit of the hologram. With the development of these technologies, the resolution of X-ray imaging has reached a higher level.

With the characteristics of short wavelength in penetrating power and high energy, X-rays are combined with holography. As a method of direct three-dimensional imaging, X-ray holography has a great deal of advantages in studying the crystal structure of objects. X-ray holography does not only have the function of optical holography but also some special properties, which makes it advantageous in the three-dimensional imaging and dynamic observation of the internal microstructure of the objects. It can be used to obtain three-dimensional images with atomic resolution, which is widely used in the research on crystals, crystal films, impurities, and lattice distortions [31]. X-rays in the 'water window' have a contrastingly enhancing mechanism for biological samples. The combined application of holography

and X-rays can be used to measure the three-dimensional structure of the biological molecule, the captured images of live cells, and the processing of chemical reactions [32, 33]. Some special functional materials, e.g., nanomaterial and ferroelectric material, are widely used in the production process of significant components. Although it has been a long time since the discovery of these materials, the understanding of their detailed structure and microscopic origin is still unclear. The microstructure of the film's epitaxial growth and the electrode affects the performance of the material and, ultimately, the performance of the components. X-ray holography provides a powerful tool for these studies. This paper will (1) review works of literature that address the applications of X-ray holography in various fields, (2) describe the advantages of X-ray holography, and (3) discuss the prospect of technological development and application.

2. Applications

2.1. Material Field. Material Science is the research, development, production, and application of metallic materials, inorganic nonmetal materials, polymer materials, and composites. At the atomic level, the structure and composition of elements, the spatial sequence of atoms or molecules, and the atomic motion pattern are studied in order to correctly understand and apply materials and develop new materials. Many approaches are used to measure the three-dimensional structure of element atoms and their surroundings in materials. X-ray fluorescence holography (XFH) is one of the approaches [34–37]. The use of short-pulse X-ray sources in combination with high-resolution detectors in X-ray holography can provide clear atomic images. Besides, the deformation of the crystal cannot be directly obtained by the traditional X-ray diffraction (XD) technique, while XFH can be used to solve this problem [31, 38]. Examples of applying X-ray holography in investigations of crystalline structures are discussed in the following section.

Atoms in crystals' internal structure are regularly arranged in three-dimensional space. In fact, many materials are made of a mixture of two or more elements, which affect the internal structure of the crystalic elements making the sample become 'imperfect'. The first implementation of direct XFH measured strontium fluorescence (Figure 1) from a strontium titanate single crystal [17]. In addition, to measure the structure of the elementary atoms in the crystal, XFH is also used to measure the structure around the atoms in the material, which is confirmed by the research of Tegze et al. [39], who pointed out that X-ray holography could measure the three-dimensional image of the local environment of selected atoms with atomic resolution and distinguish atoms in different magnetic states. In 2006, Hosokawa et al. [40] obtained a three-dimensional atomic image around Ge atoms in the $Ge_2Sb_2Te_5$ film with XFH. The analysis of the image showed that the $Ge_2Sb_2Te_5$ single crystal film had no hexagonal point symmetry around Ge atoms (Figure 2). In 2009, Happo et al. [41] obtained a three-dimensional atomic image around Mn atoms in a $Cd_{0.6}Mn_{0.4}Te$ single crystal of dilute magnetic semiconductor with XFH. In the same year, Hosokawa et al. [42] measured the three-dimensional image around the Zn atom in the $Zn_{0.4}Mn_{0.6}Te$ crystal with XFH. In 2011, Hosokawa et al. [43] used XFH to observe the three-dimensional image of In atoms, Tl atoms in the single-crystal $TlInSe_2$ thermoelectric material at room temperature. In 2018, Nishioka et al. [44] used XFH to measure the three-dimensional local structure of atoms in the local plane around Zn in $Mg_{75}Zn_{10}Y_{15}$ alloy. In 2017, Stellhorn et al. [45] used XFH to measure the three-dimensional structure around the Fe and Ni atoms in $Fe_{65}Ni_{35}$ Invar alloy. In 2019, Kimura et al. [46] used XFH to measure the three-dimensional structure around the Fe atoms in $Pb(Fe_{1/2}Nb_{1/2})O_3$(PFN) multiferroic material at different temperatures to study the relationship between atomic images and temperature. In 2020, Ang et al. [47] measured the original and irradiated κ-(BEDT-TTF)$_2$Cu[N(CN)$_2$]Br crystals with XFH. The measurement results are used to study the effect of radiation on the local structure around Cu in the anion layer. The above experiments have proved the successful application of X-ray holography in three-dimensional imaging of atomic structures. Earlier, it was used to study the microstructure and composition of materials. In recent years, it is mainly used to study the change in materials' internal structure under different conditions, which can better evaluate the performance of materials.

Material preparation technology and conditions or special application requirements make crystals contain impurities, and the atomic structure around the impurities will change, resulting in local lattice distortion. XFH can achieve high-resolution imaging of the three-dimensional distribution of atomic structures, and it is very sensitive to the positional fluctuations of atoms from the ideal position. It can also obtain information about local lattice distortion in the process of generating three-dimensional atomic images. Therefore, XFH is very suitable for the analysis of the atomic structure around the impure atoms in the crystal. The research of Hayashi et al. [48] also proved this, for he pointed out that XFH can be used to observe three-dimensional atomic images around specific elements within a radius of nm order and described the local lattice distortions around specific elements. In 2006, Kopecký et al. [49] used X-ray diffuse scattering holography to determine the position of Mn atoms in GaMnAs doped with Mn and obtained new information about the local atomic structure (Figure 3). In 2011, Hayashi et al. [50] used XFH to measure the hologram of $ZnSnAs_2$: Mn thin film and observed the local structure around Mn. In 2018, Kimura et al. [51] used XFH to obtain the in-plane atomic image near In on an In-doped Bi_2Se_3 topological insulator. He found the local lattice distortion and discussed the reason. The measurement results obtained by combining XFH with other experiments or algorithms sometimes are better than using XFH only. In 2017, Hosokawa et al. [52] pointed out the impurity sites of Mn atoms, the distance between Mn-Te atoms, the local lattice distortion and the positional fluctuations around Mn atoms that can only be measured with a combination of the XFH and X-ray absorption fine-structure (XAFS) measurements

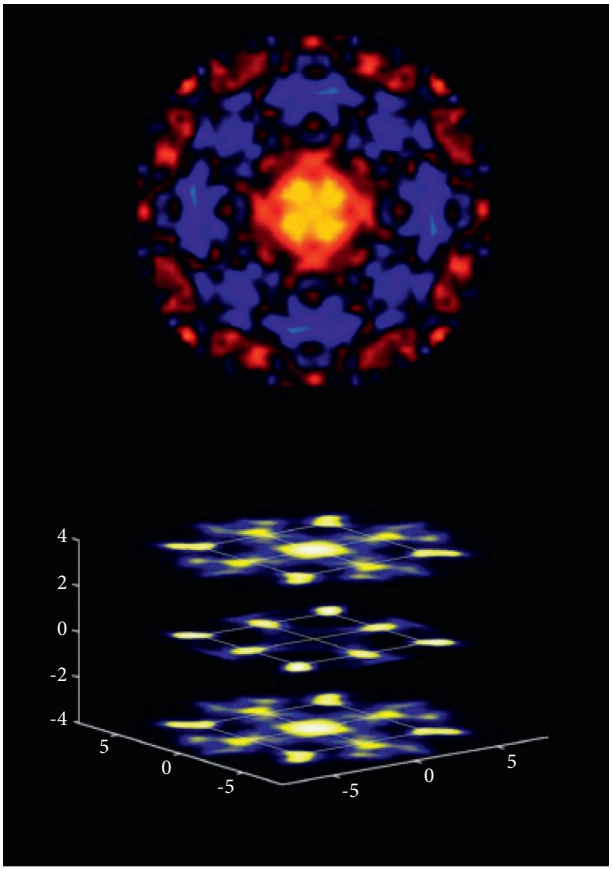

Figure 1: Three-dimensional holographic image of $SrTiO_3$, showing only the Sr atoms [17].

on a single crystal of a $Bi_2Te_3Mn_{0.1}$ topological insulator. In 2020, Stellhorn et al. [53] used XFH with a sparse modeling algorithm to analyze the local structure around the doped atoms in Nd : LaF_3 single-crystal scintillator. He determined that the atoms in the crystal were replaced by impurities and caused very small lattice distortions.

Although XFH has great advantages in measuring the internal structure of materials, it still has shortcomings, and that is why Multi-energy X-ray holography (MEXH) (Figure 4) is used as a new approach to holography. In 1995, Gog et al. [55] used MEXH to image the local atomic environment of Fe atoms in a hematite crystal, which showed that image aberrations caused by single energy were effectively suppressed. Gog et al. [56] pointed out that the accuracy of using MEXH to determine the position of atoms and the degree of the suppression of repetitive image twinnings will be affected by the total amount of imaging under single energy measured within the valid time, the integration and processing approaches in different energy measurements. In 1998, Novikov et al. [54] used multiple energy recording X-ray holograms to image three-dimensional images of Cu_2O crystal structure for the first time and clearly displayed the first Cu–Cu coordination shells. In 2000, Adams et al. [57] used MEXH to image a reciprocal holographic experiment on Cu_3Au single crystal and obtained a three-dimensional image of the Cu_3Au atomic structure. The reconstruction of the measured hologram showed the

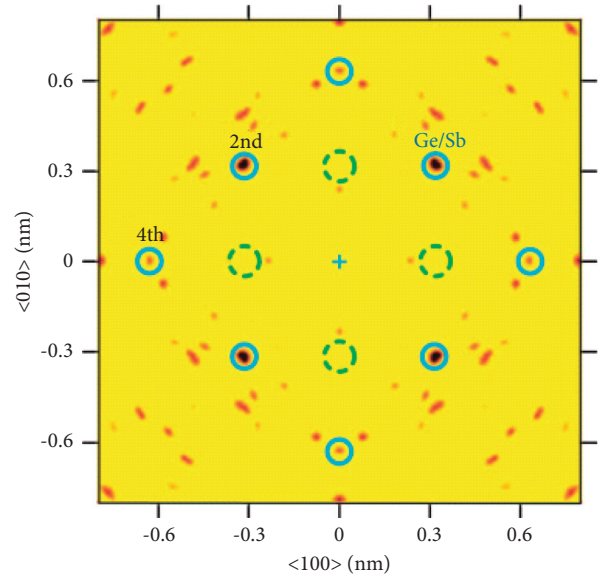

Figure 2: (Color) Atomic images around the central Ge atom [40].

positions of the nearest and the nearest neighbors of Cu atoms, which are identical to the actual ones. In 2001, Hayashi et al. [58] used MEXH to image the local atomic environment of Zn atoms doped in GaAs crystal. Studies have shown that MEXH can be successfully used in the measurement of atomic structure, the surrounding structure of crystals, and the atomic structure of impurities in crystals. Besides, multiple scattering [59] and accidental image cancellations [60] can be suppressed effectively by MEXH, which has an advantage in the improvement of image quality.

The extremely strong and ultrafast X-ray pulses from free-electron lasers make it possible to study the fundamental aspects of complex transient phenomena in materials. In 2007, based on femtosecond time-delay X-ray holography, Chapman et al. [61] monitored the dynamics of the polystyrene sphere and observed the explosion after the initial pulse. They pointed out that the three-dimensional dynamics of materials can be studied on the timescale of atomic motion (Figure 5) with the help of ultrafast X-ray sources. In 2012, Wang et al. [62] used resonant X-ray holography to perform femtosecond single-shot imaging of nanoscale ferromagnetic spin sequences and proved the feasibility of highly efficient single-shot imaging of spin-resolved electronic structures. In 2021, Keskinbora et al. [63] pointed out that the single reconstruction capability of Structured Illumination X-ray Holography (StIXH) is expected to be used in measuring the unreproducible dynamics in ultrahigh time resolution with highly repeating rate X-ray source. The scope of microscopic research can be extended to more samples, such as biological cells or electromagnetic devices.

It is worth mentioning that Complex X-ray Holography (CXH) [64] was proposed to record the phase of scattered X-rays when using resonant X-ray scattering. In 2004, Takahashi et al. [65] succeeded in using the CXH to reconstruct the isolated As atomic images in GaAs crystal. The

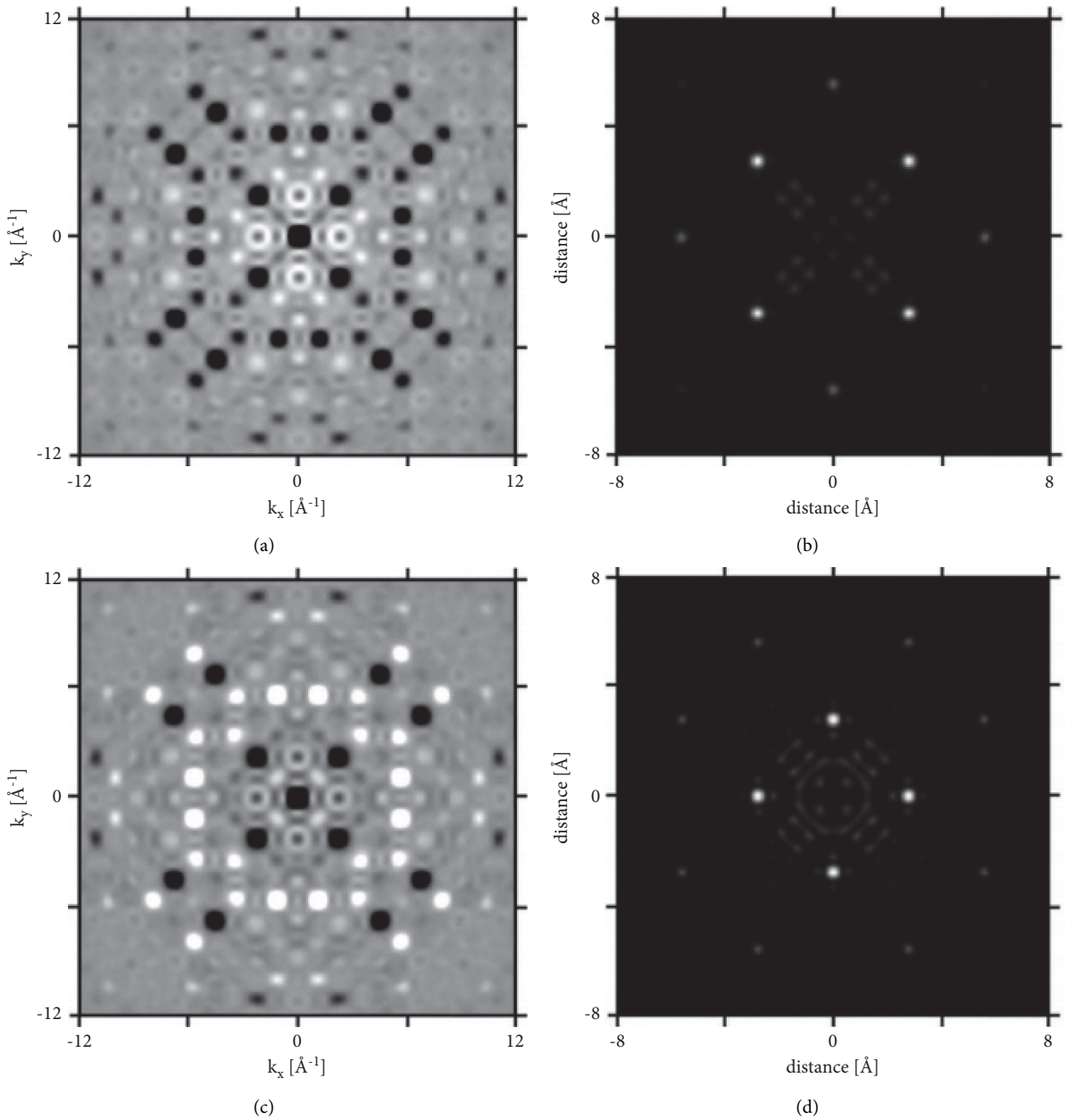

Figure 3: Simulated holograms of clusters of atoms corresponding to the volume of eight unit cells of single-crystal GaAs doped by Mn in (a) substitutional and (c) interstitial positions. (b, d) Real-space images of planes parallel to the (001) crystallographic plane containing reference Mn atoms reconstructed from holograms (a) and (c), respectively [49].

results indicated that the accuracy of the reproduced images can be improved with the CXH. Obviously, its application in measuring material structure is not as wide as that of XFH.

It is shown that X-ray holography is successfully applied in the three-dimensional measurement of atomic structure and the structure around atoms with a high resolution. In particular, XFH has shown significant advantages in three-dimensional imaging and has been widely used. The most applied cases of XFH are to measure changes in the local atomic structure caused by impurities in different materials, including single crystal, amorphous phase change dielectric film, ferromagnetic semiconductor film, and dilute magnetic semiconductor single crystal, thermoelectric material, multiferroic material, topological insulator, etc. MEXH can simultaneously record a variety of different energy and summarize the data of several incident energies, which can thereby effectively suppress the aberration of the holographic image, the twin images, interobject multiple scattering, self-interference and to improve the quality of reconstructed images. XFH can measure crystal deformation, which cannot be done by traditional XD technology. The advantage in measuring the lattice distortion of atoms and impurity atoms in the crystal lattice, observing the degree of distortion, and analyzing the causes of the distortion is conducive to a better understanding of the properties of materials. With the development of a new

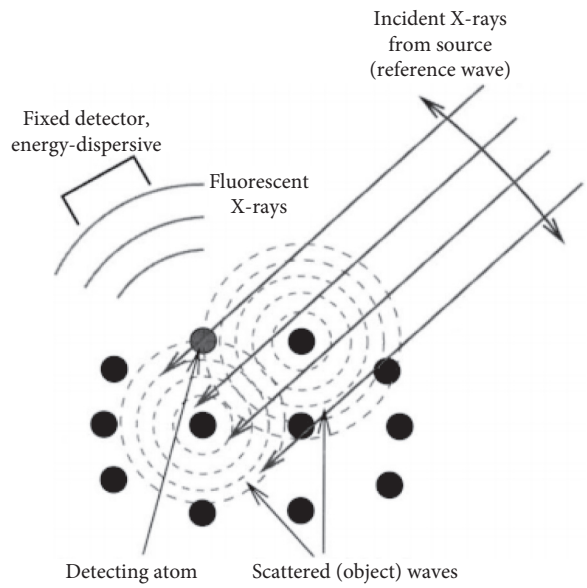

Figure 4: Formation of holograms in MEXH approaches [54].

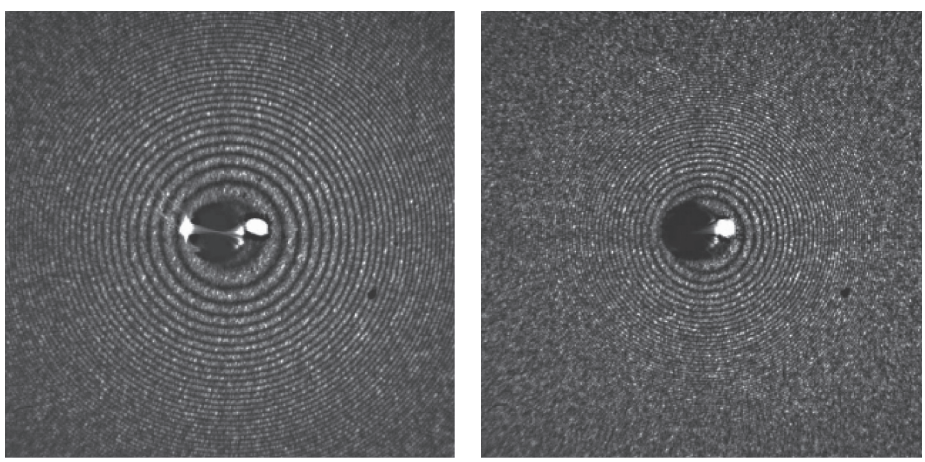

(a) (b)

Figure 5: Time-delay X-ray holograms of 140 nm-diameter polystyrene spheres. The time delays were 348 ± 1 fs (a) and 733 ± 2 fs (b). The pulses were 32 nm wavelength and 25 fs duration with intensities $(0.5 \pm 0.2) \times 10^{14}$ W cm^{-2}. The intensities of the holograms are shown on a linear greyscale, to a half-width of 4.5 μm^{-1}. Deriving the time delays and the change in the optical path through the exploding particles from the fringe pattern, we have found that the particle sizes are determined from the envelope of the intensity [61].

generation of highly coherent X-ray sources, the X-ray holography that uses the generation of synchrotron radiation sources or free-electron X-ray lasers is used to obtain the nanoresolution imaging on the timescale of atomic motions. The development of X-ray holography is closely related to the development of X-ray sources and detectors. It is believed that with the development of science and technology, X-ray holography will see greater improvements in imaging quality, measurement time, and application range.

2.2. Biological Field. Biological imaging is one way to obtain microstructure images of biological cells and tissues and further to understand various physiological processes of biological cells through image analysis. In 1980, Kirz and Sayre [66] proposed the use of X-ray microscopy to achieve three-dimensional images of microscopic organisms. In 1987, Howells et al. [67] used X-ray technology to measure pancreatic zymogen granules. Limited by the poor coherence of the X-ray source and the low resolution of the detector, the resolution obtained in the experiment has not exceeded the resolution of the optical microscope.

With the development of modern biology and genetics, determining the structural information of the measured objects is becoming the key to solving the problem. There is an urgent need for tools to study the structure and function of biological macromolecules. The advantages of X-ray holography in life-science research are as follows: (1) high

resolution, (2) direct measurement and processing on live samples with its ability to distinguish atoms, (3) dynamic observation of the processing. Biological cells can be analyzed by X-rays with the latest development in X-ray focusing, diffraction data analysis, and coherent imaging reconstruction algorithms [68]. The development of new technology makes it possible to study biological cells in different preparation states (freeze-drying, low-temperature vitrification, chemical fixation, and living cells).

Ultrafast X-ray imaging can achieve high-resolution images, which traditional imaging techniques cannot obtain when measuring living samples [69]. In 1991, Nugent et al. [70] pointed out that coherent soft X-ray holography is a technology that can achieve high-resolution imaging. Because the technology and components required for the experiments had not been developed to an advanced enough state, the advantages of coherent soft X-ray holography were not displayed at that time. Based on the need to produce three-dimensional images of comparably bigger life-science samples with a resolution of about 10 nm, Howells et al. [71] proposed a new form of Fourier-transform X-ray holography, which has higher resolution and can determine the phase and amplitude of the diffracted wave field. In 2000, Murray et al. [72] used X-ray holography to reconstruct the crystal structure of the enzyme-product complex of the hammerhead ribozyme and observed the interaction between residues and functional groups. In 2011, Gorniak et al. [33] demonstrated the first digital X-ray hologram of a biological sample recorded in the water window (Figure 6), which greatly promoted the development of imaging hydrated biological material with photons. In 2016, Tomita et al. [73] observed X-ray fluorescence holograms from protein crystals for the first time with minimal radiation damage and started a promising approach for investigating the metal active-sites in biomacromolecules. In the same year, Nicolas et al. [74] used a combination of scanning small-angle X-ray Scattering (SAXS) and full-field holography to test actomyosin in freeze-dried neonatal rat cardiomyocytes. It is shown that X-ray holography is ideal in completing missing scattered data at low momentum transfer by the structure factor, extending the covering range of spatial frequencies by two orders of magnitude. In 2017, Tomita et al. [75] used XFH to measure hemoglobin (Hb) and obtained the atomic image of the hemoglobin environment in a single subunit of Hb. Tomography is a well-established X-ray technique for imaging a medical object in three dimensions by generating images of certain layers [76]. In 2020, Kuan et al. [77] used X-ray holographic nanotomography (XNH) to reconstruct the main dendrites and axon branches of neurons of *Drosophila melanogaster* and mice with a resolution of sub-100 nm.

It is shown that X-ray holography has been successfully applied in the imaging of biomolecular structures and achieved high-resolution images of the crystal structure of samples, e.g., enzyme-product complexes, protein crystals, hemoglobin, hydrated biological samples, and nerve tissue. The correct understanding of biological structure is conducive to understanding its change process, being helpful to further understand its impact on the realization of specific functions. The nervous system is mainly composed of nerve tissues, which can regulate and control the physiological activities of the human body. The reconstruction of the main part of neurons is beneficial to the research of neural circuits.

X-ray holography can not only be used in the measurement of biological cells but also in the inspection and treatment of diseases. The disadvantage of cancer radiotherapy is that the normal tissues adjacent to the tumor cells will be affected during the treatment. In 1999, Madjidi-Zolbin and Jafari [78] pointed out that X-ray holography can accurately focus radiation on tumor cells (Figure 7) and reduce the damage to the healthy tissues surrounding the tumor cells during treatments. In 2008, Nesterets et al. [79] used X-ray phase-contrast in-line holography with ultrafast laser-based X-ray source to study the distribution of proliferating cell density with stationary cell cores and shells. The contrasting reconstructed images by phase was enhanced. The result proved the feasibility of this approach for microimaging of small soft tissue avascular tumors. In 2020, Dahlin et al. [80] used X-ray phase-contrast holographic nanotomography to perform three-dimensional scanning of neural tissues on the subcellular scale and achieved high-resolution neural three-dimensional imaging. The understanding of peripheral nerve structure helps to explain the pathology of neuropathy and to analyze the cause of illness. At the same time, the success of the experiment proved the effectiveness of this approach in peripheral nerve biopsies. In 2020, Samber et al. [81] used synchrotron radiation-based nanoscale X-ray fluorescence and X-ray online holography to study the distribution of nanoscale iron in a single fibroblast from Friedreich's ataxia (FRDA) patients. In this research, various micrometre-sized iron-rich organelles were revealed for the first time, which provided an innovative way to understand FRDA.

Besides, XFH can be used to study the local atomic structure of inorganic crystals and soft material samples, thus providing atomic resolution structural information and distinguishing experiments of different valence states of the same element in the sample [82]. Tegze et al. [83] pointed out that X-ray holography may be able to measure single molecules and viruses, and this will require ultrafast X-ray sources.

Studies have proved that X-ray holography has successfully achieved the three-dimensional measurement of biological microstructures with high resolution. In addition to the need to improve the resolution of images, the development of biological imaging technology also needs to enhance the real-time and continuous research of imaging. The goal of imaging is fully revealing the biological function by achieving continuous tracking of a single biologically functional molecule and recording its physiological process in detail. An important prerequisite for X-ray holography to be widely used in disease diagnosis is noninvasive. It can accurately focus on the lesion to achieve fixed-point detection and treatment, reducing damage to other parts. The application of bioimaging technology in clinical medical diagnosis has been paid more and more attention. In the past few decades, in macromolecular crystallography, the overall damage caused by X-ray irradiation has always been a

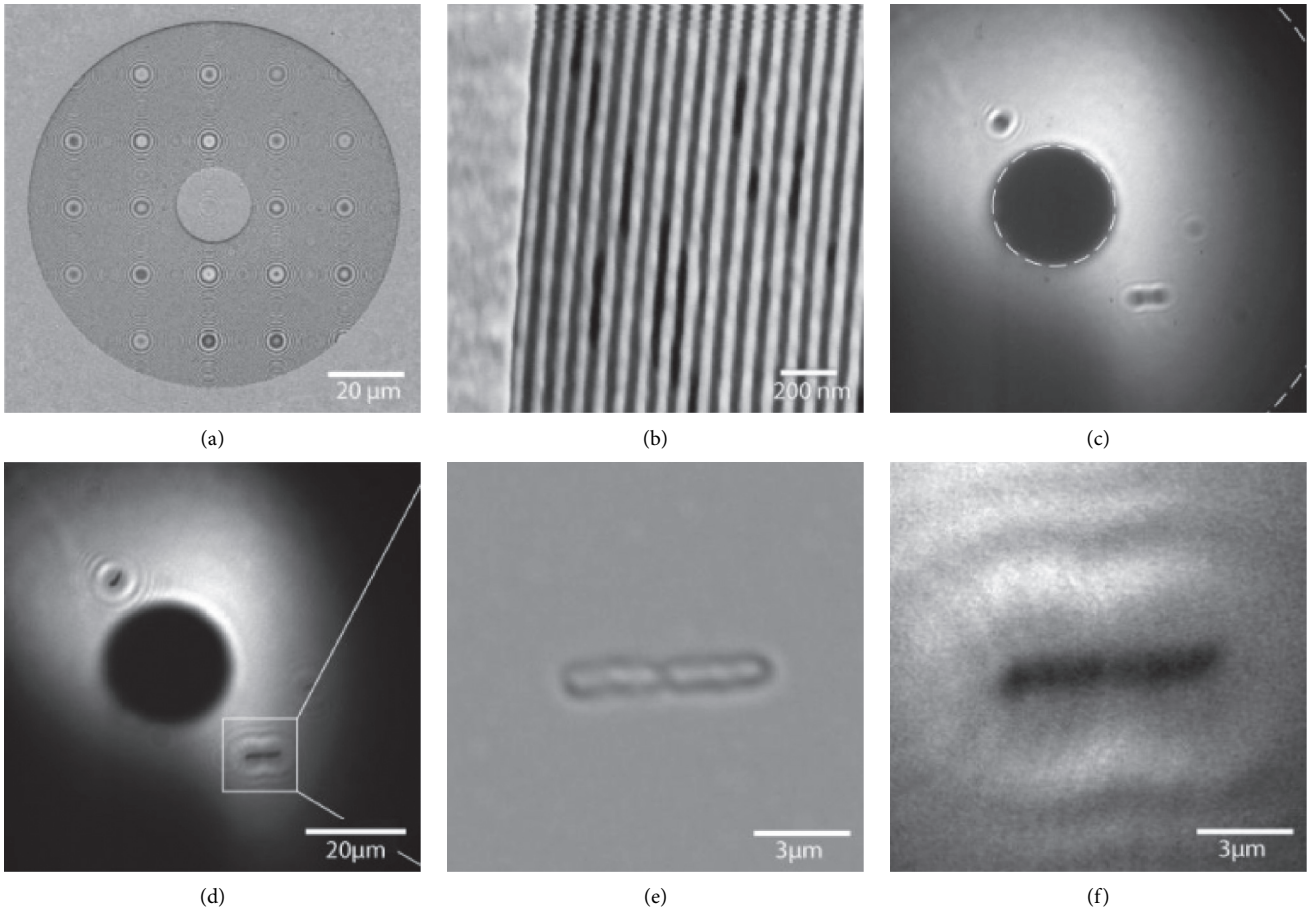

Figure 6: Imaging the marine bacteria *Cobetia marina* in the water window at $\lambda_3 = 2.68$ nm using digital in-line holography. (a) SEM image of the used zone plate with a clearly visible central beam stop. (b) Close-up of the zone plate's outermost zones. (c) X-ray hologram with *Cobetia marina* in the lower right corner. (d) Reconstruction of hologram (c). (e) Sample *Cobetia marina* under an optical microscope in bright field illumination (100x, NA = 0.9). (f) Magnified ROI of the reconstructed image as indicated by the rectangle in (d) [33].

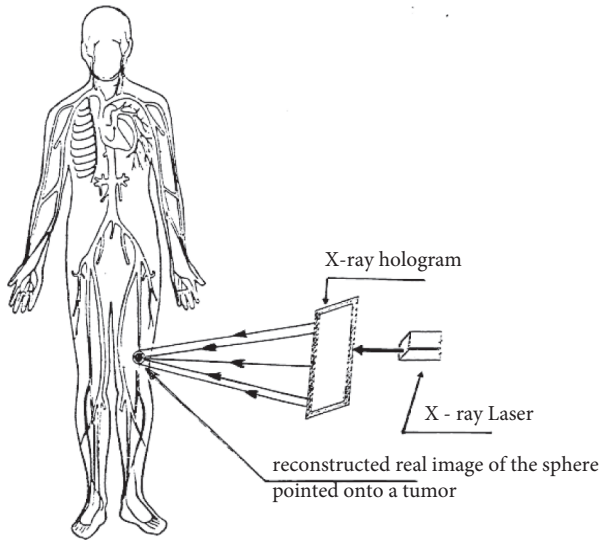

Figure 7: A schematic illustration of cancer treatment by X-ray holography [78].

problem faced by scholars, but the best solution currently proposed is cryogenic cooling. The highly coherent light source enables X-ray holography to achieve dynamic measurement in the femtosecond range. With the improvement of new technologies and approaches, the measurement time can be shortened and it is practical to complete the measurement before the sample becomes invalid. The new generation of free electron laser type X-ray source combined holography may be able to measure the three-dimensional structure of single molecules, viruses, and other tiny systems that cannot be crystallized, which will greatly promote the development of this process.

2.3. Industrial Field. With the rapid development of industry, the miniaturization, integration, and intelligence of components have made functional materials with special properties widely used, which demands higher requirements for material performance.

The research on nanomaterials is indispensable with special physical properties, chemical properties, and application value. The experiments show the successful measurement of nanostructured materials, which can help to understand the type, quantity, and internal structure of substances and to obtain products with special functional requirements. One of the significant applications of X-ray holography is to measure nanostructures. There are several ways that can be used to measure tiny structures with high resolution, e.g., high-brightness synchrotron radiation accelerator, optimized testing technology, and improved experimental equipment combined with X-ray holography. In 2005, Hellwig et al. [84] used soft X-ray spectroscopy holography to measure the magnetic nanostructures, whose reconstructed image had a spatial resolution below 50 nm. In 2007, Scherz et al. [85] demonstrated phase imaging of magnetic nanostructures by resonant soft X-ray holography. It is shown that the use of quantitative and spectral phase approaches allows high-contrast imaging of nanoscale electronic and magnetic levels while increasing the depth of detection and reducing the radiation dose by an order of magnitude. In 2009, Streit-Nierobisch et al. [86] proposed that resonant soft X-ray holography could be used to measure the magnetic domain structure of different Co/Pt multilayer films (Figure 8). By studying focused ion beam (FIB)-induced anisotropic modulation and vertical domain structure in nanostructure samples, the size and configuration of domains can be controlled by adjusting the amount of ionic agent applied in a single point. In 2010, Chamard et al. [87] demonstrated the three-dimensional imaging of SiGe nanocrystal with Bragg Fourier transform holography and obtained the shape, the internal views of the density, and displacement field. The simplicity and stable inversion have opened up a new way of in-situ study of the inhomogeneous strain field in the nanocrystal. In 2011, Kim et al. [88] obtained the reconstructed image of nanomaterials with the resolution of 87 nm with single-shot Fourier-transform X-ray holography and X-ray laser. In 2020, Zhang et al. [89] reconstructed the evolved nanostructures in ultrathin films with X-ray waveguide fluorescence holography. The analysis results showed that the controllable synthesis of nanostructure ultrathin films may become a reality.

It is obvious that researchers have increased their research on nanomaterials and have gradually deepened it in recent years due to the development of a new generation of synchrotron radiation sources and detectors. The approaches of measurement with efficient image processing programs have improved experimental devices and optimized reconstruction algorithm. With other technologies, they have greatly promoted the precise measurement of nanostructures.

Epitaxial growth refers to the growth of a single crystal layer on a single crystal substrate under certain requirements. It has the same crystal orientation as the substrate. Many electronic devices are fabricated with the technology of epitaxial growth on single-crystal substrates. Studies have shown that the local atomic structure of thin film samples can be obtained by XFH. In 2004, Sekioka et al. [90] found that whether the material accepts radiation has a significant difference in the local atomic structure hologram of the $EuBa_2Cu_3O_{7-\sigma}$(EBCO) superconductor films measured by XFH. In 2014, Happo et al. [91] used XFH to observe the local atomic structure around Ge and Mn atoms in $Ge_{0.6}Mn_{0.4}Te$ thin films and found the local lattice distortions around Ge atoms (Figure 9). In 2015, Hayashi et al. [92] used XFH to evaluate the crystal structure of $ZnSnAs_2$ thin films.

The ferroelectric material is a kind of functional material with ferroelectric effects as ferroelectricity and piezoelectricity. It has very significant applications in microelectronics, photovoltaics, and sensors to make ferroelectric memories, pyroelectric infrared detectors, spatial light modulators, optical waveguides, and so on. Scott [93] researched ferroelectric materials and found that their applications are still in the development stage. Hayashi et al. [94] used XFH to analyze the local structure around Ti in the ferroelectric material $Pb(Zr_{0.7}Ti_{0.3})O_3$ crystal (Figure 10). Essential for the design of new and improved ferroelectric materials, the result can be used to understand the local structure of lead zirconate titanate (PZT) and reveal the microscopic origin of high dielectric and piezoelectric response.

The demand and requirements for energy to be green and sustainable are becoming a trend, in which lithium batteries have become a mainstream energy source. Widely used as a high-efficient and environmentally friendly high-temperature fuel cell, the performance of battery electrodes is affected by their microstructure and electrochemical performance. X-ray nanoholography can also be used to study the microstructure of the electrode of solid oxide fuel cells. Based on the requirements of brightness and hard X-ray, this technology is nondestructive. To obtain three-dimensional images requires the use of a third-generation synchrotron. Villanova et al. [95] performed quantitative phase-contrast X-ray nanoholographic imaging on a large number of solid oxide fuel cells (SOFC) anodes composed of Ni/YSZ cermet. Then Grindler et al. [96–99] studied the microstructure of electrodes based on different objectives. For comparison between different electrodes and electrode

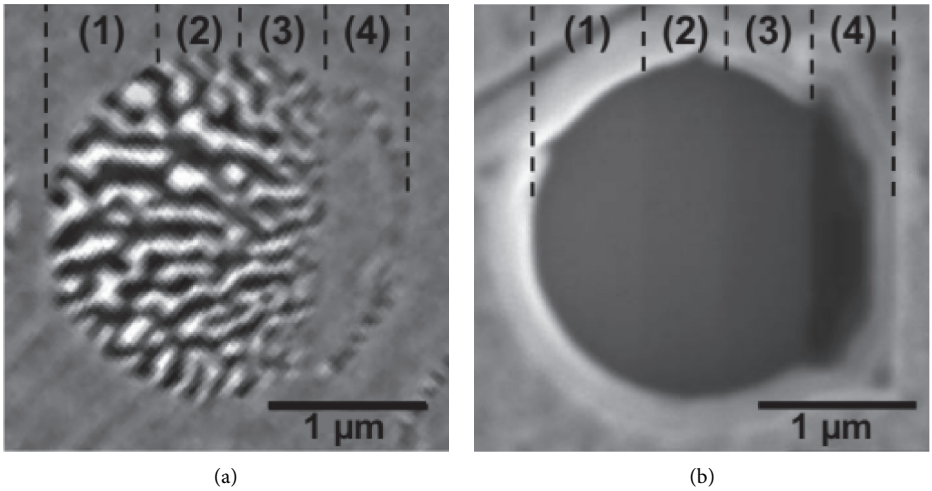

Figure 8: (a) Domain image of a Co/Pt sample structured with stripes of increasing ion dose, labeled (1–4), at remanence. (b) SEM image of the sample [86].

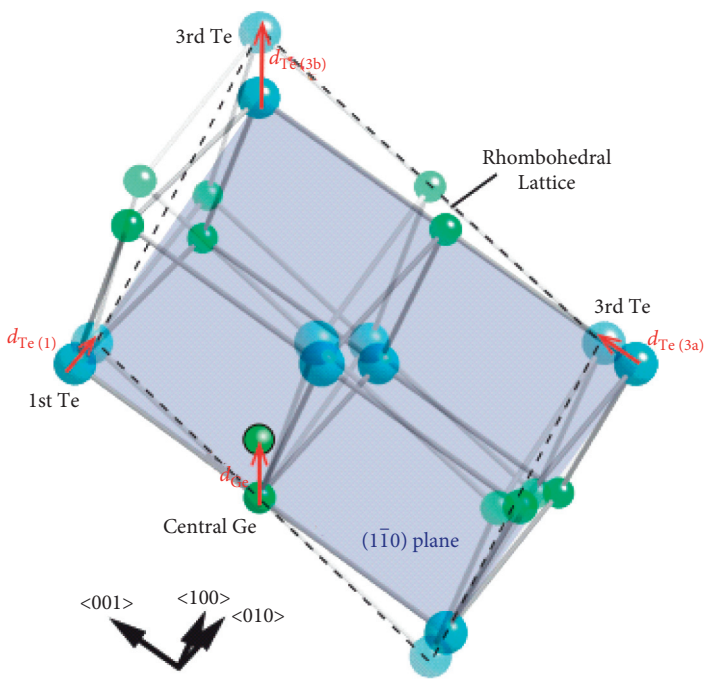

Figure 9: (Color) Distortion model around the central Ge atom in $Ge_{0.6}Mn_{0.4}Te$. For clarity, the distortions in the illustration are much larger than the real ones (the distortion of the lattice angle is about 5 times as large as the true value) [91].

optimization, Nguyen et al. [100] used quantitative phase-contrast X-ray nanoholography to analyze the microstructure of $LiNi_{0.5}Mn_{0.3}Co_{0.2}O_2$ high-energy density electrodes and quantified them.

Recently, a new application of X-ray holography has been discovered. Turnbull et al. [101] researched nanoscopic lamellae of centrosymmetric ferromagnetic alloy and showed tilted holographic images at 30° incidence. They have proved the successful application of X-ray holography in identifying the topology of localized structures in nanoscale magnetism. Blukis et al. [102] used XFH to image the magnetic structure of the Tazewell IIICD meteorite cloud area with a spatial resolution of 40 nm. This is the first case of applying XFH to measure the magnetization of a single magnetic particle. Its response to a magnetic field can directly measure its magnetic stability and the strength of particle interaction. It provides a new approach for studying the magnetic field of the early Solar System and further for studying the formation of the Solar System and the process of early planetary evolution.

In this section, X-ray holography is mainly reviewed for three-dimensional imaging of nanomaterials, thin film crystals, ferroelectric materials, and electrode structures. Fundamentally, these research objects are on functional

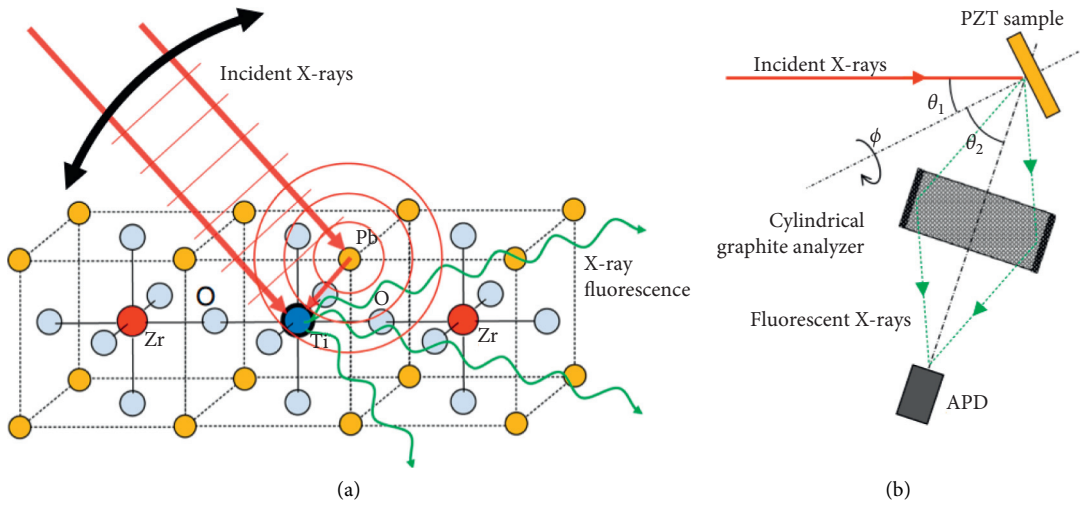

Figure 10: Principle and experimental setup of XFH. (a) Principle of inverse XFH. In this study, Ti in PZT was the target element. (b) Experimental setup for inverse XFH [94].

materials with special purposes but are different from general materials. X-ray holography can realize the measurement of the three-dimensional atomic structure of nanostructured materials, which is the basis for understanding nanomaterials. In reality, most nanomaterials are manufactured artificially with the premise of understanding. The epitaxial growth technology improves the flexibility of device design and the performance of the device. X-ray holography successfully realized the three-dimensional imaging of the extrinsic long film structure. Through the measurement of structural changes among different elements, the influence of change in external conditions on the internal element structure can be obtained. This is helpful for the study of the working process of that material. As a special functional material, ferroelectric materials have significant applications in many aspects. The three-dimensional imaging of the internal microstructure of ferroelectric materials is mainly used to study the composition and structure of materials, which helps to understand the microscopic origin of special properties and make better use of ferroelectric materials. The measurement of the microstructure of the electrode helps to study the influence of the internal substance of the electrode, its shape on the performance of the electrode, and the optimization of the electrode. Through the measurement of structural changes, the influence of changes in external conditions on the internal element structure of the material and among different elements can be obtained, which are helpful for the study of the working process of the material. Research on materials is the key to the progress and development of industry.

Through X-ray holography, the understanding of these special materials has been further improved. The rapid development of science and technology puts forward higher requirements for materials. So to discover more properties of materials becomes the focus of the following research. However, research on composite nanomaterials, high-performance ferroelectric materials, low-temperature solid oxide battery materials, and high-performance epitaxial growth technology are still in their infancy. With the improvement of technology, X-ray holography, we believe, will become an important tool for more in-depth material research.

3. Conclusions

As a mature approach of three-dimensional imaging, X-ray holography has many advantages and a wide range of applications in material science, biomedical science, and industry, which attracts many researchers to invest increasing energy in the study and its development. The research and applications of X-ray holography have been more than a century. They have drawn extensive attention from scholars from the beginning. As an important tool, X-ray holography has shown many strong advantages, such as high spatial resolution, short measurement time, and more advanced image reconstruction approaches. It is not difficult to find that the application range and measurement results of X-ray holography are related to the improvement of test equipment and technological progress. These technologies include many aspects. The first of them is the X-ray source. The development of synchrotron radiation accelerators and free electron lasers can provide brighter and better coherent light sources, which can excite shorter pulses to achieve femtosecond imaging. In this case, the holographic images like 'continuous' to achieve dynamic measurement of the microstructure. The second is the improvement of measurement approaches. The higher measurement requirements have led to the emergence of many measurement approaches, including improvements of the existing approach and the combination with traditional approaches. The third is the upgrade of the image reconstruction algorithm. The second step of holography is an image reconstruction based on the principle of diffraction, providing the phase information of the image. Combined with more optimized algorithms, high-resolution images and more information can be obtained.

Although X-ray holography is currently in full swing, its technology still faces many challenges. For example, X-ray holography can measure the structure of materials with atomic resolution and also their microstructures on prepared biological samples. But there are great challenges in measuring the microstructure of living cells. As is known to all that X-rays have radiation, which can damage the structure of the tested sample and make the measurement results inaccurate. This is a huge challenge to measure the microstructure of sensitive materials and live biological samples with X-ray holography. Imaging neuron networks provide a basis for understanding the nervous system. Nanoscale X-ray holography based on synchrotron radiation can perform three-dimensional imaging of nerve tissue on a subcellular scale, which is tremendously helpful to understand the pathological mechanism of neurological diseases. The next focus of research will be about how to perform three-dimensional imaging on a smaller scale while obtaining more information. Radiation therapy is a useful means to treat some diseases. X-ray holography can accurately focus the radiation on the diseased part and reduce the damage to other parts. In order to obtain a smaller damage range, an urgent problem to be solved is how to achieve the precise positioning of the target. The development and application of high-performance functional materials are related to the development of the industry. However, the current technical conditions are limiting a comprehensive understanding of the properties of these materials and the mastery of the preparation process. With the advancement of X-ray holography, it is believed that these problems will finally be solved. The key research is on X-ray sources as for the progress and development of X-ray holography. The fourth-generation synchrotron radiation emitter can produce high-brightness, short-pulse X-ray sources. Combined with high-performance detectors and optimized algorithms, it is expected to achieve dynamic and accurate measurements of smaller structures on the femtosecond scale while expanding the range of measurement. In the future, further theoretical and practical research will promote the application of X-ray holography to the three-dimensional measurement of more diverse microstructures.

Conflicts of Interest

The authors declare no conflicts of interest.

Acknowledgments

This work was supported by the National Natural Science Foundation of China (51875068, 52075062) and the National Key Research and Development Program of China (2020YFB2010100).

References

[1] D. Gabor, "A new microscopic principle," *Nature*, vol. 161, no. 4098, pp. 777-778, 1948.

[2] W. K. Röntgen, "A new form of radiation," *Science*, vol. 3, no. 72, pp. 726–729, 1896.

[3] W. C. Röntgen, "On a new kind of rays," *Science*, vol. 3, no. 59, pp. 227–231, 1896.

[4] A. V. Baez, "A study in diffraction microscopy with special reference to X-rays," *Journal of the Optical Society of America*, vol. 42, no. 10, pp. 756–762, 1952.

[5] E. N. Leith, J. Upatnieks, and K. A. Haines, "Microscopy by wavefront reconstruction∗," *Journal of the Optical Society of America*, vol. 55, no. 8, pp. 981–986, 1965.

[6] J. T. Winthrop and C. R. Worthington, "X-ray microscopy by successive fourier transformation," *Physics Letters*, vol. 15, no. 2, pp. 124–126, 1965.

[7] J. T. Winthrop and C. R. Worthington, "X-ray microscopy by successive Fourier transformation II. An optical analogue experiment," *Physics Letters*, vol. 21, no. 4, pp. 413–415, 1966.

[8] G. W. Stroke, D. Brumm, A. Funkhouser, A. Labeyrie, and R. C. Restrick, "On the absence of phase-recording or "twin-image" separation problems in "Gabor" (in-line) holography," *British Journal of Applied Physics*, vol. 17, no. 4, pp. 497–500, 1966.

[9] G. L. Rogers and J. Palmer, "The possibilities of X-ray holographic microscopy*," *Journal of Microscopy*, vol. 89, no. 1, pp. 125–135, 1969.

[10] S. Aoki and S. Kikuta, "X-ray holographic microscopy," *Japanese Journal of Applied Physics*, vol. 13, no. 9, pp. 1385–1392, 1974.

[11] G. C. Bjorklund, S. E. Harris, and J. F. Young, "Vacuum ultraviolet holography," *Applied Physics Letters*, vol. 25, no. 8, pp. 451-452, 1974.

[12] S. Aoki and S. Kikuta, "Soft X-ray interferometry and holography," *American Institute of Physics Conference Proceedings*, vol. 147, no. 1, pp. 49–56, 1986.

[13] J. E. Trebes, S. B. Brown, E. M. Campbell et al., "Demonstration of X-ray holography with an X-ray laser," *Science*, vol. 238, no. 4826, pp. 517–519, 1987.

[14] S. Kikuta, S. Aoki, S. Kosaki, and K. Kohra, "X-ray holography of lensless Fourier-transform type," *Optics Communications*, vol. 5, no. 2, pp. 86–89, 1972.

[15] B. Reuter and H. Mahr, "Experiments with Fourier transform holograms using 4.48 nm X-rays," *Journal of Physics E: Scientific Instruments*, vol. 9, no. 9, pp. 746–751, 1976.

[16] M. Tegze and G. Faigel, "Atomic-resolution X-ray holography," *Europhysics Letters*, vol. 16, no. 1, pp. 41–46, 1991.

[17] M. Tegze and G. Faigel, "X-ray holography with atomic resolution," *Nature*, vol. 380, no. 6569, pp. 49–51, 1996.

[18] A. Rosenhahn, R. Barth, X. Cao, M. Schürmann, M. Grunze, and S. Eisebitt, "Vacuum-ultraviolet Gabor holography with synchrotron radiation," *Ultramicroscopy*, vol. 107, no. 12, pp. 1171–1177, 2007.

[19] K. Giewekemeyer, H. Neubauer, S. Kalbfleisch, S. P. Krüger, and T. Salditt, "Holographic and diffractive x-ray imaging using waveguides as quasi-point sources," *New Journal of Physics*, vol. 12, no. 3, p. 035008, 2010.

[20] K. Hayashi, M. Miyake, T. Tobioka, Y. Awakura, M. Suzuki, and S. Hayakawa, "Development of apparatus for multiple energy X-ray holography at spring-8," *Nuclear Instruments and Methods in Physics Research Section A: Accelerators, Spectrometers, Detectors and Associated Equipment*, vol. 467-468, pp. 1241–1244, 2001.

[21] A. Rosenhahn, F. Staier, T. Nisius et al., "Digital In-line Holography with femtosecond VUV radiation provided by the free-electron laser FLASH," *Optics Express*, vol. 17, no. 10, pp. 8220–8228, 2009.

[22] B. Pfau, C. M. Günther, S. Schaffert et al., "Femtosecond pulse x-ray imaging with a large field of view," *New Journal of Physics*, vol. 12, no. 9, p. 95006, 2010.

[23] A. P. Mancuso, T. Gorniak, F. Staier et al., "Coherent imaging of biological samples with femtosecond pulses at the free-electron laser FLASH," *New Journal of Physics*, vol. 12, no. 3, p. 35003, 2010.

[24] S. Chen, H.-W. Chai, A.-M. He, T. Tschentscher, Y. Cai, and S.-N. Luo, "Resolving dynamic fragmentation of liquids at the nanoscale with ultrafast small-angle X-ray scattering," *Journal of Synchrotron Radiation*, vol. 26, no. 5, pp. 1412–1421, 2019.

[25] F. Bencivenga, R. Mincigrucci, and F. Capotondi, "Nanoscale transient gratings excited and probed by extreme ultraviolet femtosecond pulses," *Science Advances*, vol. 5, no. 7, p. eaaw5805, 2019.

[26] S. Marchesini, S. Boutet, A. E. Sakdinawat et al., "Massively parallel X-ray holography," *Nature Photonics*, vol. 2, no. 9, pp. 560–563, 2008.

[27] P. Lechner, C. Fiorini, and R. Hartmann, "Silicon drift detectors for high count rate X-ray spectroscopy at room temperature," *Nuclear Instruments and Methods in Physics Research Section A: Accelerators, Spectrometers, Detectors and Associated Equipment*, vol. 458, no. 1-2, pp. 281–287, 2001.

[28] P. Lechner, A. Pahlke, and H. Soltau, "Novel high-resolution silicon drift detectors," *X-Ray Spectrometry*, vol. 33, no. 4, pp. 256–261, 2004.

[29] S. Mertens, A. Alborini, K. Altenmüller et al., "A novel detector system for KATRIN to search for keV-scale sterile neutrinos," *Journal of Physics G: Nuclear and Particle Physics*, vol. 46, no. 6, p. 065203, 2019.

[30] J. Geilhufe, B. Pfau, C. M. Günther, M. Schneider, and S. Eisebitt, "Achieving diffraction-limited resolution in soft-X-ray Fourier-transform holography," *Ultramicroscopy*, vol. 214, p. 113005, 2020.

[31] V. V. Lider, "X-ray holography," *Physics-Uspekhi*, vol. 58, no. 4, pp. 365–383, 2015.

[32] J. C. Solem, "Imaging biological specimens with high-intensity soft x rays," *Journal of the Optical Society of America B*, vol. 3, no. 11, pp. 1551–1565, 1986.

[33] T. Gorniak, R. Heine, A. P. Mancuso et al., "X-ray holographic microscopy with zone plates applied to biological samples in the water window using 3rd harmonic radiation from the free-electron laser FLASH," *Optics Express*, vol. 19, no. 12, pp. 11059–11070, 2011.

[34] S. Kaldor, "Use of area array detector for X-ray fluorescence holography allows simultaneous recording of the full hologram without sacrificing angular accuracy," *MRS Bulletin*, vol. 26, no. 6, p. 432, 2001.

[35] S. Marchesini and C. S. Fadley, "X-ray fluorescence holography: going beyond the diffraction limit," *Physical Review B*, vol. 67, no. 2, p. 024115, 2003.

[36] Y. Takahashi, K. Hayashi, and E. Matsubara, "Development and application of laboratory X-ray fluorescence holography equipment," *Powder Diffraction*, vol. 19, no. 1, pp. 77–80, 2004.

[37] K. Hayashi and P. Korecki, "X-ray fluorescence holography: principles, apparatus, and applications," *Journal of the Physical Society of Japan*, vol. 87, no. 6, p. 061003, 2018.

[38] N. Happo, Y. Takehara, M. Fujiwara et al., "Local structure around Mn atoms in IV-VI ferromagnetic semiconductor Ge0.6Mn0.4Te investigated by X-ray fluorescence holography," *Japanese Journal of Applied Physics*, vol. 50, no. 5S2, p. 05FC11, 2011.

[39] M. Tegze, G. Faigel, and G. Bortel, "X-ray holography: atoms in 3D," *Journal of Alloys and Compounds*, vol. 401, no. 1-2, pp. 92–98, 2005.

[40] S. Hosokawa, T. Ozaki, K. Hayashi et al., "Existence of tetrahedral site symmetry about Ge atoms in a single-crystal film of Ge2Sb2Te5 found by x-ray fluorescence holography," *Applied Physics Letters*, vol. 90, no. 13, p. 131913, 2007.

[41] N. Happo, K. Hayashi, and S. Hosokawa, "Atomic image around Mn atoms in diluted magnetic semiconductor Cd0.6Mn0.4Te obtained from X-ray fluorescence holography," *Journal of Crystal Growth*, vol. 311, no. 3, pp. 990–993, 2009.

[42] S. Hosokawa, N. Happo, and K. Hayashi, "Reconciling the Pauling bond length picture and Vegard's law in a mixed crystal: an x-ray fluorescence holographic study," *Physical Review B*, vol. 80, no. 13, p. 134123, 2009.

[43] S. Hosokawa, N. Happo, K. Hayashi et al., "Three-dimensional atomic images of TlInSe2Thermoelectric material obtained by X-ray fluorescence holography," *Japanese Journal of Applied Physics*, vol. 50, no. 5S2, p. 05FC06, 2011.

[44] T. Nishioka, Y. Yamamoto, K. Kimura et al., "In-plane positional correlations among dopants in 10H type long period stacking ordered Mg75Zn10Y15 alloy studied by X-ray fluorescence holography," *Materialia*, vol. 3, pp. 256–259, 2018.

[45] J. R. Stellhorn, Y. Ideguchi, S. Hosokawa et al., "Temperature-dependent local atomic structures in the traditional Fe65Ni35Invar alloy by X-ray fluorescence holography," *Surface and Interface Analysis*, vol. 50, no. 8, pp. 790–794, 2018.

[46] K. Kimura, K. Yokochi, R. Kondo et al., "Local structural analysis of Pb(Fe1/2Nb1/2)O3 multiferroic material using X-ray fluorescence holography," *Japanese Journal of Applied Physics*, vol. 58, no. 10, p. 100601, 2019.

[47] A. K. R. Ang, R. Marumi, A. Sato-Tomita et al., "Elucidation of local structure deformation in κ–(BEDT–TTF)2Cu [N(CN)2]Br by x-ray fluorescence holography," *Physical Review B*, vol. 103, no. 21, p. 214106, 2021.

[48] K. Hayashi, N. Happo, and S. Hosokawa, "Applications of X-ray fluorescence holography to determine local lattice distortions," *Journal of Electron Spectroscopy and Related Phenomena*, vol. 195, pp. 337–346, 2014.

[49] M. Kopecký, J. Kub, and E. Busetto, "Location of Mn sites in ferromagnetic Ga1− xMnxAs studied by means of X-ray diffuse scattering holography," *Journal of Applied Crystallography*, vol. 39, no. 5, pp. 735–738, 2006.

[50] K. Hayashi, N. Uchitomi, J. T. Asubar et al., "Three dimensional local structure analysis of ZnSnAs2:Mn by X-ray fluorescence holography," *Japanese Journal of Applied Physics*, vol. 50, no. 1S2, p. 1BF05, 2011.

[51] K. Kimura, K. Hayashi, L. V. Yashina et al., "Local structural analysis of In-doped Bi2 Se3 topological insulator using X-ray fluorescence holography," *Surface and Interface Analysis*, vol. 51, no. 1, pp. 51–55, 2019.

[52] S. Hosokawa, J. R. Stellhorn, T. Matsushita et al., "Impurity position and lattice distortion in a Mn-doped Bi2Te3 topological insulator investigated by x-ray fluorescence holography and x-ray absorption fine structure," *Physical Review B*, vol. 96, no. 21, p. 214207, 2017.

[53] J. R. Stellhorn, S. Hosokawa, N. Happo et al., "Local structure of the impurity site in Nd:LaF 3 by X-ray fluorescence

holography," *Physica Status Solidi (B)*, vol. 257, no. 11, p. 2000310, 2020.

[54] D. V. Novikov, B. Adams, T. Hiort et al., "X-ray holography for structural imaging," *Journal of Synchrotron Radiation*, vol. 5, no. 3, pp. 315–319, 1998.

[55] T. Gog, P. M. Len, G. Materlik, D. Bahr, C. S. Fadley, and C. Sanchez-Hanke, "Multiple-energy X-ray holography: atomic images of hematite (Fe2O3)," *Physical Review Letters*, vol. 76, no. 17, pp. 3132–3135, 1996.

[56] T. Gog, R. H. Menk, F. Arfelli, P. M. Len, C. S. Fadley, and G. Materlik, "X-ray holography with atomic resolution: trying to make it work," *Synchrotron Radiation News*, vol. 9, no. 3, pp. 30–35, 1996.

[57] B. Adams, Y. Nishino, and G. Materlik, "A novel experimental technique for atomic X-ray holography," *Journal of Synchrotron Radiation*, vol. 7, no. 4, pp. 274–279, 2000.

[58] K. Hayashi, M. Matsui, and Y. Awakura, "Local-structure analysis around dopant atoms using multiple energy x-ray holography," *Physical Review B*, vol. 63, no. 4, p. 041201, 2001.

[59] J. J. Barton, "Removing multiple scattering and twin images from holographic images," *Physical Review Letters*, vol. 67, no. 22, pp. 3106–3109, 1991.

[60] P. M. Len, S. Thevuthasan, C. S. Fadley, A. P. Kaduwela, and M. A. Van Hove, "Atomic imaging by x-ray-fluorescence holography and electron-emission holography: a comparative theoretical study," *Physical Review B*, vol. 50, no. 15, pp. 11275–11278, 1994.

[61] H. N. Chapman, S. P. Hau-Riege, M. J. Bogan et al., "Femtosecond time-delay X-ray holography," *Nature*, vol. 448, no. 7154, pp. 676–679, 2007.

[62] T. Wang, D. Zhu, B. Wu et al., "Femtosecond single-shot imaging of nanoscale ferromagnetic order inCo/PdMultilayers using resonant X-ray holography," *Physical Review Letters*, vol. 108, no. 26, p. 267403, 2012.

[63] K. Keskinbora, A. Levitan, and G. Schütz, "Maskless off-axis X-Ray holography," 2021, https://arxiv.org/abs/2101.12380.

[64] Y. Takahashi, K. Hayashi, and E. Matsubara, "Complex X-ray holography," *Physical Review B*, vol. 68, no. 5, p. 52103, 2003.

[65] Y. Takahashi, K. Hayashi, and E. Matsubara, "Elemental identification of a three-dimensional environment by complex x-ray holography," *Physical Review B*, vol. 71, no. 13, p. 134107, 2005.

[66] J. Kirz and D. Sayre, "Soft X-ray microscopy of biological specimens," *Synchrotron Radiation Research*, Springer, Boston, MA, USA, 1980.

[67] M. Howells, C. Jacobsen, J. Kirz, R. Feder, K. McQuaid, and S. Rothman, "X-ray holograms at improved resolution: a study of zymogen granules," *Science*, vol. 238, no. 4826, pp. 514–517, 1987.

[68] M. Bernhardt, J. D. Nicolas, and M. Osterhoff, "Correlative microscopy approach for biology using X-ray holography, X-ray scanning diffraction and STED microscopy," *Nature Communications*, vol. 9, no. 1, pp. 1–9, 2018.

[69] T. Gorkhover, A. Ulmer, K. Ferguson et al., "Femtosecond X-ray Fourier holography imaging of free-flying nanoparticles," *Nature Photonics*, vol. 12, no. 3, pp. 150–153, 2018.

[70] K. A. Nugent, H. N. Chapman, and Y. Kato, "Incoherent soft X-ray holography," *Journal of Modern Optics*, vol. 38, no. 10, pp. 1957–1971, 1991.

[71] M. R. Howells, B. Calef, and C. J. Jacobsen, "A modern approach to x-ray holography[C]//AIP Conference Proceedings," *American Institute of Physics*, vol. 507, no. 1, pp. 587–592, 2000.

[72] J. B. Murray, H. Szöke, A. Szöke, and W. G. Scott, "Capture and visualization of a catalytic RNA enzyme-product complex using crystal lattice trapping and X-ray holographic reconstruction," *Molecular Cell*, vol. 5, no. 2, pp. 279–287, 2000.

[73] A. Sato-Tomita, N. Shibayama, N. Happo et al., "Development of an X-ray fluorescence holographic measurement system for protein crystals," *Review of Scientific Instruments*, vol. 87, no. 6, p. 063707, 2016.

[74] J.-D. Nicolas, M. Bernhardt, M. Krenkel, C. Richter, S. Luther, and T. Salditt, "Combined scanning X-ray diffraction and holographic imaging of cardiomyocytes," *Journal of Applied Crystallography*, vol. 50, no. 2, pp. 612–620, 2017.

[75] A. Sato-Tomita, N. Happo, S.-Y. Park, K. Hayashi, Y. C. Sasaki, and N. Shibayama, "X-ray fluorescence holography for proteins: application to hemoglobin and myoglobin," *Biophysical Journal*, vol. 112, no. 3, p. 579a, 2017.

[76] D. Meyer-Ebrecht and H. Weiss, "Tomosynthesis-3-D X-ray imaging by means of holography or electronics," *Optica Acta: International Journal of Optics*, vol. 24, no. 4, pp. 293–303, 1977.

[77] A. T. Kuan, J. S. Phelps, L. A. Thomas et al., "Dense neuronal reconstruction through X-ray holographic nanotomography," *Nature Neuroscience*, vol. 23, no. 12, pp. 1637–1643, 2020.

[78] H. Madjidi-Zolbin and S. Jafari, "Cancer treatment by x-ray holography," *International Society for Optics and Photonics*, vol. 2887, pp. 84–90, 1996.

[79] Y. Nesterets, T. Gureyev, and A. Stevenson, "Soft tissue small avascular tumor imaging with x-ray phase-contrast micro-CT in-line holography," *Proceedings of SPIE-Tthe International Society for Optical Engineering*, vol. 6913, p. 69133Z, 2008.

[80] L. B. Dahlin, K. R. Rix, and V. A. Dahl, "Three-dimensional architecture of human diabetic peripheral nerves revealed by X-ray phase contrast holographic nanotomography," *Scientific Reports*, vol. 10, no. 1, pp. 1–8, 2020.

[81] B. De Samber, T. Vanden Berghe, E. Meul et al., "Nanoscopic X-ray imaging and quantification of the iron cellular architecture within single fibroblasts of Friedreich's ataxia patients," *Journal of Synchrotron Radiation*, vol. 27, no. 1, pp. 185–198, 2020.

[82] A. K. R. Ang, A. Sato-Tomita, N. Shibayama et al., "X-ray fluorescence holography for soft matter," *Japanese Journal of Applied Physics*, vol. 59, no. 1, p. 010505, 2020.

[83] M. Tegze, G. Faigel, S. Marchesini, M. Belakhovsky, and O. Ulrich, "Imaging light atoms by X-ray holography," *Nature*, vol. 407, no. 6800, p. 38, 2000.

[84] O. Hellwig, S. Eisebitt, W. Eberhardt, W. F. Schlotter, J. Lüning, and J. Stöhr, "Magnetic imaging with soft x-ray spectroholography," *Journal of Applied Physics*, vol. 99, no. 8, p. 08H307, 2006.

[85] A. Scherz, W. F. Schlotter, K. Chen et al., "Phase imaging of magnetic nanostructures using resonant soft x-ray holography," *Physical Review B*, vol. 76, no. 21, p. 214410, 2007.

[86] S. Streit-Nierobisch, D. Stickler, C. Gutt et al., "Magnetic soft x-ray holography study of focused ion beam-patterned Co/Pt multilayers," *Journal of Applied Physics*, vol. 106, no. 8, p. 83909, 2009.

[87] V. Chamard, J. Stangl, G. Carbone et al., "Three-dimensional X-ray fourier transform holography: the Bragg case," *Physical Review Letters*, vol. 104, no. 16, p. 165501, 2010.

[88] H. T. Kim, I. J. Kim, C. M. Kim et al., "Single-shot nanometer-scale holographic imaging with laser-driven x-ray laser," *Applied Physics Letters*, vol. 98, no. 12, p. 121105, 2011.

[89] Z. Jiang, J. W. Strzalka, and D. A. Walko, "Reconstruction of evolving nanostructures in ultrathin films with X-ray waveguide fluorescence holography," *Nature Communications*, vol. 11, no. 1, pp. 1–10, 2020.

[90] T. Sekioka, K. Hayashi, E. Matsubara et al., "Atomic imaging in EBCO superconductor films by an X-ray holography system using a toroidally bent graphite analyzer," *Journal of Synchrotron Radiation*, vol. 12, no. 4, pp. 530–533, 2005.

[91] N. Happo, K. Hayashi, S. Senba, H. Sato, M. Suzuki, and S. Hosokawa, "Distorted and undistorted atomic sites in a ferromagnetic semiconductor Ge0.6Mn0.4Te film determined by X-ray fluorescence holography," *Journal of the Physical Society of Japan*, vol. 83, no. 11, p. 113601, 2014.

[92] K. Hayashi, N. Uchitomi, K. Yamagami et al., "Large as sublattice distortion in sphalerite ZnSnAs2 thin films revealed by x-ray fluorescence holography," *Journal of Applied Physics*, vol. 119, no. 12, p. 125703, 2016.

[93] J. F. Scott, "Applications of modern ferroelectrics," *Science*, vol. 315, no. 5814, pp. 954–959, 2007.

[94] K. Hayashi, C. Lu, A. K. R. Ang et al., "Local structure analysis around Ti in lead zirconate titanate by X-ray fluorescence holography," *Physica Status Solidi (B)*, vol. 257, no. 11, p. 2000191, 2020.

[95] J. Villanova, J. Laurencin, P. Cloetens et al., "3D phase mapping of solid oxide fuel cell YSZ/Ni cermet at the nanoscale by holographic X-ray nanotomography," *Journal of Power Sources*, vol. 243, pp. 841–849, 2013.

[96] E. Lay-Grindler, J. Laurencin, J. Villanova et al., "Degradation study by 3D reconstruction of a nickel-yttria stabilized zirconia cathode after high temperature steam electrolysis operation," *Journal of Power Sources*, vol. 269, pp. 927–936, 2014.

[97] M. Hubert, J. Laurencin, P. Cloetens, B. Morel, D. Montinaro, and F. Lefebvre-Joud, "Impact of Nickel agglomeration on solid oxide cell operated in fuel cell and electrolysis modes," *Journal of Power Sources*, vol. 397, pp. 240–251, 2018.

[98] G. Delette, J. Laurencin, F. Usseglio-Viretta et al., "Thermoelastic properties of SOFC/SOEC electrode materials determined from three-dimensional microstructural reconstructions," *International Journal of Hydrogen Energy*, vol. 38, no. 28, pp. 12379–12391, 2013.

[99] J. Villanova, P. Cloetens, H. Suhonen et al., "Multi-scale 3D imaging of absorbing porous materials for solid oxide fuel cells," *Journal of Materials Science*, vol. 49, no. 16, pp. 5626–5634, 2014.

[100] T. T. Nguyen, J. Villanova, Z. Su et al., "3D quantification of microstructural properties of LiNi 0.5 Mn 0.3 Co 0.2 O 2 high-energy density electrodes by X-ray holographic nanotomography," *Advanced Energy Materials*, vol. 11, no. 8, p. 2003529, 2021.

[101] L. A. Turnbull, M. T. Birch, A. Laurenson et al., "Tilted X-ray holography of magnetic bubbles in MnNiGa lamellae," *ACS Nano*, vol. 15, no. 1, pp. 387–395, 2020.

[102] R. Blukis, B. Pfau, and C. M. Günther, "Nanoscale imaging of high-field magnetic hysteresis in meteoritic metal using X-ray holography," *Geochemistry, Geophysics, Geosystems*, vol. 21, no. 8, p. e2020GC009044, 2020.

Hindawi
International Journal of Optics
Volume 2021, Article ID 6493130, 7 pages
https://doi.org/10.1155/2021/6493130

Research Article

Super-Resolution and Large Depth of Field Model for Optical Microscope Imaging

Ruo-Peng Zheng, Shu-Bin Liu, and Lei Li

School of Electronics and Information Engineering, Sichuan University, Chengdu 610065, China

Correspondence should be addressed to Lei Li; leili@scu.edu.cn

Received 24 November 2021; Accepted 11 December 2021; Published 29 December 2021

Academic Editor: Paramasivam Senthilkumaran

Due to the limitation of numerical aperture (NA) in a microscope, it is very difficult to obtain a clear image of the specimen with a large depth of field (DOF). We propose a deep learning network model to simultaneously improve the imaging resolution and DOF of optical microscopes. The proposed M-Deblurgan consists of three parts: (i) a deblurring module equipped with an encoder-decoder network for feature extraction, (ii) an optimal approximation module to reduce the error propagation between the two tasks, and (iii) an SR module to super-resolve the image from the output of the optimal approximation module. The experimental results show that the proposed network model reaches the optimal result. The peak signal-to-noise ratio (PSNR) of the method can reach 37.5326, and the structural similarity (SSIM) can reach 0.9551 in the experimental dataset. The method can also be used in other potential applications, such as microscopes, mobile cameras, and telescopes.

1. Introduction

In microscopy, it is very difficult to obtain a clear image of the specimen with a large depth of field (DOF), especially for large NA. Usually, optical axial scanning is used to solve the problem. However, it is time-consuming. With the rapid development of deep learning in computer vision and image processing, it is possible to use deep learning algorithms to obtain a clear image of the specimen with a large DOF. For example, the super-resolution (SR) and deblurring algorithms are used to improve the resolution of images [1–9]. Recently, the deep learning single-image super-resolution (SISR) model [10–12] and convolutional neural network (CNN) model [13] have been applied to improve the resolution and definition in microscope images, which indicates that they have great potential in microscopes. However, compared with the application of SISR in enhancing the texture of real images, the SR microscopic images have higher requirements for the predicted image fineness. Therefore, it is still an uncertain problem that the SR image based on deep learning is better than the traditional SR microscope [14–16] in many scenarios. Public image deblurring methods in deep learning simply solve the blur caused by the point-spread function (PSF) of the optical microscope [17], while the problem of the blurred microscope images due to insufficient DOF needs to be solved urgently. For example, traditional SR microscopes such as localization microscopy [14], STED microscopy [15], and structured illumination microscopy (SIM) [16] provide great convenience to observe the internal work of cells and various biological processes. However, it needs a relatively more complicated experimental setup and requires a priori knowledge about the sample and its preparation. An SR confocal microscope based on deep learning is proposed to improve the resolution of the image [18], but this method is based on photoactivated localization microscopy (PALM), and it is difficult to generalize it in various microscopic imaging systems. An SR microscope based on generative adversarial networks (GAN) enhances the textures of macroscale realistic photographs, but the fineness is far from the requirements of microscopic imaging [19]. An SR microscope based on deep neural networks has greater accuracy and quantifiability of the inferred nanoscale structure [20]. But the blur inherent in low-resolution (LR) images is

still unresolved. A deblur microscope based on CNN is proposed to remove the blur caused by PSF [17]. This method ignores the blur caused by the insufficient DOF. Therefore, it is urgent to realize to study a microscope with both SR and large DOF functions.

In this paper, we propose a generative adversarial neural network framework model (M-Deblurgan) based on the optimal approximation, which is to simultaneously solve the low-resolution and insufficient depth of field in an optical microscope. M-Deblurgan is composed of a generator network and a discriminator network that have a competitive relationship. The generator network comprises three modules: deblurring module, optimal approximation module, and SR module. The robustness of the model on the publicly available dataset and experimental dataset are tested. The PSNR of the method can reach 37.5326, and the SSIM can reach 0.9551 in the experimental dataset, which shows the deblurred results and resolution are improved compared to other models.

2. Proposed Method

The proposed method is shown in Figure 1. The proposed deep learning network structure follows the GAN framework [21], which has two subnetworks trained at the same time. One is a generator network that makes LR microscopic blurred images become high-resolution clear microscopic images, and the other is a discriminator network that distinguishes the image generated by the generator from the real image.

2.1. Network Structure. The generator network is shown in Figure 1(a). We integrate the ideas of residual network and encoder-decoder network into the joint task of microscopic image deblurring and SR. The generator network consists of a deblurring module, an optimal approximation module, and an SR module.

In the deblurring module, we propose an improved encoder-decoder network as our deblurring module and use the improved method as a lightweight option to incorporate multiscale features. The architecture consists of an encoder-decoder network, and we output the final feature maps of five different scales during the upsampling process. The encoder is made up of a 5×5 flat-convolutional layer and four 3×3 Res-Blocks. To broaden the perceptual field and learn high-dimensional representations, the encoder component employs three pooling layers. Three 3×3 upsampling layers and three 3×3 Res-Blocks make up the decoder component, which gradually increases the size of the feature map to the original input resolution. Between the encoder and the decoder, we added four skip connections. These connections can hasten the network's convergence and result in significantly crisper outputs. To avoid adding too many fuzzy features from the encoder side, we additionally use a 3×3 flat-convolution layer before element-wise addition. These feature maps of different scales are sampled to the same 1/4 input size and connected into a tensor that contains rich image texture information of different scales.

There are two upsampling and convolutional layers at the end of the network, which can make the output size of the deblurring module equal to the input size and reduce artifacts. We have also made some improvements to the residual block. We removed the batch normalization layer in ResBlock compared to the original ResNet. The batch normalization layer normalizes the properties of specific jobs, increases the amount of computation, and lowers the flexibility of the network.

In the optimal approximation module, firstly, this module can avoid the accumulation of errors due to the simple series connection of the deblurring module and the SR module, that is, to prevent the estimation error of the first model from being further propagated and amplified in the second model. Secondly, it makes full use of the correlation between the two tasks. The main formulas used in our optimal approximation method are as follows:

$$F(x_i) = \frac{1}{e^{|x_i - z|}}. \tag{1}$$

Among them,

$$Z = \frac{\|(x_1, \ldots, x_i, \ldots, x_N)\|_2}{N}. \tag{2}$$

N in equation (2) represents the number of inputs, and x_i represents the i-th input. N in this network is 3. $(x_1, \ldots, x_i, \ldots, x_N)$ represents the set of inputs, which represents the input image, the output of the encoder-decoder network, and the output of the deblurring module in the proposed network, respectively. The two formulas are mainly used to determine which of the 3 inputs is closest to the actual optimal input. The input picture and the output of the feature module are connected to the optimal approximation module in a jump connection. Through the screening of the optimal approximation module, the data of the one closest to the real picture can be output. The forward and backward jump connections can minimize the influence of the front network error on the backpropagation and reduce the network coupling.

In the super-resolution module, the output of the optimal approximation module is used as the input of the SR module. The model has three fully connected layers (FC) with a core size of 3. Then, the feature map resolution is improved by two trainable 2x subpixel convolutional layers. The model adds a convolutional layer with a core size of 3 at the tail to convert the features to the RGB image and remove redundant artifacts. We add residual learning to the super-resolution module and add a global jump connection to jointly reconstruct the super-resolution image, making the final image closer to the real image.

The input of the discriminator is composed of the image generated by the generator and the real image, and the output is the probability that the image generated by the generator is the real image. The network structure is shown in Figure 1(b). The network is similar to the VGG network, which uses step-size convolution to downsample the image while doubling the number of feature maps. Except for the sigmoid function used in the last layer, the Leaky ReLU (LR)

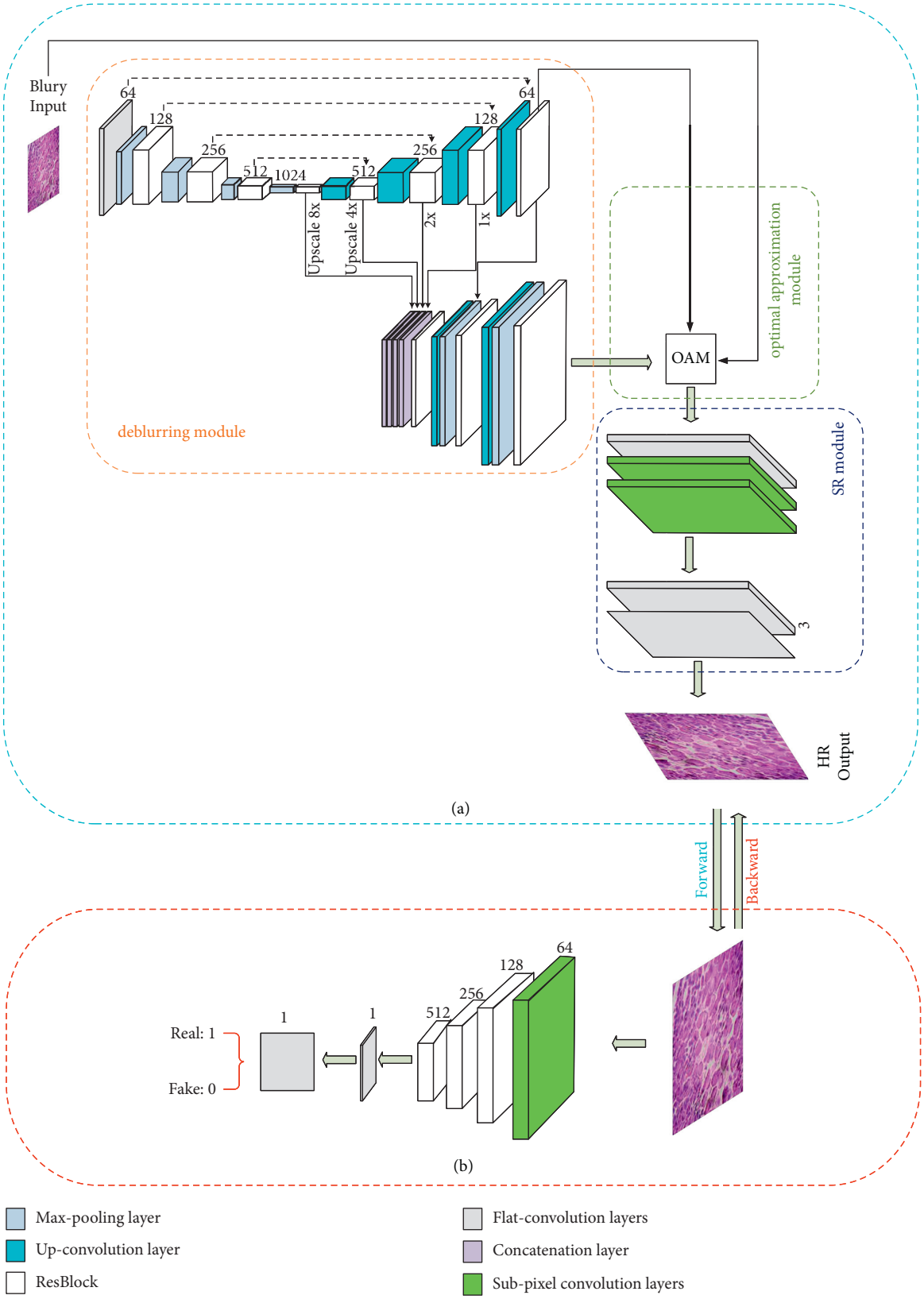

Figure 1: M-Deblurgan pipeline architecture. (a) Generator network. (b) Discriminator network.

activation function with a slope of 0.2 is used after the other layers. Besides, we use a global average pooling layer to replace the first fully connected layer, which can prevent overfitting and reduce the number of parameters in the model training process.

2.2. Network Loss. The designed objective function is the combination of three different loss functions in M-Deblurgan: pixel-wise mean squared error (MSE) loss (L_{MSE}), perceptual loss (L_{percep}), and SSIM loss (L_{SSIM}). In the proposed method, the MSE loss is calculated as follows:

$$L_{\mathrm{MSE}} = \frac{1}{N}\sum_{i=1}^{N}\left(\left\|G_1\left(F\left(I_i^{LR}\right)\right) - I_i^{L\acute{R}}\right\|^2 + \left\|G_2\left(I_i^{D}\right) - I_i^{\mathrm{HR}}\right\|^2\right). \tag{3}$$

Among them, I_i^{LR} $I_i^{L\acute{R}}$, I_i^{D}, and I_i^{HR} represent LR microscopically blurred images, LR clear images, deblurred images, and high-resolution clear images, respectively. F represents the feature extraction module, G_1 represents the deblurring module, and G_2 represents the SR module. The perceptual loss is calculated as follows:

$$L_{\mathrm{percep}} = \frac{1}{W_{i,j}H_{i,j}}\sum_{x=1}^{W_{i,j}}\sum_{y=1}^{H_{i,j}}\left(\varphi_{i,j}\left(I^{\mathrm{HR}}\right)_{x,y} - \varphi_{i,j}\left(G\left(I^{\mathrm{LR}}\right)\right)_{x,y}\right)^2. \tag{4}$$

Among them, $\phi_{i,j}$ represents the feature map output in the i-th pooling layer, and the j-th convolutional layer after the image is input to the pretrained VGG19 network model. $W_{i,j}$ and $H_{i,j}$ represent the dimension of the feature map. Specifically, we aim to minimize from the following equation:

$$\begin{aligned} L(G;D) &= L_{\mathrm{MSE}} + \alpha\left(L_{\mathrm{percep}}\right) \\ &\quad - \beta\log\left|\frac{\left(1 + \mathrm{SSIM}\left(G\left(I^{\mathrm{LR}}\right), y\right)\right)}{2}\right|, \end{aligned} \tag{5}$$

where $G(I^{\mathrm{LR}})$ is the generative model output, D (.) is the predicted result of the discriminator, and y is the HR image used as ground truth. Since the images generated by the model often have unsatisfactory artifacts and excessively smooth textures, α and β were set to accommodate the MSE loss and the SSIM loss to be ~5–15% of the combined generator model loss $L(G;D)$.

3. Experimental Results and Analysis

The proposed model is trained and tested on a PC (Intel Core i7-10750H CPU @2.6 GHz + RTX1660Ti) equipped with the Windows10 operating system and is based on the platform of PyTorch 1.7.0. We set the learning rate to 10^{-4} in the first 150 epochs and linearly decayed to 10^{-7} in the subsequent 50 epochs.

The FIRE (https://www.ics.forth.gr/cvrl/fire/) dataset is used as the simulated dataset for the training and testing of the proposed network. We cropped the dataset into 5360 images with a size of 512 × 512, of which 4840 images are used for training and 520 images are used for testing. For training, the training dataset is down-sampled 4 times through bicubic interpolation to obtain an LR image with a spatial resolution of 256 × 256. Finally, the blurry LR inputs are generated by applying a Gaussian kernel. The proposed network model processes a 256 × 256 blurry LR input and outputs an SR and a clear image of 512 × 512 size. The results of the experiment are shown in Figure 2. Figure 2(a) is an original uncropped image. Figures 2(b), 2(d), and 2(f) represent the enlarged images of the red frame region enclosed in Figure 2(a). Figures 2(c), 2(e), and 2(g) represent the enlarged images of the blue frame region enclosed in Figure 2(a). Figures 2(b) and 2(c) are blurry LR inputs. By using Figures 2(b) and 2(c) as the model input, the output is the clear SR images shown in Figures 2(d) and 2(e). From the experimental results, Figures 2(d) and 2(e) remove the blur of small blood vessels and improve the resolution of the image (as indicated by the red and blue arrows). The restored image is very close to the ground truth (Figures 2(f) and 2(g)) in terms of details and intensity information.

Our model performs very well in the simulated dataset. It is very necessary to use the PINE CONES dataset collected in a real and complex experimental environment to verify the quality of the model. The experimental image acquisition and processing process is shown in Figure 3.

Microscopic defocused images of female pine cones are obtained by the ×5 objective lens of a biological microscope. At the same time, the clear images of the corresponding ×10 objective are obtained as the ground truth for model training. The experimental observation device is shown in Figure 4. The specimen is the female pine cones. We train and test our proposed model and other SR and deblurring methods on the PINE CONES dataset. The results are shown in Figure 5. Figure 5(a) is obtained by the ×5 objective with the process of the defocused blur. Figures 5(b)–5(d) are the images obtained by processing Figure 5(a) with the RL-Decov + SR method [22], the U-net + SR method [23], and our method, respectively. Figure 5(e) is obtained by the ×10 objective. Figures 5(f) and 5(j) and 5(k)–5(o) are the enlarged images of two same areas in Figures 5(a)–5(e), respectively. These areas are pointed out in Figures 5(a)–5(e) using solid red and blue frames. It can be seen from the enlarged image Figures 5(f)–5(o) that there are serious distortions in the restoration of blurry LR images through the RL-Decov + SR and U-net + SR methods. The cell image recovered by the RL-Decov + SR method is shown in Figures 5(g) and 5(l). It is not difficult to find that the nucleus and the cell wall are diffused. The cell image recovered by the U-net + SR method is shown in Figure 5(h) with unsatisfactory artifacts, and the sharpening of the cell wall is not enough in Figure 5(m). However, the processed image in Figure 5(d), obtained using our method, is similar to Figure 5(e).

The model proposed in this paper reconstructs a clear and high-resolution image when the input is a low-resolution microscopic blurred image while maintaining a small model size. In the prediction phase, the results can be output quickly. When reconstructing the image, only the generator network model is required. Since the generator of the proposed method belongs to a fully convolutional neural

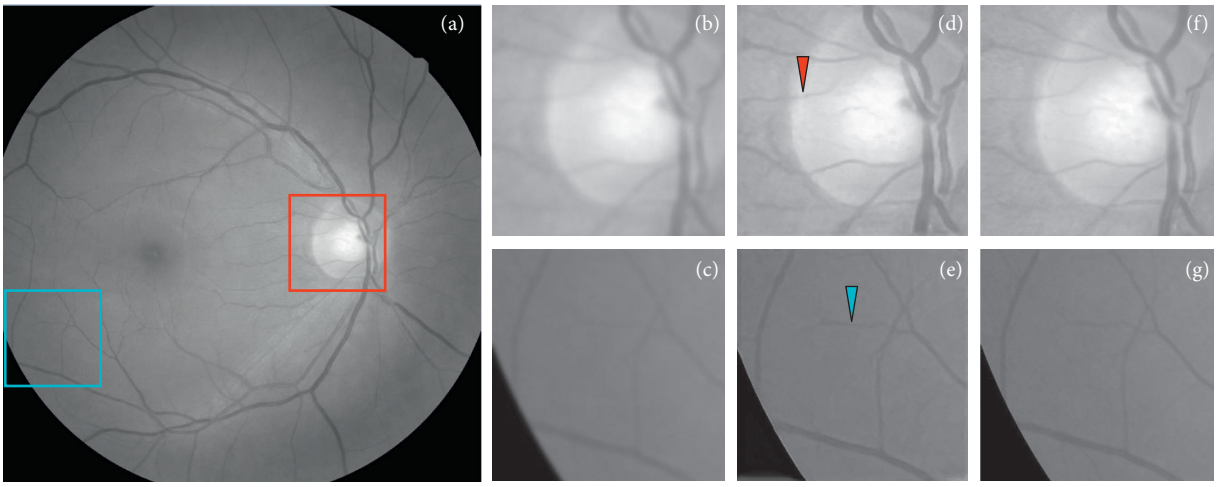

Figure 2: Experimental results on the simulated dataset. (a) Original uncropped image. (b, c) Blurry LR input. (d, e) The images processed by our method. (f, g) Ground truth. (b, d, f) Enlarged images of the red frame region enclosed in (a). (c, e, g) Enlarged images of the blue frame region enclosed in (a). Red arrow and blue arrow in (d) and (e) indicate the sharpened small blood vessels with our method.

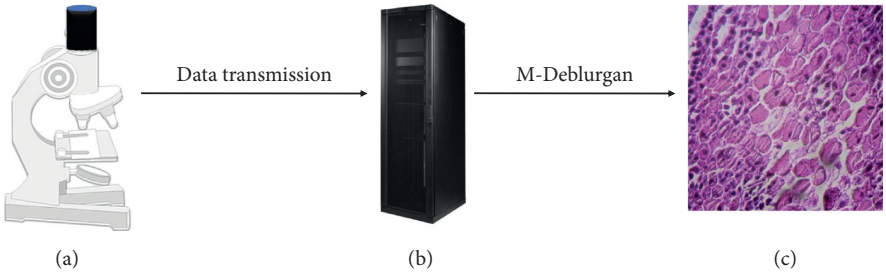

Figure 3: Experimental data acquisition and processing setup. (a) Optical microscope. (b) Computer. (c) Processed image.

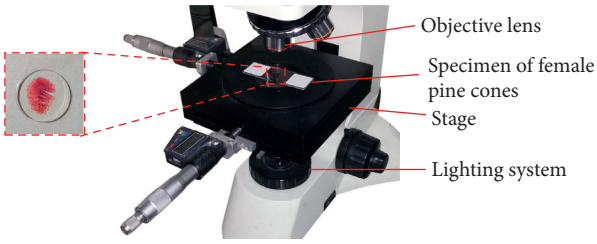

Figure 4: Experimental observation device.

network, the size of the input images is not limited. As shown in Figure 5, our proposed method can generate clearer images under real microscope observation scenes and has stronger robustness than other methods.

To measure the quantitative performance of the proposed network, we considered conventional indicators, namely, PSNR and SSIM. Table 1 is the quantitative comparison between the proposed method and other methods in the testing phase. The results show that the performance of the proposed network is superior to the existing methods in terms of PSNR and SSIM, with an increase of 4.8033 dB and 0.053 dB on the PINE CONES dataset. By introducing the optimal approximation module, the performance of the proposed network is greatly improved.

Comparing the U-net + SR model and our model in Figure 6, these two models performed similarly in the initial training stage. When the epoch is close to 200, the PSNR of M-Deblurgan is 2.7 dB higher than that of another model. The result demonstrates the superiority of the proposed model. Combining the data in Figure 7, it is not difficult to find that the proposed method has fewer parameters and higher PSNR values than other deep learning models. Fewer parameters will lead to less computer video memory consumption and improve the training efficiency of the model. Therefore, the M-Deblurgan is more robust. From the quantitative comparison, we can draw the conclusion that the M-Deblurgan based on the optimal approximation module is conducive to generating clearer and higher perceptual images.

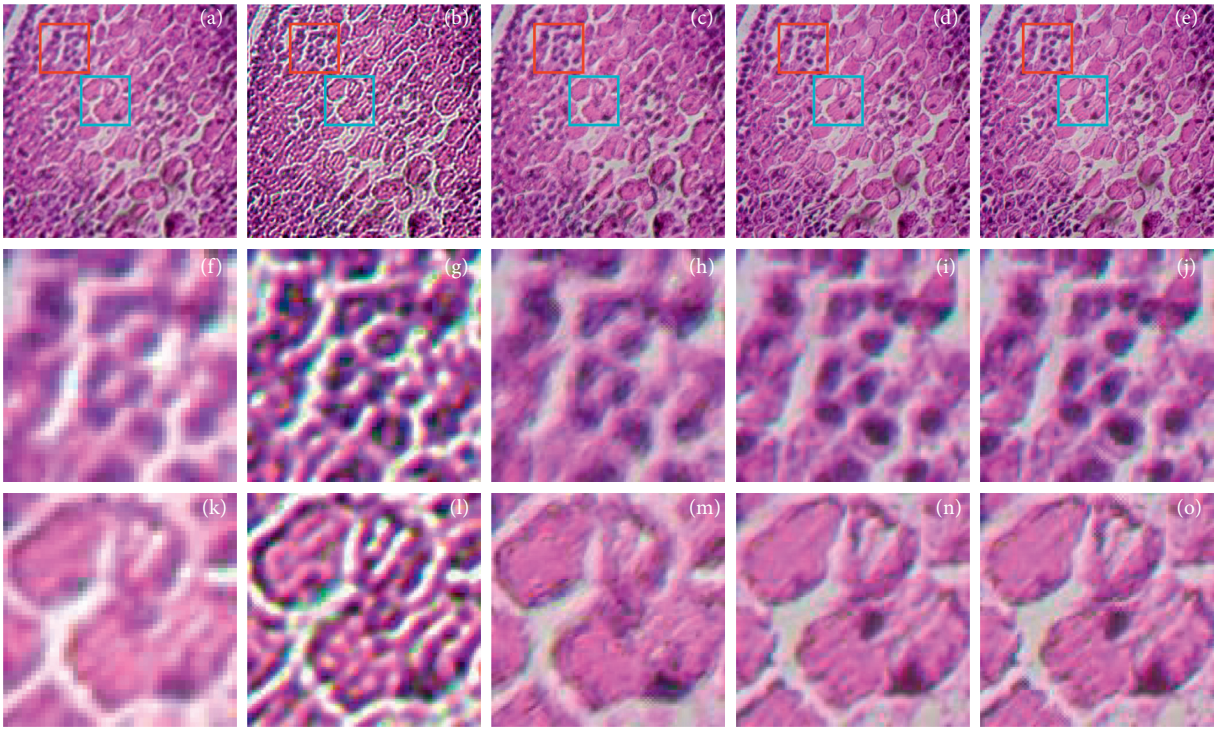

Figure 5: Experimental results on the PINE CONES dataset. (a) Image obtained by the ×5 objective with the process of the defocused blur. (b–d) Processed image of (a) by the RL-Decov + SR, U-net + SR, and our method, respectively. (e) Images obtained by the ×10 objective. (f–j) Enlarged images of the solid red region enclosed in (a–e), respectively. (k–o) Enlarged images of the solid blue region enclosed in (a–e), respectively.

Table 1: Quantitative comparison with other methods on the test dataset.

Method	FIRE		PINE CONES	
	PSNR	SSIM	PSNR	SSIM
RL-Decov + SR	26.1325	0.8034	25.2356	0.7822
U-net + SR	33.6004	0.9138	32.7293	0.9021
Ours	38.5014	0.9736	37.5326	0.9551

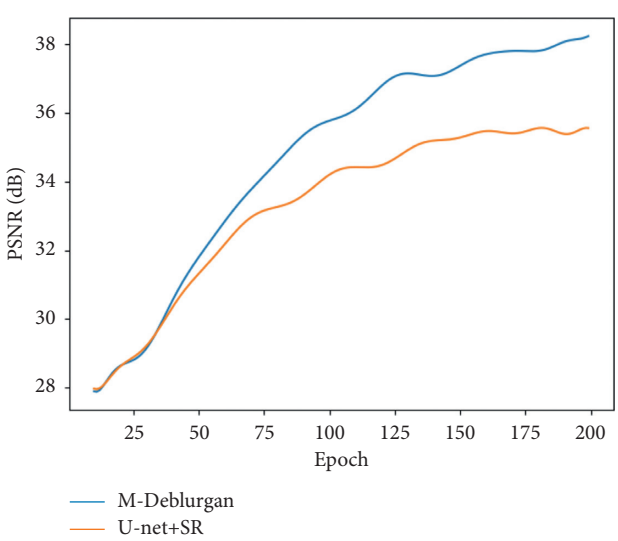

Figure 6: Quantitative analysis of two different deep learning methods on the training process.

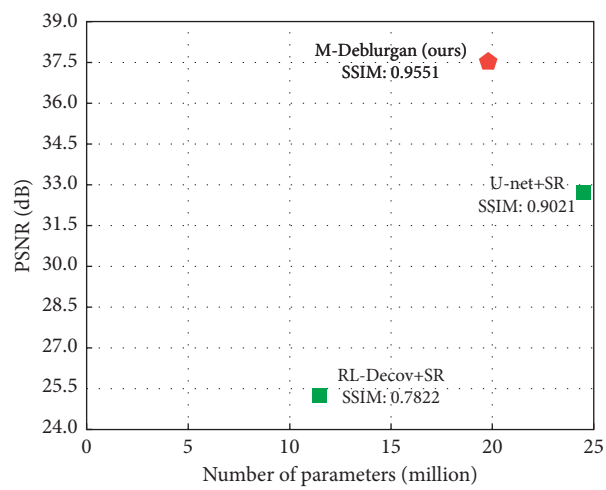

Figure 7: Comparison of PSNR and the model size of other methods on the PINE CONES dataset. The red pentagon is our method.

4. Conclusion

In this paper, we propose a deep learning model (M-Deblurgan) to improve the imaging resolution and DOF of traditional optical microscopes. The M-Deblurgan doesn't require any manual manipulation of the PINE CONES dataset during the training process. Furthermore, the clear SR output can be obtained quickly when the blurry LR microscopic images are used as input. The experimental

results show that our proposed method, especially the optimal approximation module, overcomes the limitations of the simple combination of deblurring and super-resolution tasks. The experiments show that the peak signal-to-noise ratio (PSNR) of our method can reach 37.5326, and the structural similarity (SSIM) can reach 0.9551 in the experimental dataset. The experimental results show that the model is superior to existing methods in objective indicators such as visual quality and PSNR.

Data Availability

The data used to support the findings of this study are included within the article.

Conflicts of Interest

The authors declare that they have no conflicts of interest.

Acknowledgments

This work was supported by the National Natural Science Foundation of China (61975139 and 61927809).

References

[1] J. Cai, H. Zeng, H. Yong, Z. Cao, and L. Zhang, "Toward real-world single image super-resolution: a new benchmark and a new model," in *Proceedings of the IEEE/CVF International Conference on Computer Vision*, pp. 3086–3095, Seoul, South Korea, October 2019.

[2] Y. Huang, Z. Lu, Z. Shao et al., "Simultaneous denoising and super-resolution of optical coherence tomography images based on generative adversarial network," *Optics Express*, vol. 27, no. 9, pp. 12289–12307, 2019.

[3] Y. Kageyama, M. Isogawa, D. Iwai, and K. Sato, "ProDebNet: projector deblurring using a convolutional neural network," *Optics Express*, vol. 28, no. 14, pp. 20391–20403, 2020.

[4] O. Kupyn, V. Budzan, M. Mykhailych, D. Mishkin, and J. Matas, "Deblurgan: blind motion deblurring using conditional adversarial networks," in *Proceedings of the IEEE Conference on Computer Vision and Pattern Recognition*, pp. 8183–8192, Salt Lake City, UT, USA, June 2018.

[5] Z. Luo, A. Yurt, R. Stahl et al., "Pixel super-resolution for lens-free holographic microscopy using deep learning neural networks," *Optics Express*, vol. 27, no. 10, pp. 13581–13595, 2019.

[6] Z. Niu, J. Shi, L. Sun, Y. Zhu, J. Fan, and G. Zeng, "Photon-limited face image super-resolution based on deep learning," *Optics Express*, vol. 26, no. 18, pp. 22773–22782, 2018.

[7] W.-Z. Shao, Y.-Y. Liu, L.-Y. Ye et al., "DeblurGAN+: revisiting blind motion deblurring using conditional adversarial networks," *Signal Processing*, vol. 168, Article ID 107338, 2020.

[8] R. Strack, "Deep learning advances super-resolution imaging," *Nature Methods*, vol. 15, no. 6, p. 403, 2018.

[9] H. Sim and M. Kim, "A deep motion deblurring network based on per-pixel adaptive kernels with residual down-up and up-down modules," in *Proceedings of the IEEE/CVF Conference on Computer Vision and Pattern Recognition Workshops*, p. 0, Long Beach, CA, USA, June 2019.

[10] C. Belthangady and L. A. Royer, "Applications, promises, and pitfalls of deep learning for fluorescence image reconstruction," *Nature Methods*, vol. 16, no. 12, pp. 1215–1225, 2019.

[11] H. Wang, Y. Rivenson, Y. Jin et al., "Deep learning enables cross-modality super-resolution in fluorescence microscopy," *Nature Methods*, vol. 16, no. 1, pp. 103–110, 2019.

[12] M. Weigert, U. Schmidt, T. Boothe et al., "Content-aware image restoration: pushing the limits of fluorescence microscopy," *Nature Methods*, vol. 15, no. 12, pp. 1090–1097, 2018.

[13] O. Abdel-Hamid, A.-r. Mohamed, H. Jiang, L. Deng, G. Penn, and D. Yu, "Convolutional neural networks for speech recognition," *IEEE/ACM Transactions on audio, speech, and language processing*, vol. 22, no. 10, pp. 1533–1545, 2014.

[14] M. G. L. Gustafsson, "Surpassing the lateral resolution limit by a factor of two using structured illumination microscopy. short communication," *Journal of Microscopy*, vol. 198, no. 2, pp. 82–87, 2000.

[15] S. W. Hell and J. Wichmann, "Breaking the diffraction resolution limit by stimulated emission: stimulated-emission-depletion fluorescence microscopy," *Optics Letters*, vol. 19, no. 11, pp. 780–782, 1994.

[16] S. Van de Linde, A. Löschberger, T. Klein et al., "Direct stochastic optical reconstruction microscopy with standard fluorescent probes," *Nature Protocols*, vol. 6, no. 7, pp. 991–1009, 2011.

[17] P. Sarder and A. Nehorai, "Deconvolution methods for 3-D fluorescence microscopy images," *IEEE Signal Processing Magazine*, vol. 23, no. 3, pp. 32–45, 2006.

[18] W. Ouyang, A. Aristov, M. Lelek, X. Hao, and C. Zimmer, "Deep learning massively accelerates super-resolution localization microscopy," *Nature Biotechnology*, vol. 36, no. 5, pp. 460–468, 2018.

[19] C. Qiao, D. Li, Y. Guo et al., "Evaluation and development of deep neural networks for image super-resolution in optical microscopy," *Nature Methods*, vol. 18, no. 2, pp. 194–202, 2021.

[20] H. Zhao, Z. Ke, N. Chen et al., "A new deep learning method for image deblurring in optical microscopic systems," *Journal of Biophotonics*, vol. 13, Article ID e201960147, 2020.

[21] I. J. Goodfellow, J. Pouget-Abadie, M. Mirza et al., "Generative adversarial networks," *Advances in Neural Information Processing Systems*, vol. 3, pp. 2672–2680, 2014.

[22] M. Ingaramo, A. G. York, E. Hoogendoorn, M. Postma, H. Shroff, and G. H. Patterson, "Richardson-lucy deconvolution as a general tool for combining images with complementary strengths," *ChemPhysChem*, vol. 15, no. 4, pp. 794–800, 2014.

[23] O. Ronneberger, P. Fischer, and T. Brox, "U-net: convolutional networks for biomedical image segmentation," in *Medical Image Computing and Computer-Assisted Intervention, Pt Iii, Lecture Notes in Computer Science*, N. Navab, J. Hornegger, W. M. Wells, and A. F. Frangi, Eds., Springer International Publishing Ag, New York, NY, USA, 2015.

Hindawi
International Journal of Optics
Volume 2021, Article ID 3161498, 5 pages
https://doi.org/10.1155/2021/3161498

Research Article

Parallax Barrier for Weakening Vernier Fringe in Naked-Eye LED 3D Display

Hong-Ran Zeng and Wu-Xiang Zhao

School of Electronic and Information Engineering, Sichuan University, Chengdu 610065, China

Correspondence should be addressed to Wu-Xiang Zhao; zhaowuxiang@scu.edu.cn

Received 31 July 2021; Accepted 4 December 2021; Published 22 December 2021

Academic Editor: E. Bernabeu

In naked-eye LED 3D display, vernier fringe is apparent for a conventional parallax barrier. This paper presents an intended misplaced parallax barrier with discrepant width of Light Translucent Slits (LTSs) to weaken vernier fringe. Because of the wild Black Matrix (BM) of LED display, which causes apparent vernier fringe, we enlarge the width of the LTS and move the slits properly in their periods. This structure increases the periodic difference between the parallax barrier and pixel of the LED display, which can increase the brightness of the diazone of vernier fringe and make it to appear more sparsely. In this way, vernier fringe produced by those two periods is weakened at the condition that no obvious crosstalk of stereoimages is increased. The performances of simulation and experimental display prototype show that the diazone of vernier fringe is faded and obviously sparser in the naked-eye LED 3D display. As a result, vernier fringe of this display is significantly decreased and not visible for viewing.

1. Introduction

Naked-eye 3D display technologies do not need any accessory such as stereo glasses and is currently a research hotspot in the field of display [1, 2]. Among them, the LCD-based parallax barrier naked-eye 3D display is a popular experimental scheme with simple structure, easy realization, and low cost, which has become a relatively mature product in recent years [3–7]. However, the LCD display screen is hard to be enlarged due to its low brightness, while the LED screen is suitable for large-screen display due to its high brightness, large size, and bright color [8–12]. For the traditional vertical parallax barrier design, the LTS is placed parallel to the column pixels of the display screen [13, 14]. When the eye sight captures the BM, which is the nonluminous part between adjacent subpixels, through the LTS, it will generally trigger the obvious periodic black and white gradient slits, named as vernier fringe [15–17], bringing discomfort to the viewers and seriously affecting the display effect. The use of an oblique parallax barrier can impair vernier fringe, but it will significantly increase the crosstalk of the stereoimage [18–21]. In order to reduce the discomfort brought by vernier fringe and not significantly increase crosstalk, this paper proposes a designing method of misplaced parallax barrier with nonuniform width of the LTS based on the wide characteristics of BM of the LED screen [22]. By appropriately increasing the width of the LTS of the parallax barrier and moving it during the period, the difference between the periodic structure of the parallax barrier and the pixel periodic structure of the LED screen can be increased, so as to reduce the correlation between the spectral element and the display screen [23] and further enhance the brightness of diazone in vernier fringe and make it sparse. Therefore, the proposed method can attenuate the vernier fringe without obvious introduction of crosstalk of the stereoimage.

2. The Structure and Principles of the Parallax Barrier Naked-Eye 3D Display

We take the front-parallax barrier naked-eye 3D displayer based on the LED screen as an example to illustrate the inner structure and principle [24], which are shown in Figure 1. We set the spacing among adjacent pixels in the LED screen

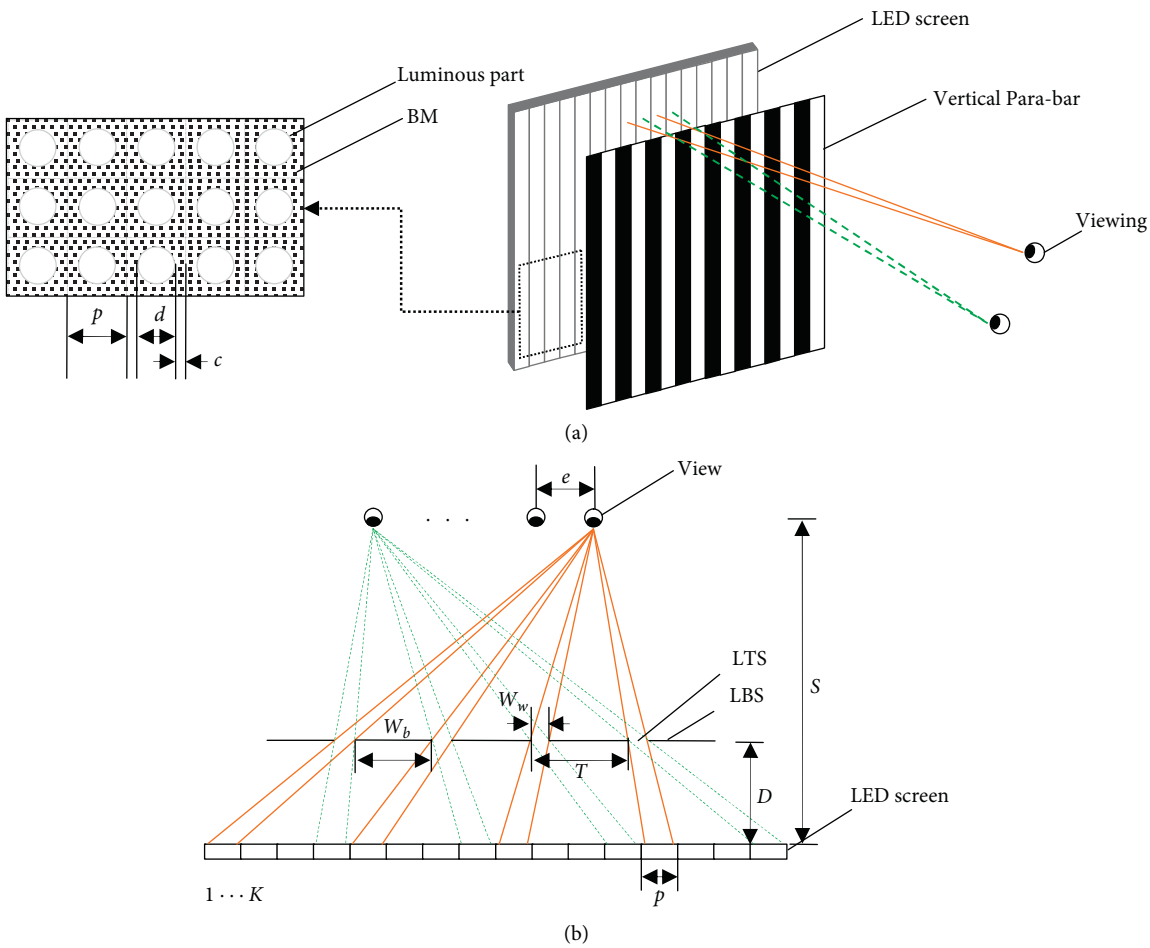

Figure 1: Naked-eye 3D display based on the parallax barrier. (a) Structure; (b) principle of beam split.

as p, the width of the LTS of the parallax barrier (parabar) as W_w, Light Blocking Slit (LBS) width as W_b, period as $T = W_w + W_b$, optimal viewing distance as S, and the distance between adjacent viewpoints as e, according to the average human pupil distance. In terms of the triangle similarity principle, the relationship between the abovementioned parameters can be given by

$$D = \frac{p \cdot S}{e + p}, \tag{1}$$

$$W_w = \frac{p \cdot e}{e + p}, \tag{2}$$

$$T = \frac{K \cdot e \cdot p}{e + p}. \tag{3}$$

3. Design of a Misplaced Parallax Barrier with Nonuniform LTS Width

In the parallax barrier naked-eye 3D display, since the pixels of the 2D displaying board are arranged in an orderly periodic matrix structure, the light of pixels interferes with the periodic parallax barrier in front of the pixel panel to form obvious vernier fringe, which makes the 3D display effect terrible to watch. Thus, in order to weaken the vernier fringe from the traditional vertical parallax barrier, this paper proposes a designing method of the parallax barrier with nonuniform width of LTS. As shown in Figure 2, the pixel spacing of the LED screen is denoted as $p = 2.5$ mm and the white disc, whose diameter equals to 1.5 mm, represents the actual luminous part of the pixel. In addition, half width of the BM is set as 0.5 mm, noted by $c = 0.5$ mm, and the number of viewing point is set to $K = 5$. Also, the viewing distance S is defined as 4 m, and the adjacent distance of viewing points e is 65 mm.

First and foremost, three important parameters of the traditional vertical parallax barrier, LTS width, period, and distance from the parallax barrier to the LED screen, can be obtained by substituting the abovementioned parameters into equations (1)–(3): $W_w = 2.41$ mm, $T = 12.04$ mm, and $D = 148.15$ mm. Then, keeping the period $T = 12.04$ mm unchanged, we alter the width of the LTS and move to the corresponding position in its respective period. However, there must be an upper limit $W_{w\max}$ and lower limit $W_{w\min}$ to the LTS width to ensure the effect of stereodisplay not to increase too sharply due to the mighty wide LTS and not to cause serious loss of stereoimage brightness due to excessive narrow LTS. The experiment verifies that the vernier fringe can be effectively weakened and the

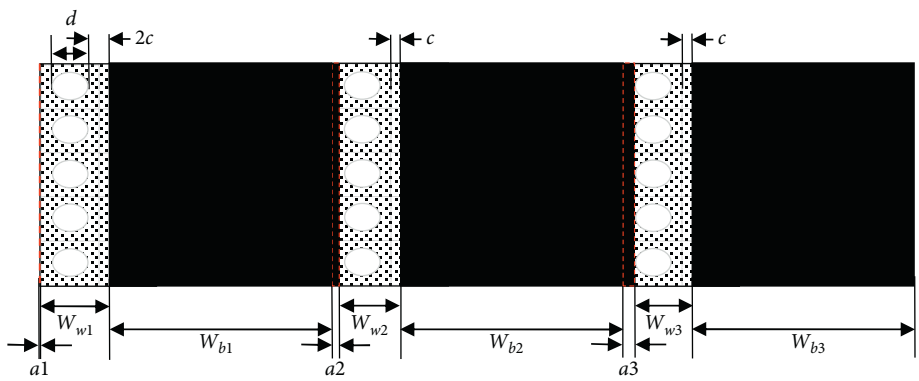

Figure 2: Structure of the malposed parallax barrier with discrepant width of slits, $W_{w1} = 3.0$ mm, $W_{w2} = 2.7$ mm, and $W_{w3} = 2.41$ mm, respectively.

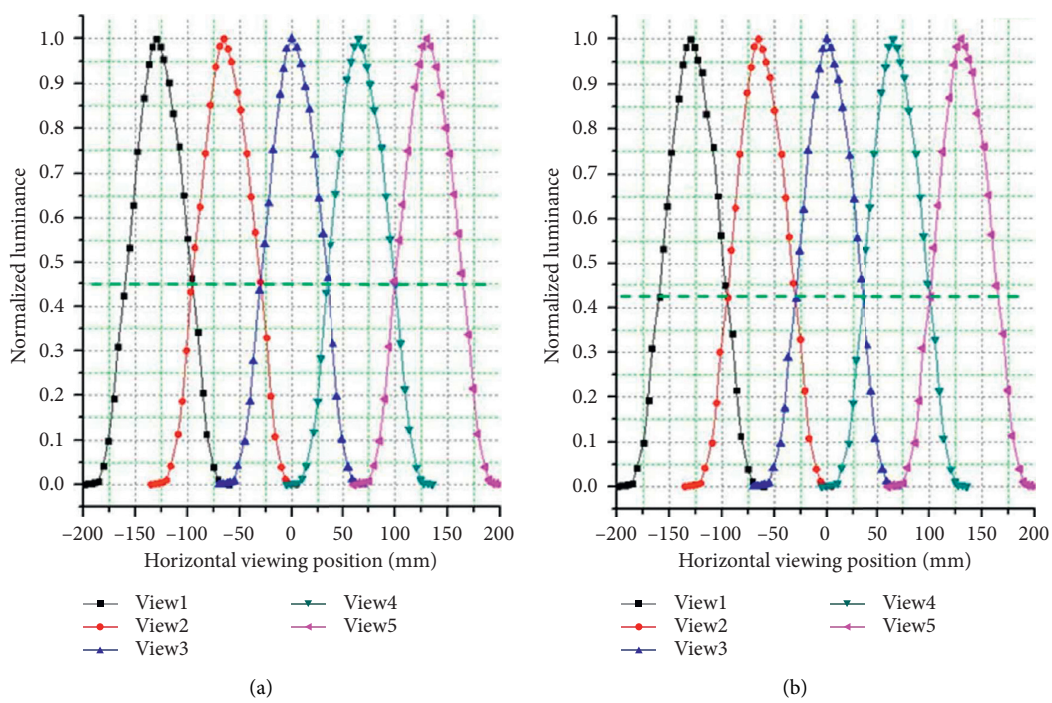

Figure 3: Normalized brightness distribution curves of naked-eye 3D displays based on the parallax barrier at the optimum 3D view distance. (a) Using the proposed parallax barrier; (b) using the conventional vertical parallax barrier.

crosstalk has little effect when the width of the LTS is equal to the sum of the pixel spacing p and the half width c of the BM. The crosstalk can increase dramatically if the width of the LTS is further expanded. Besides, the width of the LTS equaling to the original width, $W_w = 2.41$ mm, is the minimal width which we can implement as the brightness of the stereoimage can be radically disrupted by the deteriorative vernier fringe when smaller width is applied. Thus, the upper limit of LTS width is $W_{w\max} = p + c = 3$ mm, and the lower limit is $W_{w\min} = W_w = 2.41$ mm.

During the experiment, the widths of the LTS in the first period T_1 and the second period T_2 are extended to $W_{w1} = p + c = 3c + d = 3.0$ mm and $W_{w2} = 2.7$ mm, shifting in the right direction $a_1 = 0$ mm and $a_2 = 0.3$ mm, respectively, whereas the width of the LTS in the third period T3 remains the same, $W_{w3} = W_w = 2.41$ mm, shifting to the right $a_3 = 0.59$ mm. Finally, the experimental process is replicated over every three periods to complete the proposed designing means of the misplaced parallax barrier with nonuniform width of LTS.

4. Simulation and Experimental Results

4.1. Simulation Results and the Analysis. We use ASAP software to simulate the brightness distribution of every view point for the naked-eye 3D display. Figure 3 illustrates the normalized luminance distribution in the horizontal direction at the optimum viewing distance. Figure 3(a) shows the simulation performance of the proposed misplaced parallax barrier with nonuniform LTS width, and Figure 3(b) demonstrates the corresponding performance of the conventional vertical parallax barrier.

Table 1: Specifications and parameters of the two prototypes, prototype 1 with a misplaced parallax barrier with nonuniform width of the LTS and prototype 2 with a traditional vertical parallax barrier.

Parameters	Prototype1	Prototype2 (mm)
Size	640 × 320 mm	
2D resolution	256 × 128	
Pixel spacing p	2.5 mm	
Number of viewing points K	5	
Optimal viewing distance S	4 m	
3D resolution	51 × 128	
Period	12.04 mm	
	3.0 mm	2.41
LTS's width	2.7 mm	2.41
	2.41 mm	2.41

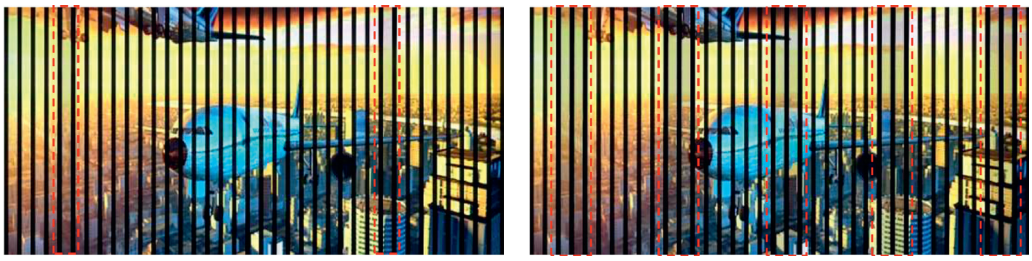

(a) (b)

Figure 4: Comparison of experimental results. (a) Diazone of prototype 1: light, thin, and sparse; (b) diazone of prototype 2: prominent, wide, and dense.

More specifically, the horizontal axis of Figure 3 represents the horizontal viewing position and the viewing position is directly opposite the center of the naked-eye 3D display when the value on horizontal axis reaches zero (0 mm). We can qualitatively measure the severity of crosstalk by the amount of the overlapped region of the normalized luminance distribution at each view point. The smaller the overlapped area is, the less the crosstalk is introduced and, thereby, the better the performance of the naked-eye 3D displayer is. Comparing Figure 3(a) with Figure 3(b), the overlapped region of the brightness curves of each view point in Figure 3(a) is slightly more than that in Figure 3(b), enhancing the crosstalk merely a little bit. But, it influences little on the visual zone and viewing effect.

4.2. Experimental Results and Analysis. To conduct the comparative experiments, a naked-eye 3D displaying prototype 1 with a misplaced parallax barrier with nonuniform width of the LTS and a naked-eye 3D display prototype 2 with a traditional vertical parallax barrier were produced. The dominant parameters are shown in Table 1. Also, Figure 4 demonstrates the image details of vernier fringe when two prototypes display the stereoimage, while Figure 4(a) implies applying the prototype 1 with a misplaced parallax barrier with nonuniform width of the LTS, whereas we adopt the traditional prototype 2 for Figure 4(b). The consequences show that the diazone of vernier fringe is light, thin, and sparse, giving rise to the desired viewing effect for prototype 1, but in Figure 4(b), it is prominent, wide, and dense.

Therefore, the experiment results verify that the proposed structure can obviously reduce the vernier fringe of the parallax barrier naked-eye 3D display and improve the stereoimaging effect. By appropriately increasing the width of the LTS of the parallax barrier and moving it to the corresponding position in its period, the difference between the periodic structure of the parallax barrier and the pixel periodic structure of the LED screen can be enlarged. Hence, the correlation between the splitter elements and the displaying screen can be lessened. Such a design method reduces the contrast ratio of the BM at the junction of adjacent viewpoints, thus promoting the brightness of the diazone in vernier fringe and making it sparse.

5. Conclusions

In this paper, in order to effectively reduce the vernier fringe of the parallax barrier naked-eye 3D display, a new designed parallax barrier is proposed, which is the misplaced parallax barrier with nonuniform width of the LTS. This parallax barrier can enhance the brightness of the diazone in vernier fringe and make it obviously fade, thin, and sparse. The simulation and experimental results prove that the proposed structure can effectively weaken vernier fringe at the condition that no obvious crosstalk of stereoimages is increased. Thus, the research has high practical value.

Abbreviations

LTS: Light translucent slit
BM: Black matrix
LBS: Light blocking slit.

Data Availability

All the data used to support the findings of this study are included within the article.

Conflicts of Interest

The authors declare no conflicts of interest.

Acknowledgments

This work was supported by the Sichuan Province Science and Technology Plan Project under Grant no. 2021YJ0094.

References

[1] Q. Kai-huai and J.-l. Luo, "Techniques for autostereoscopic display and its development," *Journal of Image and Graphics*, vol. 14, no. 10, pp. 1934–1941, 2009.
[2] Y. Jia-chen, H. Chun-ping, and L. Jian-jun, "Stereo image coding algorithm based on mesh," *Journal of Optoelectronics·Laser*, vol. 21, no. 1, pp. 136–139, 2010.
[3] T. Okosi, *Three-Dimensional Imaging Techniques*, Academic Press, Cambridge, MA, USA, 1976.
[4] N. A. Dodgson, "Autostereoscopic 3D displays," *Computer*, vol. 38, no. 8, pp. 31–36, 2005.
[5] Z. Ji-gui, X. Ting, and B. Wu, "Study on the coding design and point matching of LCD coded raster," *Journal of Optoelectronics·Laser*, vol. 16, no. 2, pp. 164–166, 2005.
[6] W. Mphepo, Y.-P. Huang, and H.-P. D. Shieh, "Enhancing the brightness of parallax barrier based 3D flat panel mobile displays without compromising power consumption," *Journal of Display Technology*, vol. 6, no. 2, pp. 60–64, 2010.
[7] J. Geng, "Three-dimensional display technologies," *Advances in Optics and Photonics*, vol. 5, no. 4, pp. 456–535, 2013.
[8] H. Yamamoto, H. Nishimura, T. Abe, and Y. Hayasaki, "Large stereoscopic LED display by use of parallax barrier of aperture grille type (Invited Paper)," *Chinese Optics Letters*, vol. 12, no. 6, pp. 060006–060010, 2014.
[9] S. Ping, A. Peng-li, and G.-f. Jin, "Demonstration of an autostereoscopic three-dimensional light-emitting diode display using diffractive optical elements sheet," *Journal of Display Technology*, vol. 11, no. 11, pp. 953–958, 2015.
[10] S. Ping, A. Peng-li, and C. Liang-cai, "Characteristics of the autostereoscopic three-dimensional LED display based on diffractive optical elements sheet," *SPIEL*, vol. 10022, p. 100221Y, 2016.
[11] A. N. Shu, S. U. Ping, M. A. Jian-she, and H. E. Ze-hao, "Analysis of stereo depth for 3D LED autostereoscopic displays based on the physical limitation," *SPIEL*, vol. 10378, p. 103780V, 2017.
[12] Y.-z. Huang, M. Rafiq Swash, and A. Sadka, "Innovative 3D pixel mapping method for LED holoscopic 3D display," *SPIN*, pp. 330–333, 2017.
[13] Z. Ren-liang, Z. Wu-xiang, and Q.-h. Wang, "Research on stereo viewing zone in autostereoscopic display based on parallax barrier," *Acta Photonica Sinica*, vol. 37, no. 5, pp. 960–963, 2008.
[14] H. Yamamoto, T. Kimura, S. Matsumoto, and S. Suyama, "Viewing-zone control of light-emitting diode panel for stereoscopic display and multiple viewing distances," *Journal of Display Technology*, vol. 6, no. 9, pp. 359–366, 2010.
[15] S. Xian-yu and L. Ji-tao, "Method for 3-D object recognition based on moire fringe," *Journal of Optoelectronics laser*, vol. 3, 2005.
[16] H.-x. Wang, S. Xian-yu, and L. Jing, "Method for 3D object recognition based on moiré fringe," *Journal of Optoelectronics·Laser*, vol. 16, no. 3, pp. 349–353, 2005.
[17] K. Ling-sheng, G. Jin, and T.-c. Wang, "Analysis of Moiré minimization in autostereoscopic parallax displays," *Optics Express*, vol. 21, no. 22, pp. 26068–26079, 2013.
[18] Y.-q. Wang, "Auto-stereoscopic display based on LCD," *Chinese Journal of Liquid Crystals and Displays*, vol. 18, no. 2, pp. 116–120, 2003.
[19] W. Pei-shun, Y. Jian-min, and G. Tai-liang, "Design of vertically staggered barrier for autostereoscopic display," *Journal of Optoelectronics·Laser*, vol. 22, no. 6, pp. 827–830, 2011.
[20] J. M. Yao, Q. Xin, and T. L. Guo, "Design of zigzag staggered barrier for autostereoscopic display," *Acta Photonica Sinica*, vol. 41, no. 10, pp. 1176–1179, 2012.
[21] X. Guo, H. Chun-ping, and S. Li-li, "Theoretical analysis of title angles based on autostereoscopic display with slanted barrier," *Laser Technology*, vol. 40, no. 3, pp. 388–391, 2016.
[22] Z. Xiang-Yao, Z. Xiong-Tu, and G. Tai-liang, "Crosstalk reduction in large-scale autostereoscopic 3D-LED display based on black-stripe occupation ratio[J]," *Optics Communications*, vol. 389, no. 15, pp. 159–164, 2017.
[23] L. S. Kong, C. Y. Liu, Y. Zhang, and G. Jin, "Progress on removing Moiré patterns in parallax autostereoscopic displays," *Chinese Journal of Liquid Crystals and Displays*, vol. 29, no. 3, pp. 441–449, 2014.
[24] Q.-h. Wang, *3D Display Technology and Devices*, Science Press, Beijing, China, 2011.

Hindawi
International Journal of Optics
Volume 2021, Article ID 2322858, 6 pages
https://doi.org/10.1155/2021/2322858

Research Article

Investigation of Light Parameters on Image Quality and Optical Coherence Tomography

Boka Fikadu,[1] Bulcha Bekele,[1] Leta Tesfaye Jule,[1,2] Anatol Degefa,[3] N. Nagaprasad,[4] and Krishnaraj Ramaswamy[4,5]

[1]*Department of Physics, College of Natural and Computational Science, Dambi Dollo University, Dembi Dolo, Ethiopia*
[2]*Centre for Excellence-Indigenous Knowlegde, Innovative Technology Transfer and Enterpreneurship, Dambi Dollo University, Dembi Dolo, Ethiopia*
[3]*Department of Mathematics, College of Natural and Computational Science, Dambi Dollo University, Dembi Dolo, Ethiopia*
[4]*Department of Mechanical Engineering, ULTRA College of Engineering and Technology, Madurai 625 107, Tamil Nadu, India*
[5]*Department of Mechanical Engineering, College of Engineering, Dambi Dollo University, Dembi Dolo, Ethiopia*

Correspondence should be addressed to Krishnaraj Ramaswamy; prof.dr.krishnaraj@dadu.edu.et

Received 9 July 2021; Accepted 21 October 2021; Published 26 November 2021

Academic Editor: Wuxiang Zhao

In this work, image quality and optical coherence tomography were studied. The results of the study show that there is a very significant difference between ultrasound and optical coherence tomography to produce an image with a different wave. To understand this, we studied the basic principle of optical coherence tomography in the Michelson interferometer using monochromatic and broadband sources. Time-domain and spectral-domain measurements, which exist at the detector level, are briefly described using a glass sample. The time-domain signal strength of the Michelson interferometer using a broadband source is a Gaussian envelope.

1. Introduction

Huang invented optical coherence tomography (OCT) in 1991, and it has since found various applications outside of ophthalmology. For example, OCT is also used to picture certain nontransparent tissues [1]. OCT (optical coherence tomography) system is an optical instrument that provides a cross-sectional image of the biological tissue with an axial resolution of less than 10 microns utilizing light waves [2]. Furthermore, optical coherence tomography (OCT) is a technique that is currently in use in medicine and biology and is capable of creating high-resolution and cross-sectional images of biological tissues [3]. Included in this category are both transparent tissues, including the eyes, and heavily scattering tissues, such as the skin [4]. OCT has very similar applications to ultrasound imaging, but instead of using time-of-flight measurements, OCT utilizes the interference nature of light waves to produce coherence gating [5]. One of the most important components of OCT is that there is no ionizing radiation, and it is not necessary to prepare a sample [6]. Additionally, OCT is comparatively safe when compared with another technique that uses X-rays because it uses light sources without ionizing radiation being involved. Furthermore, with the advantage of being a noninvasive (in vivo) technique, OCT systems show great potential in the future of medical diagnostics. Today, scanning of retinas to reveal defects in the underlying tissue is the area of most success for OCT, and standalone units are being sold commercially [4–6]. The OCT technique is limited to an imaging size of up to 1 mm below the surface of biological tissues [7]. OCT is specifically good at scanning the retina [8]. Because the retina is readily available to external light, optical coherence tomography (OCT) is particularly useful for diagnosing abnormalities [9]. The light enters the eyes, and the retina converts it into electric signals and passes them to the brain for the formation or reconstruction images [1, 2]. The major component of the retina is the optics disk, macula, and blood vessels. Using OCT, it is

easy to see ten different tissue layers inside the retina [2, 5, 8]. Only about a decade ago, the first reports of OCT use in medicine were published in peer-reviewed journals [1, 5, 7]. Although its roots can be traced back to early research on white light interferometry, the discovery of optical coherence domain reflectometry (OCDR), a one-dimensional optical detection technique, is credited with giving rise to the technology [10]. It was initially designed for the purpose of detecting flaws in defective optical fibres and optical network components; nevertheless, its capacity to probe the eye as well as other biological tissues was quickly realized [11]. OCT is a modern variant of a Michelson interferometer, which worked by removing one side of the reference mirror and replacing it with a sample glass to determine the image of the tissue using monochromatic sources and broadband sources [12]. OCT is a type of optical coherence tomography that operates in both the time domain and the spectral domain [13]. For evaluating depth study in time-domain optical coherence tomography, the reference mirror must be moved; however, spectral-domain optical coherence tomography is a Fourier transform analysis performed without adjusting the mirror [2]. In this article, we explain the application of modern optical instruments, specifically for measurements using a Michelson interferometer. Additionally, we simulate the signal Fourier transforms of the materials and compare them with the results of an image of the sample. The primary goal of this study is to figure out the images of OCT using low coherence interference. As a result, time-domain and spectral-domain optical coherence tomography can be determined in broadband sources.

2. Principle of Optical Coherence Tomography

OCT has special characteristics, like it is noninvasive and is nondestructive. OCT is used to identify very small structures, and it is used to look under the skin. It can also be used to give information by producing a 3-dimensional image [14].

2.1. Interferences. Young's double-slit experiment is the famous demonstration of optical interference and describes that the light from a single source radiating through two slits (or hole) can interfere with projection of an alternating fringe pattern of bright and dark bands on a screen [1, 6, 9]. These bright and dark fringes occur because of the constructive and destructive interferences of light, respectively. Depending on this bright and dark pattern, the light waves from the two slits are in phase and we add them together up to the resultant maximum amplitude called constructive interference, or when the light waves from the two slits are out of phase, we subtract up to the resultant minimum amplitude called destructive interference. That these two (constructive and destructive interferences) exist are based on the optical path length difference (OPD) between the slits and the same location on the screen [11, 13, 15].

2.2. Michelson Interferometer. The principle of optical coherence tomography originates with the Michelson interferometer, which was invented by A. A. Michelson in 1881. OCT is analogous to ultrasound, as they measure the back reflection intensity of infrared light beams instead of using the echoes of sound. Because of the rapid speed at which light propagates, it is impossible to quantify the back reflection intensity of OCT using electrical instruments [16]. Figure 1 shows a Michelson interferometer, which consists of two reflective mirrors, mirror 1 and mirror 2. Light is emitted from the light source, which hits the beam splitter, with half of the light going along path L_1 and reflected back to the beam splitter while the other half goes along optical path L_2 and is reflected back to the beam splitter [17]. These two light waves will interact with each other and be detected with the photodetector. Depending on the length difference between optical paths L_1 and L_2, either constructive or destructive interference will occur. Since both return beams will go through the beam splitter (a half-silvered mirror) again, they lose 50% of their intensity. In some more complicated setups, a polarizing beam splitter (half-silvered mirror) and wave retarders can be used to avoid this power loss.

OCT is a modern instrument that is used to produce an image, and image technology projects a light beam (820 nm) near the infrared wavelength. Figure 2 shows the setup of OCT, similar to the Michelson interferometer setup. In this setup, only one reference mirror (a movable mirror) is used, and another, the standard mirror, has been changed with a sample of glass. The spectrum from the source of light is separated into different beams using the beam splitter. The probe beam enters the object, and the reference beam approaches the standard mirror at a predetermined distance from the reference mirror. Light reflected from different layers of the specimen is measured and compared to the light reflected from the reference mirror, which measures the echo duration or delay of the light reflected from the reference mirror. When light reflected from both the sample and reference mirrors arrives at the same time, a positive interference is formed. The interferometer integrates numerous data points over a depth of 2 mm to generate a tomogram of retinal architecture using the information from the data points [18].

From Figure 2, we have an incidence electric field, coefficient of reflection, and transmission of a glass sample. Let us derive the equation of the incident electric field of the sample and calculate the intensity at the detector. Consider the incident light as a plane wave, where the net field at the photodetector includes the electric field coming from L_1 of the interferometer $E_0(t,\tau) = \mathrm{E}e^{i\omega(t+\tau)}$ and the electric field coming from L_2 as $E_0(t) = \mathrm{E}e^{i\omega t}$.

3. Results and Discussion

In the previous section, we have discussed the principles of OCT and the way OCT can be used like a Michelson interferometer. However, in this case, we review the analysis, discussion, and simulation of this project. The intensity of the Michelson interferometer was simulated, and the signal intensity of the Michelson interferometer in monochromatic and broadband sources was simulated. The signal intensity of OCT in a Michelson interferometer, when one reference

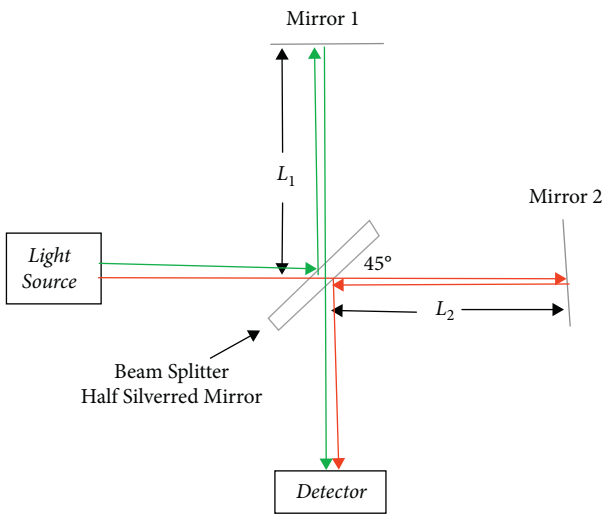

Figure 1: Schematic of the Michelson interferometer.

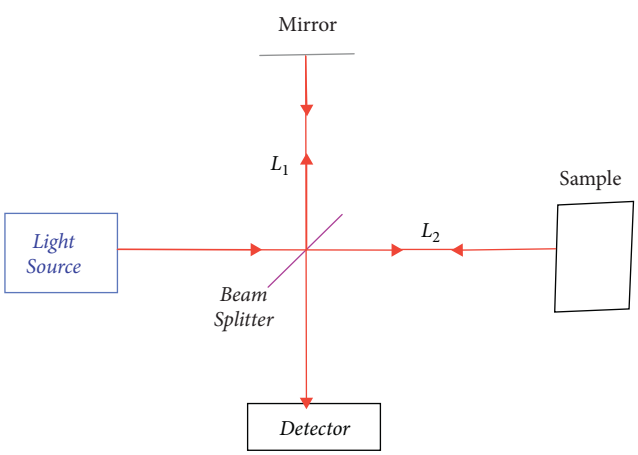

Figure 2: Schematic of OCT in Michelson interferometer.

mirror is replaced by a glass sample which has a refractive index of 1.5 and thickness of 1 mm, using monochromatic and broadband sources was simulated [19].

3.1. Simulations of Signal from the Michelson Interferometer. We simulated the intensity with the function of time at a detector. In this simulation, we used the central wavelength (λ_0) as 1 μm and the spectral width ($\Delta\lambda$) as 100 nm for the light source and the velocity and position of the mirror as constant. The intensity which exists at the detector in the Michelson interferometer, with an incident wave as a function of time, is shown in Figure 3.

When the time was zero, the maximum intensity existed and the entire incident light did not occur. We simulated the signal intensity of a monochromatic source, as shown in Figure 4. The signal intensity of the monochromatic source was simulated, where the horizontal axis shows the time difference between the movable mirror and the fixed mirror. In this simulation, we used the central wavelength (λ_0) as 1 μm and the spectral width ($\Delta\lambda$) as 100 nm for the light source and the velocity and orientation of the mirror as

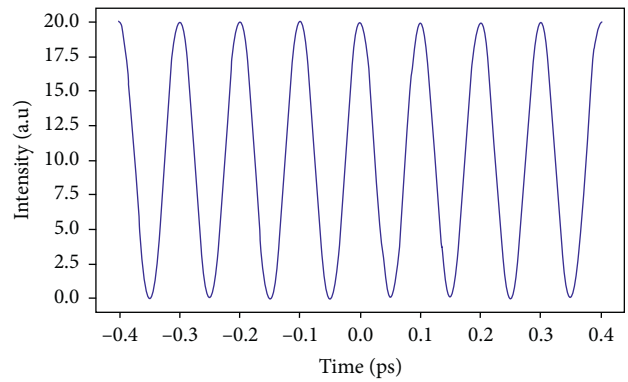

Figure 3: Intensity of the Michelson interferometer.

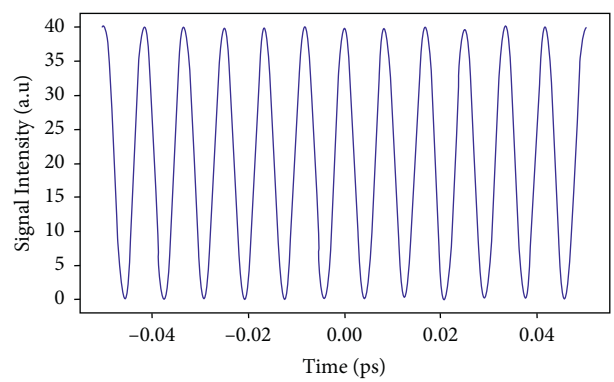

Figure 4: Signal intensity of a monochromatic source.

constant. Its greatest possible amplitude refers to constructive interference as well as the minimum amplitude refers to destructive interference. When the time difference is zero, the reflectance is maximum and this is called constructive interference [20].

We simulated the signal intensity of the Michelson interferometer using a broadband coherent source, as shown in Figure 5. This simulation of signal intensity has a Gaussian envelope [21]. In this case, we have some amount of continuous broadband sources, and we used the central wavelength (λ_0) as 1 μm and the spectral width ($\Delta\lambda$) as 100 nm for the light source, where velocity and position of the mirror were constant. For this signal intensity, the movable mirror is of 1.5 ps. The horizontal axis shows the time difference of the movable mirror.

From this Michelson interferometer, the signal intensity of light with a Gaussian spectrum as time is either increased or decreased; the output signal intensity started to oscillate. In this case, when we move the reference mirror by half-length, we get a different fringe pattern at each time.

3.2. Simulations of OCT in a Michelson Interferometer. We simulated signal intensity at the detector using a monochromatic source. In this case, one of the reference mirrors is replaced by a sample of glass. This sample glass has a thickness of 1 mm and a refractive index of 1.5. From the setup, we measure the reflection and transmission of the

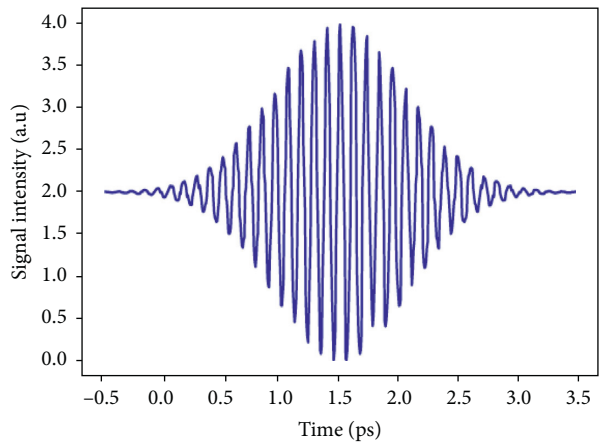

Figure 5: Signal intensity of the broadband coherent source.

sample of glass as a function of time. First, we calculated the electric field, where the Fresnel equations are of perpendicular incidence. That is, there would be a reflection at the first surface and off the second surface and then also multiple reflections, which are called Fabry–Perot reflections [22]. The number of reflections we took into account would depend on the duration of the scan. The signal intensity of OCT in a Michelson interferometer using a monochromatic source with a long coherence length like a variable of time is shown in Figure 6. The maximum amplitude is for constructive interference, and the minimum amplitude is for destructive interference. When the time difference is zero, the reflectance is maximum and it is called constructive interference. This means the monochromatic signal intensity fringes are in phase only for zero time [23–28].

Figure 7 shows the signal intensity of OCT in a Michelson interferometer using a broadband source. The central wavelength of (λ_0) 1 μm and the spectral width ($\Delta\lambda$) of 100 nm for the light source were simulated. Signal intensity for the optical path length of the sample glass and the movable mirror was matched to the narrow coherence length as the light source used low coherence (broadband sources). The movable mirror started to scan when the optical path length of the reflections from within the sample glass matched each other. The incoming light source was split into two by the beam splitter. This means that when the incoming light passed through two different path lengths L_1 and L_2, then it was collinearly superimposed at the beam splitter, the two pulses reflected in each arm of the interferometer, and one of the arm's lengths is increased, the distance causing a delay on recombining. The fundamental wavelength was rejected when the sample glass is detected by a photodetector as a function of the width of the time autocorrelation=2nd/c between the pulses. Since the refractive index and thickness of the glass are 1.5 and 1 mm, respectively, based on these values, we calculated the width of time = 10 picoseconds (10 ps) and frequency of 1×10^{12} Hertz (1 THz). The time delay at the detector using the width of the time pulse was calculated, where the central wavelength was ($\lambda 0$) 1 μm and the spectral width ($\Delta\lambda$) was 100 nm, and the result was 3.3 ps.

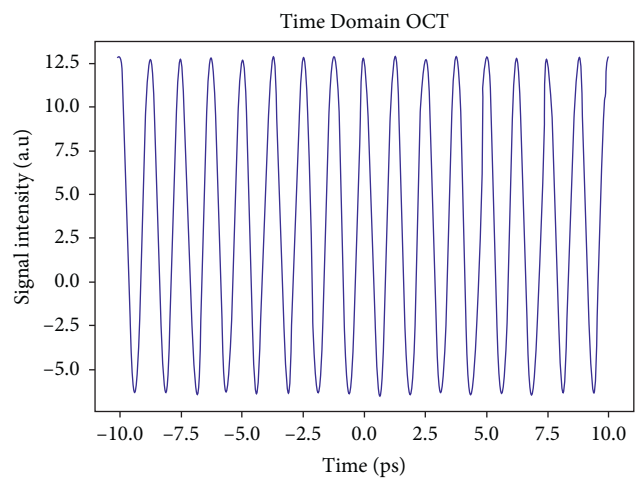

Figure 6: Signal intensity of monochromatic sources.

In this time-domain, OCT, three of these pulses have the same approximate width but different heights. In the simplest method, we measured the shape of the pulse as changing with the distance of the time depth of the reference mirror and then we could see the signal intensity of our sample glass. The time delay of the movable mirror in this signal intensity of OCT was twice the time delay of the movable mirror in the signal intensity of Michelson interferometry. Since we have the values of the refractive index of glass, 1.5, and the thickness of the glass, 1 mm, we easily simulated the electric field. Additionally, we have some constant values, such as the reflection coefficient and transmission coefficient, as well as the values of the angular frequency (ω) and tau (τ), also being constant. After we simulated the electric field, we found the Fourier transform of this electric field. This Fourier transform of the electric field is the spectral domain of the OCT. We measured this spectral domain of the OCT without moving the mirror, and we only focused the Fourier transform of an electric field of a sample glass [29–34].

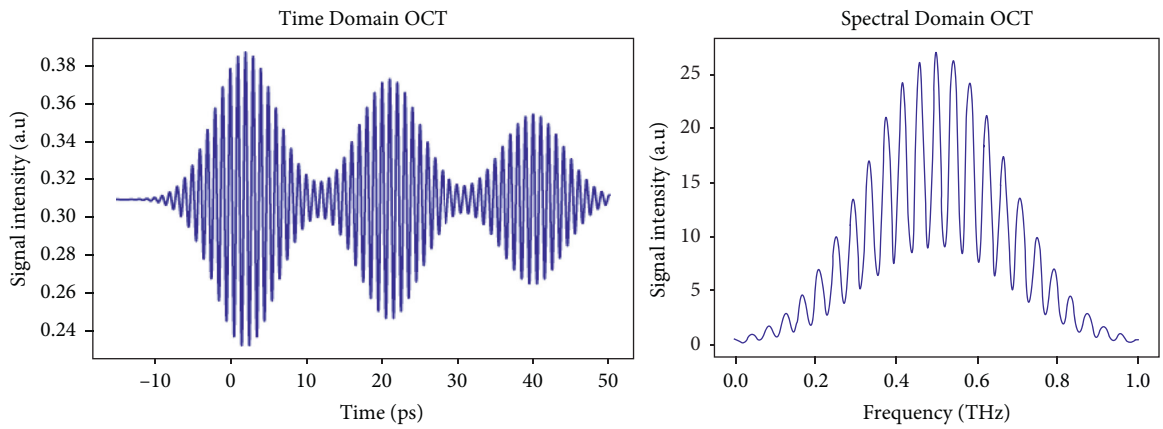

Figure 7: Signal intensity of a broadband coherent source.

4. Conclusions

In our work, the application of nanotechnology in integrating OCT with the Michelson interferometer was realized. It is evident that the most important part of an OCT is the time domain and spectral domain. The time domain is based on a moving mirror, but the spectral domain is not based on this moving mirror; it is based on the Fourier transform of an electric field. OCT has many applications in hospitals and industries, but it is mostly used on transparent materials or tissues. OCT is a modern technique that is used to create two- or three-dimensional images without involving any ionizing radiation. The way we measured the signal intensity at the detector in OCT is the same method as for the Michelson interferometer. However, we replaced the fixed mirror with a sample of glass. We then talked about the time domain and spectral domain using a broadband source and a sample glass instead of a reference mirror on one side. We have shown from our results and simulation that the time domain generates ultrafast laser pulses in the range of picoseconds. Some of the characteristics of the pulses were computed, such as their ultrafast laser pulse duration (ps), repetition time, and intensity signal. As our results show, the numerical simulation of using the auto-correlation function to determine the temporal size of ultrafast pulse durations took 10 ps in the time domain of OCT integrated nanotechnology inference was concluded, indicating that the time domain is one of the best techniques for generating ultrafast laser pulses.

Data Availability

The data used to support the findings of this study are included within the article.

Conflicts of Interest

The authors declare that there are no conflicts of interest.

References

[1] M. Tomaniak, D. Ochijewicz, Ł. Kołtowski et al., "OCT-derived plaque morphology and FFR-determined hemodynamic relevance in intermediate coronary stenoses," *Journal of Clinical Medicine*, vol. 10, no. 11, p. 2379, 2021.

[2] E. A. Rank, R. Sentosa, D. J. Harper et al., "Toward optical coherence tomography on a chip: in vivo three-dimensional human retinal imaging using photonic integrated circuit-based arrayed waveguide gratings," *Light: Science & Applications*, vol. 10, pp. 1–15, 2021.

[3] Y. Hamanaka, Y. Sotomi, T. Kobayashi et al., "Comparable neointimal healing in patients with stable coronary lesions and acute coronary syndrome: 3-month optical coherence tomography analysis," *The International Journal of Cardiovascular Imaging*, vol. 15, pp. 1–11, 2021.

[4] O. Mc Grath, M. W. Sarfraz, A. Gupta, Y. Yang, and T. Aslam, "Clinical utility of artificial intelligence algorithms to enhance wide-field optical coherence tomography angiography images," *Journal of Imaging*, vol. 7, no. 32, 2021.

[5] J. Zhang, F. Y. Tang, C. Cheung, X. Chen, and H. Chen, "Different effect of media opacity on automated and manual measurement of foveal avascular zone of optical coherence tomography angiographies," *British Journal of Ophthalmology*, vol. 105, pp. 812–818, 2021.

[6] I. M. Fang, H. Y. Hsu, W. L. Chiang, Y. L. Shih, and C. L. Han, "Correlation between visual acuity and optical coherence tomography angiography parameters in unilateral idiopathic epiretinal membrane," *Journal of Clinical Medicine*, vol. 10, pp. 26–38, 2021.

[7] M. Dembski, A. Nowinska, K. Ulfik-Dembska, and E. Wylęgała, "Swept source optical coherence tomography analysis of the selected eye's anterior segment parameters," *Journal of Clinical Medicine*, vol. 10, no. 1094, 2021.

[8] R. Oh, J. Y. Oh, H. J. Choi, M. K. Kim, and C. H. Yoon, "Comparison of ocular biometric measurements in patients with cataract using three swept-source optical coherence tomography devices," *BMC Ophthalmology*, vol. 21, pp. 1–7, 2021.

[9] Z. Lin, X. Pan, K. Mao et al., "Quantitative evaluation of retinal and choroidal changes in fabry disease using optical coherence tomography angiography," *Lasers in Medical Science*, 2021.

[10] M. G. Altınel, B. Acikalin, H. Gunes, and G. Demir, "Optical coherence tomography parameters as predictors of treatment response to a 577-nm subthreshold micropulse laser in chronic central serous chorioretinopathy," *Lasers in Medical Science*, vol. 36, 2021.

[11] A. Miraftabi, S. Jafari, N. Nilforushan, P. Abdolalizadeh, and R. Rakhshan, "Effect of trabeculectomy on optic nerve head

and macular vessel density: an optical coherence tomography angiography study," *International Ophthalmology*, vol. 41, 2021.

[12] J. W. Lee, S. Y. Park, P. S. Kim, I. H. Cho, and H. D. Kim, "Correlations among metamorphopsia test scores, optical coherence tomography findings and multifocal electroretinogram responses in epiretinal membrane patients," *Documenta Ophthalmologica*, vol. 142, no. 3, pp. 293–304, 2021.

[13] S. Gao, Y. Li, D. Bissig et al., "Functional regulation of an outer retina hyporeflective band on optical coherence tomography images," *Scientific Reports*, vol. 11, pp. 1–13, 2021.

[14] X. Wang, Q. Wei, X. Wu et al., "The vessel density of the superficial retinal capillary plexus as a new biomarker in cerebral small vessel disease: an optical coherence tomography angiography study," *Neurological Sciences*, vol. 42, 2021.

[15] X. Liu, X. Zhang, J. Ma, and X. Shi, "Integrated system for combined optical coherence tomography-raman spectroscopy of neocaridina denticulate sinensis," *Journal of Ocean University of China*, vol. 20, no. 1, pp. 94–100, 2021.

[16] S. Cheng, Y. Yu, Y. You et al., "Retinal nerve fiber layer thickness measured by optical coherence tomography predicts visual recovery after orbital decompression for dysthyroid optic neuropathy," *International Ophthalmology*, vol. 41, 2021.

[17] M. Mohan, S. K. Maurya, K. Kumar, and R. Poddar, "In vitro imaging of animal tissue with upconversion nanoparticles (UCNPs) as a molecular probing agent using swept source optical coherence tomography (SSOCT)," *Journal of Medical and Biological Engineering*, vol. 40, no. 2, pp. 251–263, 2020.

[18] I. W. Schie, F. Placzek, F. Knorr et al., "Morpho-molecular signal correlation between optical coherence tomography and raman spectroscopy for superior image interpretation and clinical diagnosis," *Scientific Reports*, vol. 11, pp. 1–14, 2021.

[19] J. Yi, W. Liu, S. Chen et al., "Visible light optical coherence tomography measures retinal oxygen metabolic response to systemic oxygenation," *Light: Science & Applications*, vol. 4, no. 9, p. e334, 2015.

[20] T. Zhang, S. Xie, Y. Liu, C. Xue, and W. Zhang, "Effect of amblyopia treatment on macular microvasculature in children with anisometropic amblyopia using optical coherence tomographic angiography," *Scientific Reports*, vol. 11, pp. 1–7, 2021.

[21] M. F. Alakus, M. Caglayan, N. Ekin et al., "Investigation of corneal topographic and densitometric properties of Wilson's disease patients with or without a Kayser-Fleischer ring," *Eye and Vision*, vol. 8, pp. 1–8, 2021.

[22] M. Nassisi, C. Lavia, S. Mohand-Said et al., "Near-infrared fundus autofluorescence alterations correlate with swept-source optical coherence tomography angiography findings in patients with retinitis pigmentosa," *Scientific Reports*, vol. 11, pp. 1–12, 2021.

[23] L. Barbano, L. Ziccardi, and V. Parisi, "Correlations between visual morphological, electrophysiological, and acuity changes in chronic non-arteritic ischemic optic neuropathy," *Graefe's Archive for Clinical and Experimental Ophthalmology*, vol. 259, no. 5, pp. 1297–1308, 2021.

[24] C. Zhuo, B. Xiao, C. Chen et al., "Abberant inverted U-shaped brain pattern and trait-related retinal impairment in schizophrenia patients with combined auditory and visual hallucinations: a pilot study," *Brain imaging and behavior*, vol. 15, no. 2, pp. 738–747, 2021.

[25] S. Abel, J. L. Tesfaye, N. Nagaprasad, R. Shanmugam, L. P. Dwarampudi, and R. Krishnaraj, "Synthesis and characterization of zinc oxide nanoparticles using moringa leaf extract," *Journal of Nanomaterials*, vol. 2021, Article ID 4525770, 2021.

[26] D. C. Lekha, R. Shanmugam, K. Madhuri et al., "Review on silver nanoparticle synthesis method, antibacterial activity, drug delivery vehicles, and toxicity pathways: recent advances and future aspects," *Journal of Nanomaterials*, vol. 2021, Article ID 4401829, 2021.

[27] A. Degefa, B. Bulcha, L. T. Jule et al., "Green synthesis, characterization of zinc oxide nanoparticles and examination of properties for dye sensitive solar cells using various vegetable extracts," *Journal of Nanomaterials*, vol. 2021, Article ID 3941923, 2021.

[28] S. Abel, J. L. Tesfaye, B. Fikadu et al., "Preparation of nano sheets from titanium dioxide nanoparticles synthesized by chemical bath deposition techniques and applications in desalination and waste water treatment," *Journal of Nanomaterials*, vol. 2021, Article ID 3039761, 2021.

[29] B. Bulcha, J. L. Jule, A. Degefa et al., "Synthesis of zinc oxide nanoparticles by hydrothermal methods and spectroscopic investigation of ultraviolet radiation protective properties," *Journal of Nanomaterials*, vol. 2021, Article ID 8617290, 2021.

[30] B. Bulcha, A. Degefa, F. Tesgera et al., "Green versus chemical precipitation methods of preparing zinc oxide nanoparticles and investigation of antimicrobial properties," *Journal of Nanomaterials*, vol. 2021, Article ID 9210817, 2021.

[31] S. Abel, J. L. Tesfaye, R. Shanmugam et al., "Green synthesis and characterizations of zinc oxide (ZnO) nanoparticles using aqueous leaf extracts of coffee (coffea arabica) and its application in environmental toxicity reduction," *Journal of Nanomaterials*, vol. 2021, Article ID 3413350, 2021.

[32] L. Tesfaye Jule, K. Ramaswamy, B. Bekele, A. Saka, and N. Nagaprasad, "Experimental investigation on the impacts of annealing temperatures on titanium dioxide nanoparticles structure, size and optical properties synthesized through sol-gel methods," *Materials Today: Proceedings*, vol. 45, pp. 5752–5758, 2021.

[33] L. T. Jule, R. Krishnaraj, N. Nagaprasad, B. Stalin, V. Vignesh, and T. Amuthan, "Evaluate the structural and thermal analysisof solid and cross drilled rotor by using finite element analysis," *Materials Today: Proceedings*, vol. 47, 2021.

[34] T. Amuthan, N. Nagaprasad, R. Krishnaraj, V. Narasimharaj, B. Stalin, and V. Vignesh, "Experimental study of mechanical properties of AA6061 and AA7075 alloy joints using friction stir welding," *Materials Today: Proceedings*, vol. 46, 2021.

Hindawi
International Journal of Optics
Volume 2021, Article ID 8315101, 15 pages
https://doi.org/10.1155/2021/8315101

Research Article

Gamma Precorrection and Phase Error Compensation Methods Based on Three-Frequency with Three-Phase Shift

Wei Feng, Shaojing Tang, Shinan Xu, Tong Qu, and Daxing Zhao

Hubei Key Laboratory of Modern Manufacturing Quality Engineering, School of Mechanical Engineering, Hubei University of Technology, Wuhan 430068, China

Correspondence should be addressed to Wei Feng; david2018@hbut.edu.cn

Received 14 August 2021; Revised 8 September 2021; Accepted 9 September 2021; Published 21 September 2021

Academic Editor: Wei Liu

Digital fringe projection measurement technology has been widely used in computer vision and optical three-dimensional (3D) measurement. Considering the phase error caused by the gamma distortion and nonlinear error, the active gamma precorrection and phase error compensation methods based on the three-frequency with three-phase shifts are designed to reversely solve the initial phase and accurately compensate phase error. On the one hand, the gamma coefficient of the measurement system depends on precoding two groups of fringe sequences with different gamma coefficients to calculate the corresponded proportional coefficient of harmonic component. On the other hand, the phase error compensation method is designed to compensate the phase error and improve the accuracy and speed of phase calculation after gamma correction. Experiments show that the proposed precalibration gamma coefficient method can effectively reduce the sinusoidal error in nearly 80 percent which only needs fewer fringe patterns. Compared with the traditional three-frequency with four-phase shift method, the proposed method not only has higher phase accuracy and better noise resistance but also has good robustness and flexibility, which is not limited to the gamma distortion model.

1. Introduction

Digital fringe projection measurement technology has been widely used in computer vision and optical three-dimensional (3D) measurement because of the advantages in their noncontact operation and full-field inspection [1]. A series of preencoded sinusoidal fringes are projected onto the measured surface, and the sinusoidal fringes are modulated by the height distribution of the measured surface, also known as the deformed fringe; then, the phase method based on the multifrequency heterodyne is used to demodulate and calculate the phase distribution to obtain the 3D information of measured surface. This technology makes the structured light system more adaptive to operate. However, the brightness transfer function between the camera and the projector is not linear during the measurement process, and its gray function is usually nonlinear. Then, the nonlinear response of the input signal will become the large error source, which usually refers to the nonlinear gamma effect of the projection device. Gamma distortion will directly lead to the high harmonic component in the deformed fringes, which will affect the quality of the phase solution and bring measurement error to the 3D information. More digital fringe patterns may reduce some high-order harmonic components and improve the measurement accuracy, but the more the projected fringe patterns, the slower the measurement speed, which is not desirable for high-speed measurement. Therefore, it is of great significance to correct the nonlinear gamma distortion and compensate phase error by projecting less fringe patterns and simultaneously maintaining the phase quality.

At present, many scholars have carried out a lot of related research studies on the nonlinear correction and phase error compensation [2–8]. In general, the gamma correction method needs to calibrate the light intensity transfer function between the projector and the camera to correct the encoded fringe patterns which will be projected onto the measured surface. For example, Guo et al. [2] had estimated

the gamma coefficient and corrected the phase by analyzing the cumulative distribution characteristics of the sinusoidal function, but this method assumed that the fullfiled gamma distortion coefficient of the fringe pattern must be the same constant. The discrete Fourier transform was used, and only two fringe patterns were needed to calibrate the gamma coefficient, but additional factors in many spaces would bring calibration gamma error [3]. On the contrary, the phase error compensation method had collected the sinusoidal fringe which had been modulated by the measured surface, and then, the gamma error model was established to compensate the phase error. Huang et al. [4] had proposed double three-step phase shifts' technique to reduce the influence of gamma effect, but the optimization algorithm needed high-computational complexity and more phase shifts' fringe patterns. Moreover, a method based on the statistical law with look-up-table (LUT) was put forward, but it needed to precalibrate the error distribution to construct the LUT or estimate the error coefficient [5]. In addition, the defocused method no longer projected sinusoidal fringe patterns but needed binary fringe patterns in the defocused mode of the projector. Li et al. [6] had introduced the defocus factor of the projection equipment. However, this method needed to project at least sixteen fringe patterns to accurately estimate the coefficients of Fourier series, and the whole gamma precalibration process was time-consuming. The high-speed 3D shape measurement method for dynamic scenes by using bifrequency tripolar pulse-width-modulation fringe projection was designed to generate ideal fringe patterns with slight defocus, but the gamma correction of projector and camera response nonlinearity would also affect the phase unwrapping [7]. A six-step phase-shifting technique for a structured light measurement system with an off-the-shelf projector was proposed to compensate the gamma nonlinearity, but the method was no longer applicable if the measurement setup included a special projector with a gamma value greater than four [8]. In a word, the current approaches still have certain limitations [9–15]. For example, too many fringes are needed to calculate the gamma coefficient, but the process is complicated; the phase error compensation needs to calculate each phase error, and the number of phase shifts is also limited, so the calculation process is cumbersome.

Aiming at the problem of the gamma effect and phase error compensation in digital fringe projection measurement, we propose a precoded method to calibrate the gamma coefficient which depends on precoding two groups of fringe sequences with different gamma values and calculating the corresponding harmonic component proportional coefficient. Moreover, a phase error compensation method based on the three-frequency with three-phase shifts' heterodyne and phase offset is designed to reversely solve the initial phase and compensate the phase error. The experiment indicates that our method not only needs less projected fringe patterns and can effectively achieve high precision precalibration gamma coefficient but also can break through the limitation of the gamma distortion model and be compensated well, which will make the measurement system more flexible and operate easily.

The rest of this paper is organized as follows. Section 2 demonstrates the proposed method, which includes the principle of precoding calibration gamma coefficient and three-frequency with three-phase shifts' error correction and compensation method. Section 3 describes the experiments and results in detail. Conclusions are presented in Section 4.

2. Methods

2.1. Principle of Precoding Calibration Gamma Coefficient. In the digital fringe projection measurement system, gamma distortion will lead to the distortion of sinusoidal fringe, as shown in Figure 1, and the gray level of the n steps phase shifts patterns captured by the camera can be expressed aswhere (x, y) is the coordinate point in the captured image, $M(x, y)$ is the ambient light intensity and usually calculated as a constant coefficient, $B(x, y)$ is the modulation intensity of the fringe, and f is the spatial frequency of the fringe. $\varphi(x, y)$ is the phase to be demodulated, which is calculated by equation (2), $\theta_n(x, y)$ is the phase shifts value, γ is the gamma coefficient of the measurement system, and B_k is the k ($k = 1, 2, 3, \ldots, N$) order harmonic component coefficient of the sinusoidal fringe signal, $n = 0, 1, \ldots, N\text{-}1$ is the phase shifts sequence number, and N is the maximum phase shifts' steps.

$$\begin{aligned} I_n(x, y) &= \{M(x, y) + B(x, y) \times \cos[2\pi f x + \varphi(x, y) + \theta_n(x, y)]\}^{\gamma}, \\ &= M(x, y) + \sum_{k=-\infty}^{+\infty} B_k(x, y)\cos\{k \times [2\pi f x + \varphi(x, y) + \theta_n(x, y)]\}, \end{aligned} \tag{1}$$

$$\varphi(x, y) = \arctan \frac{\sum_{n=1}^{N} I_n(x, y)\sin[2\pi(n-1)/N]}{\sum_{n=1}^{N} I_n(x, y)\cos[2\pi(n-1)/N]}, \tag{2}$$

Formula (1) denotes that the gamma effect will cause the nonsinusoidal signal error of original fringe patterns and high-order harmonic components, and the coefficients of each order harmonic component are essentially functions of coefficient γ in the measurement system [16]. Therefore, the precoding calibration algorithm is designed to calculate the gamma coefficients γ and complete the precalibration gamma correction of the

measurement in this paper. The principle can be described as follows.

When $B_k \neq 0$, the ratio of the $k+1$- and k-order harmonic component of the sinusoidal signal can be expressed as

$$\frac{B_{k+1}}{B_k} = \frac{\gamma - k}{\gamma + k + 1}. \tag{3}$$

Formula (3) has established the relationship between the gamma coefficient γ and the harmonic component coefficients B_k to compensate the nonlinear of the distorted sinusoidal fringes. It is further proved that B_k converges uniformly for any $\gamma > 0$ and the amplitude of harmonic component decreases rapidly with the increase of harmonic order. Therefore, if γ is an integer, the harmonic component which is higher than γ will not be generated. Since the estimation of higher order harmonic components has the error which increases the harmonic order, it is necessary to calibrate the gamma coefficient γ of the measurement system with smaller harmonic coefficient.

The gamma coefficient γ will be obtained and calibrated through formula (3). Therefore, the idea of precoding correction is adopted to use the calibrated gamma coefficient to correct sinusoidal fringes in advance on the projection pixel plane. The nonsinusoidal fringes with gamma correction are generated on the projection plane so that the fringes are sinusoidal under the influence of the nonlinear gamma effect of the projector.

With further analysis, formula (3) is derived and calculated from the gamma distortion model of the measurement system. In the process of actual measurement, there is also defocusing problem of the projection equipment [7, 17]. Therefore, the Gaussian model of point diffusion function (PDF) was used to describe defocus to perfect the gamma nonlinear model of the projection equipment [18]. The mathematical relationship between the fringe harmonic coefficient $\hat{B}_k$ and the harmonic coefficient B_k caused by gamma effect can be expressed as

$$\frac{\hat{B}_{k+1}}{\hat{B}_k} = \exp\left[-2\pi\sigma^2 (2k+1) f_0^2\right] \times \frac{B_{k+1}}{B_k} = \exp\left[-2\pi\sigma^2 (2k+1) f_0^2\right] \frac{\gamma - k}{\gamma + k + 1}. \tag{4}$$

$\hat{B}_{k+1}$ and $\hat{B}_k$ can be obtained from the spatial discrete Fourier transform of the sinusoidal fringe pattern. If the period of projected fringe and measurement system parameter are not changed, the parameters will not be changed in the actual measurement process. Then, the exponential term in formula (4) can be regarded as a constant. However, the solution of the two-variable defocusing factors σ and gamma coefficient γ requires two sets of equations, so two coefficients γ_1 and γ_2 are preencoded on the projection pixel plane. Since the projected fringes are nonsinusoidal fringes, two sets of digital fringe patterns are obtained through the nonlinear output of the projector. On the basis of the above analysis, we set $k = 1$, and γ can be calculated by formulas (5) and (6):

$$\begin{cases} \dfrac{\hat{B}_2(\gamma_1)}{\hat{B}_1(\gamma_1)} = \exp\left[-6\pi\sigma^2 f_0^2\right] \dfrac{\gamma\gamma_1 - 1}{\gamma\gamma_1 + 2}, \\ \dfrac{\hat{B}_2(\gamma_2)}{\hat{B}_1(\gamma_2)} = \exp\left[-6\pi\sigma^2 f_0^2\right] \dfrac{\gamma\gamma_2 - 1}{\gamma\gamma_2 + 2}, \end{cases} \tag{5}$$

$$(K-1)\gamma_1\gamma_2\gamma^2 + (2K\gamma_2 - K\gamma_1 - 2\gamma_1 + \gamma_2)\gamma = 2(K-1), \tag{6}$$

where K is the result of dividing the left end of formula (5). It can be seen that K will produce a small change because of the approximate calculation of the harmonic coefficient, which leads to the large change in the gamma calibration. Since the inconsistent performance of the hardware equipment, the gamma coefficient γ should be within one to three in the actual measurement process. If the precoding selected values γ_1 and γ_2 are too closer or the reciprocal of precoding value and the real value are close, there will be a large error in the gamma calibration. Our algorithm steps are shown in Figure 2.

Step 1: precode the fringe pattern sequences. Two groups of digital fringe pattern sequences with different Gamma coefficients (i.e., $\gamma_1 = 0.60$ and $\gamma_2 = 1.00$) are precoded, and each group has twelve patterns.

Step 2: project the fringe pattern sequences. Precoding phase shifts' fringe pattern sequences are sequentially projected to calibrate the plane.

Step 3: capture the fringe pattern sequences. The precoding phase shifts' pattern sequences are captured by the camera, and the corresponding K values are calculated through formula (5).

Step 4: calculate the gamma coefficient γ from formula (6).

Step 5: generate corrected fringe patterns. γ is precoded into subsequent projection fringe patterns, that is, the fringe pattern with corrected gamma coefficient is generated and projected to the reference plane in turn.

Step 6: end.

Moreover, it is worth noting that the proposed method can correct the gamma effect of the measurement system to a certain extent and improve the measurement accuracy, but

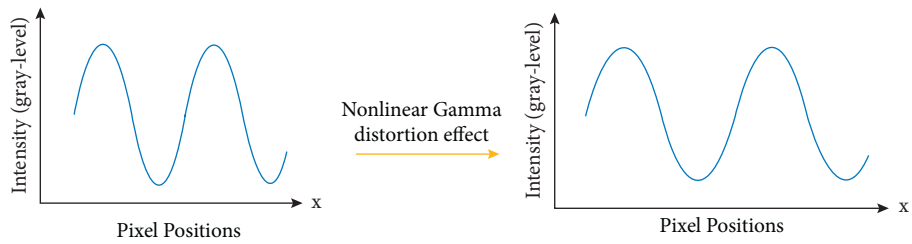

Figure 1: The schematic diagram of the distortion gamma sinusoidal signals.

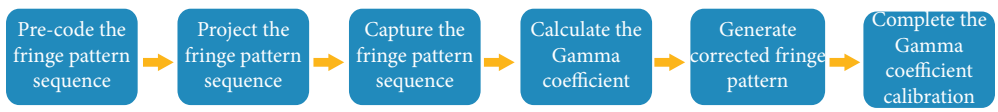

Figure 2: The flowchart of the proposed calibration algorithm of the gamma coefficient.

the active precoding method still has inevitable phase errors, so we propose a method to solve the phase error problem in Section 2.2.

2.2. Three-Frequency with Three-Phase Shifts' Error Correction and Compensation Method. In digital fringe projection measurement technology, multifrequency heterodynes based on the phase shifts' method is usually used to calculate the phase, but it needs to establish the gamma model, and the proposed precoding gamma coefficient calibration will also inevitably lead to the phase error. Therefore, a phase error compensation method based on the three-frequency with three-phase shifts and phase offset is designed to compensate the phase error and improve the accuracy of phase calculation after gamma correction. Our method not only effectively reduces the noise interference but also reduces the number of projection fringe patterns and improves the measurement speed, and it will be widely used in various 3D measurement fields by further research.

2.2.1. Reverse Calculation Initial Phase Method Based on Three-Frequency with Three-Phase Shifts. The multifrequency heterodyne method usually projects sinusoidal fringe pattern sequence with multifrequency to measure the object, and then, a set of phase distribution with smaller frequency will be obtained from their heterodyne calculation [19, 20]. Therefore, it is necessary to select both the sinusoidal fringe with appropriate frequency and the appropriate period T_1, T_2, and T_3. Then, the period width after superposition is larger than the width of projected fringe pattern, that is, $T_{123} > 1$. The projection width of the projector is 1140 pixels in our experiment. Considering the above two factors and making the numbers of projected fringe patterns as less as possible, the three-frequency with the three-phase shifts' method is designed to increase the measurement speed, that is, each group of fringe sequences has three-phase shifts with different frequencies. The period width of the three-frequency fringe patterns with three-phase shifts is

$$\begin{cases} T_1 = 14\,\text{pixels} \\ T_2 = 15\,\text{pixels} \\ T_3 = 16\,\text{pixels} \end{cases} \tag{7}$$

$$T_e = \frac{T_1 \times T_2}{|T_2 - T_1|}. \tag{8}$$

The superposition period T_e can be calculated by formula (8), and the equivalent period after superposition can be solved as

$$\begin{cases} T_{12} = 210\,\text{pixels}, \\ T_{23} = 240\,\text{pixels}, \\ T_{123} = 1680\,\text{pixels}. \end{cases} \tag{9}$$

The three-frequency with four-phase shifts' method needs to project three groups of fringe patterns with different frequencies, and 12 fringe patterns are used to calculate the phase by the four-step phase shifts' method. In the actual measurement process, the measurement speed and noise factors also need to be considered. Therefore, the three-frequency with three-phase shifts' method is proposed, that is, the projector projects three groups of fringe patterns with different frequencies to calculate the phase by three-phase shifts' method. So, only a total of 9 fringe patterns are needed, which can obviously improve the measurement speed. Meanwhile, unlike the traditional multifrequency heterodyne using heterodyne phase Φ_{123} to reconstruct 3D information, we proposed that the initial phase is calculated by using three-frequency with three-phase shifts' reverse solution, which can reduce the phase error. For the three-step phase shifts, the increment of each phase shift is

$$I_n = I_a + I_b \cos\left(\varphi + \frac{2q\pi}{3}\right),\ q = 0, 1, 2, \tag{10}$$

where I_n represents the intensity distribution of the fringe pattern, I_a is the intensity mean, I_b represents the amplitude modulation, and φ is the initial phase. Then, the theoretical value of the wrapped phase can be solved as

$$\varphi = \arctan\left[\frac{\sqrt{3}\,(I_1 - I_3)}{2I_2 - I_1 - I_3}\right]. \tag{11}$$

Reverse solution of the initial phase is calculated from the final heterodyne phase Φ_{123}; then, the absolute phase is calculated reversely corresponding to the second and the first heterodyne phases, so the absolute phase is finally obtained corresponding to the initial wrapped phase. The absolute phase with small period will be used for 3D reconstruction.

The key to the reverse solution of the initial phase is to calculate the series $k\,(x, y)$ of each the wrapped phase and the corresponding equivalent period. The solution of the series $k\,(x, y)$ is adopted as the following two formulas:

$$k(x, y) = \text{round}\left[\frac{T_A/T_B \times \Phi_A - \varphi_B}{2\pi}\right], \tag{12}$$

$$k(x, y) = \text{floor}\left[\frac{T_A/T_B\Phi_A - \varphi_B}{2\pi} + 0.5\right], \tag{13}$$

where *round* represents rounding, Φ_A represents the absolute phase calculated by the fringe pattern with larger period, φ_B is the wrapped phase to be obtained, T_A is the larger period, T_B is the smaller period, and *floor* represents the downward rounding. Formula (12) is used to reduce the noise interference when the noise of the fringe pattern is large and calculate the corresponding series $k\,(x, y)$. Formula (13) is used when the noise of the fringe pattern is small.

The absolute phase can be obtained from

$$\Phi(x, y) = \varphi(x, y) + 2\pi \times k(x, y). \tag{14}$$

The reverse calculation initial phase method based on three-frequency with three-phase shifts' algorithm is described as follows:

Step 1: the absolute phase $\Phi_{123}\,(x, y)$ is used to unwrap the wrapped phase $\varphi_{23}(x, y)$, the series $k_{23}(x, y)$ is obtained by formula (12), and the absolute phase $\Phi_{23}\,(x, y)$ is obtained by formula (14).

Step 2: the absolute phase $\Phi_{23}\,(x, y)$ is used to unwrap the wrapped phase $\varphi_{12}(x, y)$, the series $k_{12}(x, y)$ is obtained by formula (12), and the absolute phase $\Phi_{12}\,(x, y)$ is obtained by formula (14).

Step 3: the absolute phase $\Phi_{12}\,(x, y)$ is used to unwrap the wrapped phase $\varphi_3(x, y)$, the series $k_3(x, y)$ is obtained by formula (12), and the absolute phase $\Phi_3\,(x, y)$ is obtained by formula (14).

Step 4: the absolute phase $\Phi_3(x, y)$ is used to unwrap the wrapped phase $\varphi_2(x, y)$, the series $k_2\,(x, y)$ is obtained by formula (12), and the absolute phase $\Phi_2\,(x, y)$ is obtained by formula (14).

Step 5: the absolute phase $\Phi_2(x, y)$ is used to unwrap the wrapped phase $\varphi_1(x, y)$, the series $k_1\,(x, y)$ is obtained by formula (12), and the absolute phase$\Phi_1\,(x, y)$ is obtained by formula (14).

Step 6: the obtained $k_1\,(x, y)$ in the Step 5 is combined with wrapped phase of the first set of frequencies. The absolute phase of the first of frequencies is calculated by formula (14), that is, the absolute phase $\Phi_{\text{final}}(x, y)$ is required for reconstruction.

2.2.2. Phase Error Compensation Method Based on Phase Offset. As mentioned above, this paper proposes a reverse solution of initial phase based on three-frequency with three-phase shifts' method. Although the solution of the absolute phase is fast and robust, the distortion of the sinusoidal fringe pattern caused by nonlinear response of acquisition equipment and gamma nonlinearity of projection equipment will also lead to the phase error. Hence, the compensation algorithm based on the phase offset is proposed for three-frequency with three-phase shifts' method.

In order to facilitate the analysis and process of the image, the gray level of the fringe patterns can be represented by

$$I_n(x, y) = A + B\cos\left[2\pi f x + \varphi(x, y) + \delta_n\right], \tag{15}$$

where A corresponds the direct current (DC) term and ambient light intensity reflected by the object and B represents the modulation or contrast of the fringes; they are usually constant. f is the frequency of sinusoidal fringe, $\varphi\,(x, y)$ only contains phase information, and δ_n represents the phase shifts of the fringe pattern. During the experiment, we use the three-frequency with the three-phase shifts' method, so the specific phase shifts values are $-2\pi/3$, 0, $2\pi/3$.

The intensity distribution of the projected fringe pattern can be expressed by

$$I^p(x, y) = f_p\left(I_n(x, y)\right), \tag{16}$$

where f_p is the projector mapping function relationship between the input signal and the output signal. Assuming that the intensity of ambient light on the measured surface is I_a and the reflectivity of the measured surface is r, so the light intensity distribution captured by the photosensitive elements of the industrial camera is

$$I^r(x, y) = r\left[I^{\text{p}}(x, y) + I_a(x, y)\right]. \tag{17}$$

Similarly, if f_c is used as the nonlinear response function between the input and output signals of the industrial camera and the ambient light intensity is I_a', the output image of the camera can be expressed as

$$I^c(x, y) = f_c\left[I^r(x, y) + I_a'(x, y)\right]. \tag{18}$$

When the camera produces the phenomenon of energy ratio imbalance in the process of photoelectric signal conversion, the conversion function of the camera is a nonlinear function. Factors that have the greatest influence on camera nonlinear response include second-order and third-order

nonlinear signal response. Therefore, the nonlinear response of the camera can be expressed by

$$I^c(x,y) = q_3\left[I^r(x,y) + I_a'(x,y)\right]^3 + q_2\left[I^r(x,y) + I_a'(x,y)\right]^2 + q_1\left[I^r(x,y) + I_a'(x,y)\right] + q_0. \tag{19}$$

q_3, q_2, q_1, and q_0 are the fitting coefficients. If the gamma coefficient γ of the measurement system is considered and formula (19) is substituted into formulas (18) and (16), then it will be transferred as follows:

$$I^c(x,y) = k_3\left[I_n(x,y)\right]^{3\gamma} + k_2\left[I_n(x,y)\right]^{2\gamma} + k_1\left[I_n(x,y)\right]^{\gamma} + k_0. \tag{20}$$

k_3, k_2, k_1, and k_0 are also the fitting coefficients after transformation calculation in formula (20). It is concluded that there is actually a nonlinear response of order 3γ in the measurement system. On the contrary, the higher order nonlinearity of the system can be represented through the higher harmonics of the system. Therefore, the image response equation of the measurement system can be expressed as

$$I^c(x,y) = f\left[I_n(x,y)\right] = A + \sum_{k=1}^{k} A_k \cos\left(k\left[\varphi(x,y) + \delta_n\right]\right), \tag{21}$$

where A_k is the harmonic coefficient and k is the maximum number of harmonics. Furthermore, through these above derivations, the phase distribution of the phase diagram can be calculated:

$$\varphi(x,y) = -\arctan\left[\frac{\sum_{N=0}^{N-1}\left\{A + \sum_{k=1}^{k} A_k \cos\left(k\left[\varphi(x,y) + \delta_n\right]\right)\right\}\sin\left(\delta_n\right)}{\sum_{N=0}^{N-1}\left\{A + \sum_{k=1}^{k} A_k \cos\left(k\left[\varphi(x,y) + \delta_n\right]\right)\right\}\cos\left(\delta_n\right)}\right]. \tag{22}$$

Generally, the error with more than the fifth harmonic is small and negligible, so the value range of k is generally less than 5. The three-step phase shifts method was used to calculate the principal phase in the experiment, and the calculation of the wrapped phase is expressed by

$$\varphi(x,y) = \arctan\left[\frac{A_1 \sin[\varphi(x,y)] - A_2 \sin[2\varphi(x,y)] + A_4 \sin[4\varphi(x,y)] - A_5 \sin[5\varphi(x,y)]}{A_1 \cos[\varphi(x,y)] - A_2 \cos[2\varphi(x,y)] + A_4 \cos[4\varphi(x,y)] - A_5 \cos[5\varphi(x,y)]}\right], \tag{23}$$

where A_i ($i = 1, 2, 4, 5$) is the coefficient of the i order harmonic. The ideal phase can be expressed as

$$\varphi(x,y) = \varphi'(x,y) - \Delta\varphi(x,y) \tag{24}$$

The phase error is able to be obtained by combining formulas (23) and (24):

$$\begin{aligned}\Delta\varphi(x,y) &= \arctan\left[\frac{-(A_2 - A_1)\sin\left[3\varphi(x,y) - A_5 \sin[6\varphi(x,y)]\right]}{A_1 + (A_2 + A_4)\cos\left[3\varphi(x,y) + A_5 \cos[5\varphi(x,y)]\right]}\right] \\ &\cong -m_1 \sin[3\varphi(x,y)] - m_2 \sin[6\varphi(x,y)]\end{aligned} \tag{25}$$

where m_1 and m_2 are constants and m_2 is negligible compared with m_1; then, formula (25) can be expressed as

$$\Delta\varphi(x,y) \cong -m_1 \sin[3\varphi(x,y)] \tag{26}$$

If we do not consider the influence of the fifth harmonic, we should fit the phase error formula as follows:

$$\Delta\varphi(x,y) \cong -\frac{m_1 \sin[3\varphi(x,y)]}{1 + \cos[3\varphi(x,y)]} \tag{27}$$

In the experiment, $-m_1/1 + \cos[3\varphi(x,y)]$ is constant fluctuation in 2π period, so we set $k = -m_1/1 + \cos[3\varphi(x,y)]$; then, the phase error can be expressed as follows:

$$\Delta\varphi(x,y) \cong k \sin[3\varphi(x,y)] \tag{28}$$

According to the above analysis, the phase error is determined by phase φ and parameter k in our method. If an initial phase offset is introduced into the phase shifts' fringe pattern, the phase error will also change accordingly.

The core idea of the proposed method is that the sequence of fringe patterns with an initial phase offset difference of $\pi/3$ is designed, that is, a set of compensation fringe patterns should be added on the basis of the projection fringe pattern sequence. The phase error of the corresponding wrapped phase can be expressed as follows:

$$\Delta\varphi'(x, y) \cong k \sin\left[3\left(\varphi(x, y) - \frac{\pi}{3}\right)\right] \cong -k \sin[3\varphi(x, y)] \tag{29}$$

It is not difficult to find that the phase error has the equation $\Delta\varphi(x, y) + \Delta\varphi'(x, y) = 0$. Therefore, if there are three different periods and $-\pi/3$ initial phase offsets for the projection fringe patterns, it has nine patterns. The sinusoidal fringe pattern has a phase angle difference of $2\pi/3$; then, the corresponded original wrapped phase and the wrapped phase of the compensation fringe are calculated by the three-step phase shifts' method. After that, two groups of wrapped phases are added together. The phase error due to the gamma nonlinear effects of the projector is eliminated. After a lot of experiments, the k value is $N\pi$, and N is the maximum phase shifts' numbers obtained during the measurement.

3. Experiment and Results

The calibration method of the precoding gamma coefficient was simulated to verify the effectiveness. Suppose that the original gamma coefficient of the uncorrected measurement system was 0.80; the precoding values were generally between 0.50 and 1.00, which were independent of the measurement range and measurement distance. So, the precoding method was used to encode two sets of digital fringes with gamma coefficient $\gamma_1 = 0.60$ and $\gamma_2 = 1.00$, as shown, respectively, in Figures 3(b) and 3(c). Then, the actual gamma coefficients of the captured fringe patterns should be 0.50 and 0.80 in the measurement process.

The effect of high-order harmonic component on the phase was determined by the number of phase shift steps. The more fringe patterns projected, the smaller the influence of the high-order harmonic component is. Therefore, the phases obtained by 12-step phase shift were regarded as the ideal value to improve the measurement speed and obtain more accurate measurement results in this paper. 12 fringe patterns were generated and the phase shifts between each of the two patterns was fixed to $\pi/12$. When the gamma coefficient of the properly precoding fringe was 1.638 (as shown in Figure 4(a)), the fringe pattern with the best positive linearity could be captured by the camera (as shown in Figure 4(b)). In this case, the gamma coefficient of the projected fringe was $0.8 \times 1.638 = 1.3104$.

In Figure 4(c), the red dotted line presented the gray level of the fringe after gamma correction, and the blue solid line was the uncorrected gray level of the fringe. From Figures 4(d) and 4(e), it could be seen that the uncorrected fringe had obvious nonsinusoidal distortion at the peak and valley, and the sine of the projected fringe by precoding gamma coefficient calibration was much better than uncorrected fringe. In addition, the proposed method was able to effectively eliminate the effects of harmonic components from the perspective of spectrum, as shown in Figures 5 and 6.

Moreover, we calculated the root mean square (RMS) of error from which the gray level of the original gamma distortion minus the gray level of the standard sinusoidal fringe, which was shown in Table 1, and the RMS was 0.0297. While the RMS of other error between the fringe intensity corrected by the proposed method and the gray level of the standard sinusoidal fringe was 0.0058.

We normalized the gray level uniformly to facilitate comparison, and it could be seen that the gray level of the fringe error was greatly reduced by nearly 80% after precoding gamma calibration method, which could fully prove the effectiveness of our proposed algorithm.

During the whole measurement process, the standard sinusoidal fringe patterns were generated and projected onto the measured surface, and the camera was used to capture the deformed fringes. Subsequently, the wrapped phase was extracted and filtered, and the precoded method and phase error compensation method were used to correct gamma distortion and compensate the phase error. After that, the wrapped phase and absolute phase of the fringe were compared to verify the effectiveness of the proposed method. Aluminum material with surface reflectivity of 0.4–0.5 was used as the measured surface, and the verification experiment of 3D measurement was carried out.

According to Figure 7, the experiment system was built, and the optical measurement platform is shown in Figure 8. The experimental platform was the structured light measurement system based on digital phase shifts' fringe projection, which was mainly composed of computer, camera, and digital projector. The digital projector was DLP4500, which could realize RGB three-channel projection, and the effective resolution was 1140 pixels × 912 pixels. This device could project patterns quickly. The camera (Point Gray, GS3-U3-32S4M) had the maximum resolution of 2048 pixels × 1536 pixels, and the maximum frame frequency of is 121 fps.

Specific measurement steps were as follows:

Step 1: the gamma distortion effect of measurement system was precoded and calibrated according to the principle and method of Section 2.1.

Step 2: according to the theory described in Section 2.2.1, three different periodic fringe patterns T1, T2, and T3 were coded and designed to be flashed into the DLP4500, and the device projected them onto the measured surface and

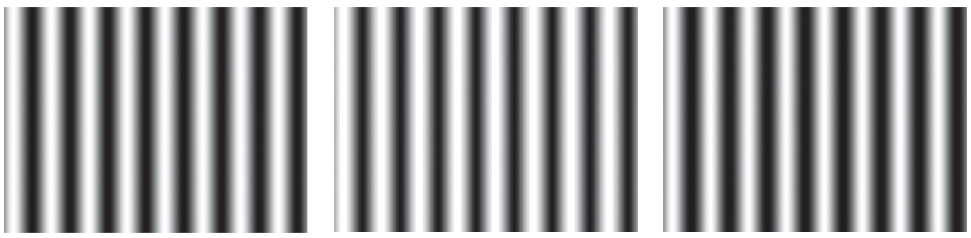

(a) (b) (c)

Figure 3: The original precoding fringe and actual fringe. (a) Original gamma = 0.80. (b) Precoding gamma = 0.60. (c) Precoding gamma = 1.00.

captured them. The equivalent periodic T12, T23, and T123 were calculated simultaneously.

Step 3: the three-step phase shifts' method was used to obtain the initial values of 9 fringe patterns captured by the camera so that the principal phase values of each pixel were $\varphi 1$, $\varphi 2$, and $\varphi 3$, respectively.

Step 4: the principal values $\varphi 12$ and $\varphi 23$ of intermediate phases were obtained by using $\varphi 1$, $\varphi 2$, and $\varphi 3$ solution from formulas (30) and formula (31):

$$\varphi_{12} = \left\{ \begin{array}{ll} \varphi_1 - \varphi_2, & \varphi_1 \geq \varphi_2 \\ \varphi_1 - \varphi_2 + 2\pi, & \varphi_1 < \varphi_2 \end{array} \right\}, \tag{30}$$

$$\varphi_{23} = \left\{ \begin{array}{ll} \varphi_2 - \varphi_3, & \varphi_2 \geq \varphi_3 \\ \varphi_2 - \varphi_3 + 2\pi, & \varphi_2 < \varphi_3 \end{array} \right\}. \tag{31}$$

Step 5: the absolute phase value $\Phi 123$ of the heterodyne was obtained by taking the principal phase value $\varphi 12$ and $\varphi 23$ of the intermediate phase as the parameters of the heterodyne calculation.

Step 6: initial phase was solved reversely, and $\Phi 1(x, y)$ with maximum frequency was obtained as the final phase.

Step 7: according to the theory described in Section 2.2.2, the compensated fringe sequences were projected and the compensated phase value was calculated as the final phase value that could be reconstructed the 3D information.

Phase error compensation process and its results were shown in Figure 9. The projected fringes and the compensation fringe patterns were shown in the gray box, the corresponding wrapped phase, and the heterodyne calculation diagrams were shown in the green box, and the calculated absolute phases were shown in the yellow box. The final compensated absolute phase was shown in the blue box, that is, the phase was the required in the final 3D reconstruction.

In this paper, the wrapped phase obtained by the three-frequency with the four-phase shifts' method was compared with that obtained by our method to analyze the feasibility of our method. The phase measurement error of 800 columns corresponding to the wrapped phase diagram was shown in Figure 10. Then, we normalized the error between 0 and 1 to facilitate comparison, and it could be seen from Figure 10(c) that the proposed method could effectively reduce the phase error fluctuation and improve its measurement accuracy.

Furthermore, we compared the final absolute phase obtained by the three-frequency with the four-phase shifts' method with our proposed method to analyze the phase error fluctuation and compensation. The phase error comparison of line 400 of the absolute phase image is shown in Figure 11. The error was normalized from 0 to 1 to facilitate comparison, and it could be seen that the phase fluctuation based on the three-frequency with the four-phase shifts' method was large, and the whole phase expansion was greatly affected by noise, so there were many burrs. The expanded phase had the defect of drawing wire. Meanwhile, we noted that the phase error at the origin had accumulated, which was unfavorable to the 3D reconstruction, and the inverse solution method based on three-frequency with three-phase shifts could obviously see that the error accumulation at the origin was very small, the phase change was smooth, and the burr was less. It was much better than the three-frequency with four-phase shifts' method. Therefore, our proposed method had good absolute phase noise resistance, good robustness, and higher width tolerance.

Subsequently, the fringe patterns with the period of 14 pixels, 24pixels, and 32pixels were projected onto the measured surface, and the RMS of phase errors before and after correction and compensation were calculated. The results were shown in Table 2, and it could be found that the proposed correction compensation method could effectively reduce the phase error caused by gamma effect.

In the 3D reconstruction experiment, the projector firstly was used to project the sinusoidal fringe sequences generated by the precoding gamma coefficient calibration correction. Then, the camera captured the modulated fringe patterns, and the absolute phase of the measured surface was obtained by using the proposed method based on the reverse solution initial phase method and the three-frequency with three-phase shifts' error compensation based on phase offset. After that, the 3D reconstruction data of the measured surface could be obtained, as shown in Figure 12. We compared the 3D reconstruction image after digital fringe gamma correction and phase error compensation, and the effectiveness of our method could be verified.

Figure 12(a) shows that the measured surface would appear obvious wave distortion after 3D reconstruction. The reason for this phenomenon was the gamma distortion of

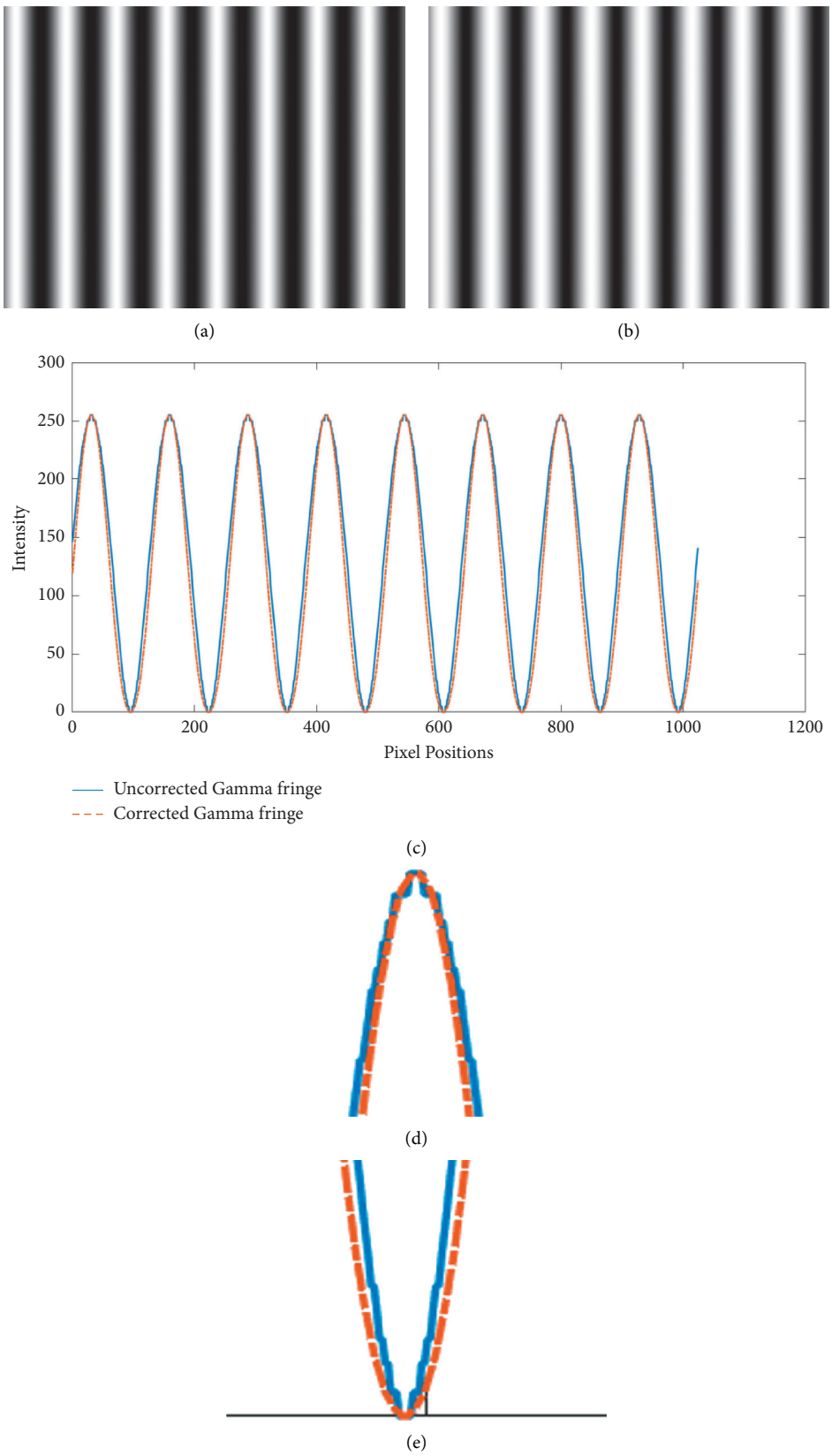

Figure 4: Simulation results. (a) Precoding fringe with gamma = 1.638. (b) Captured fringe simulation. (c) Sinusoidal contrast of fringe before and after correction. (d) Contrast of sine wave crest. (e) Contrast of sine wave valley.

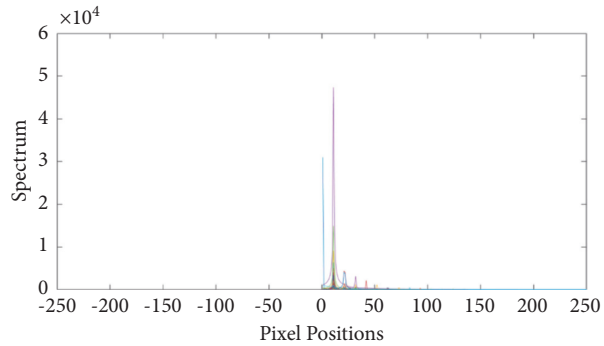

Figure 5: Uncorrected gamma = 0.80, spectrum display diagram.

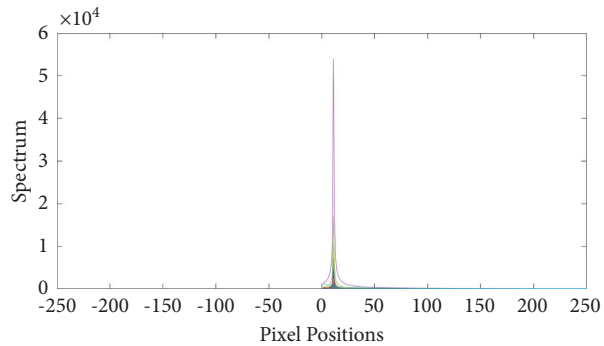

Figure 6: Corrected gamma = 1.3104, spectrum display diagram.

Table 1: RMS before and after correction of the gamma coefficient.

Error before correction RMS (rad)	Error after correction RMS (rad)	Ratio of RMS of phase error before and after correction compensation	Sinusoidal precision of ratio improvement (%)
0.0297	0.0058	5.12	80

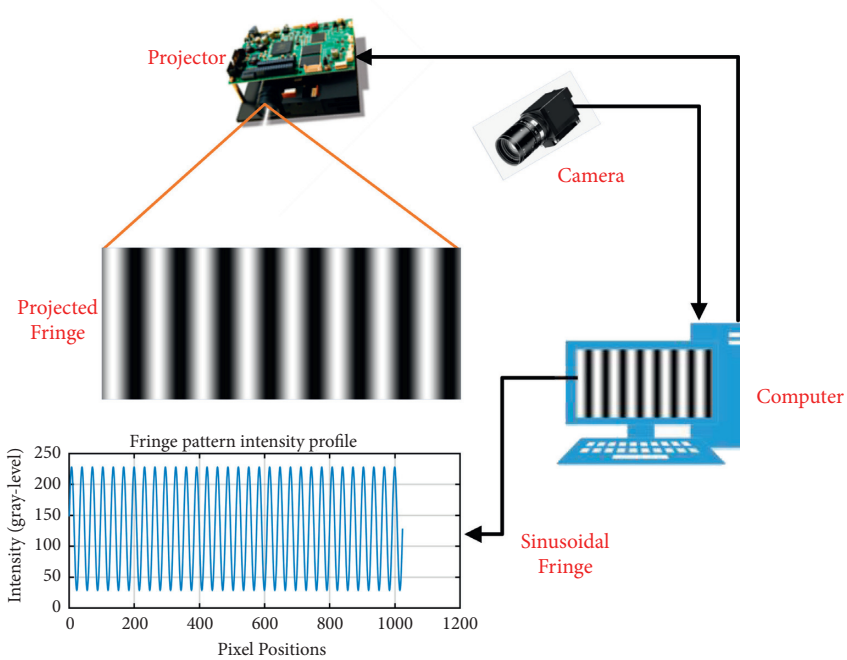

Figure 7: Schematic diagram of the digital fringe projection measurement system.

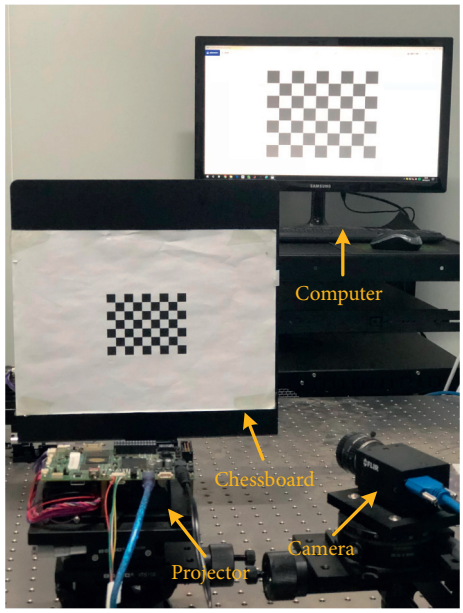

Figure 8: Hardware implement.

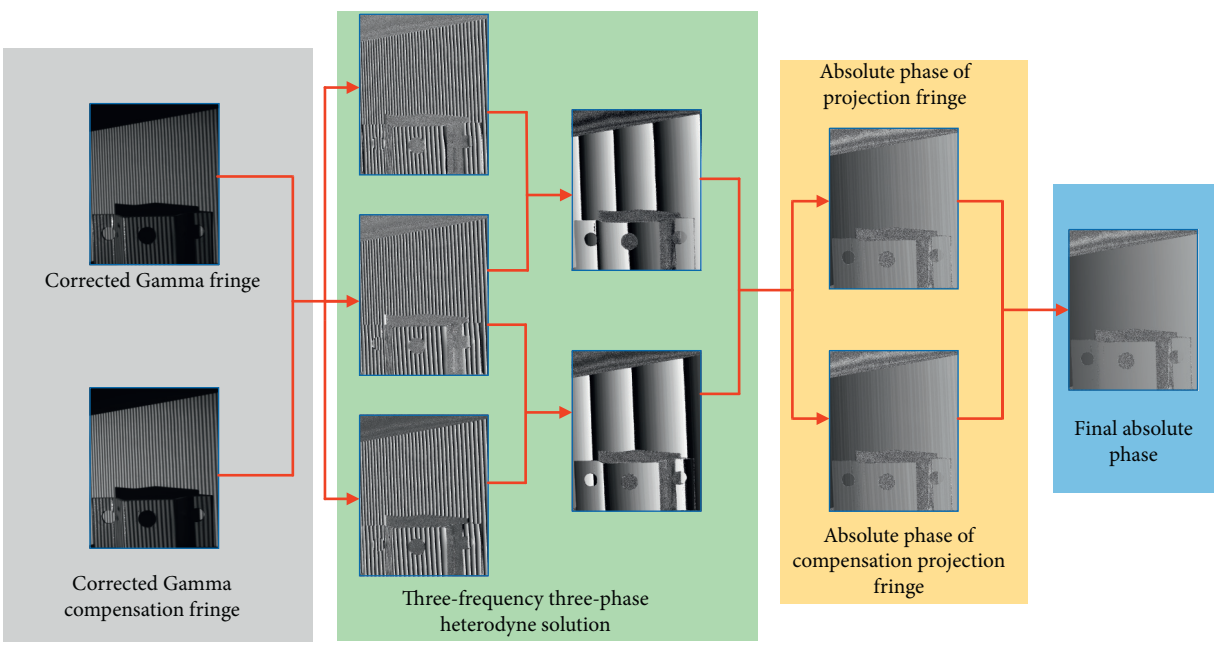

Figure 9: Schematic diagram of phase error compensation measurement.

the fringe patterns, which caused the phase error. Figure 12(b) could draw the conclusion that the distortion degree was obviously reduced and the reconstructed surface was smoother and clearer after phase error compensation and gamma correction based on our method. The missing part of the reconstruction was due to the fact that the monocular structured light measurement system was unable to measure the shadow part.

Then, we compared and analyzed the quality of the model data and the original point cloud data. We set the deviation value, one side of the reference plane was negative, and the other side was positive value. The maximum and minimum distances from the point to the plane were calculated by the least square fitting plane. The average error and the standard deviation were calculated, as shown in Tables 3 and 4, which were used to evaluate quantitatively the validity of the proposed method.

From the above tables, the average error of the absolute direction was reduced by 83.02%. The forward average error was decreased by 85.71%. In a word, the distortion of the wave shape was obviously reduced after correction and compensation, and the effect of correction and compensation was ideal, so the effectiveness of the proposed method could be verified.

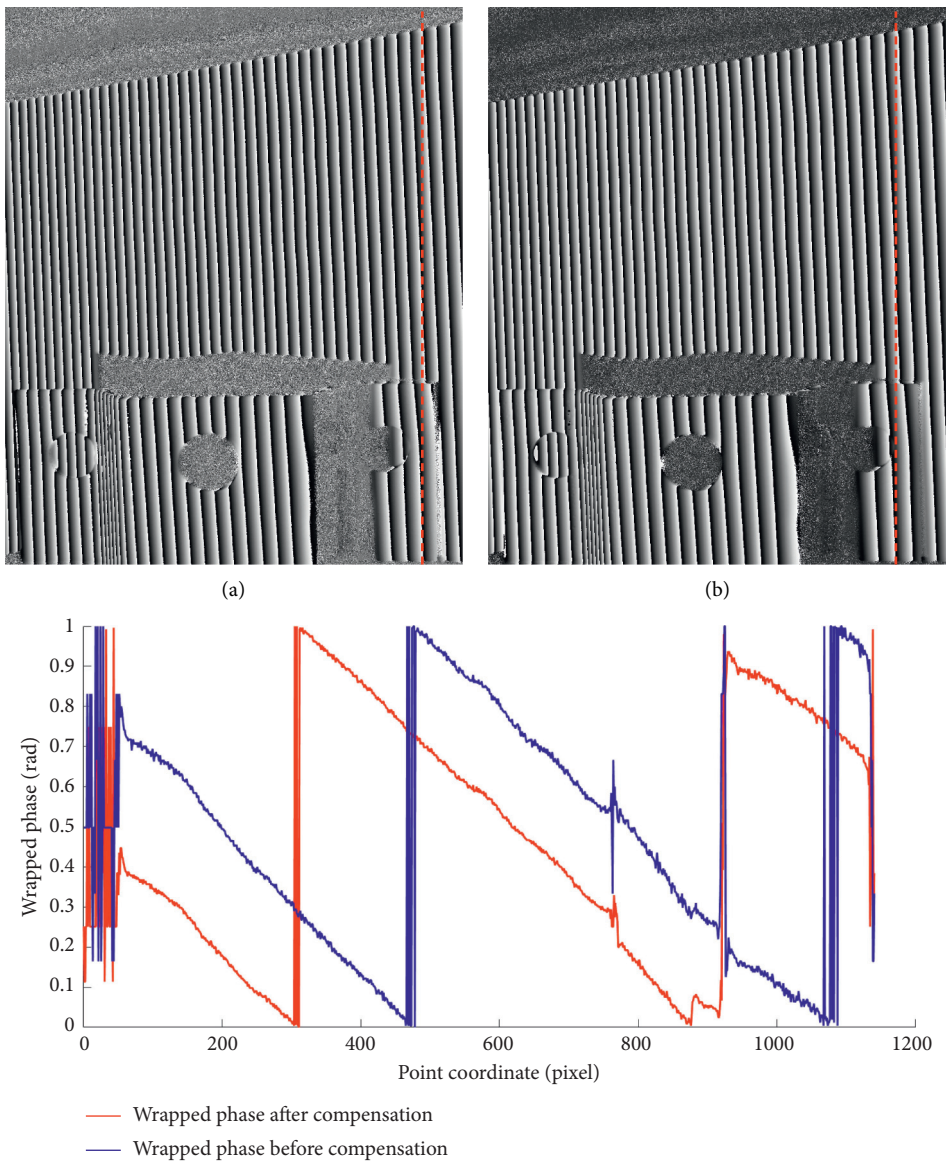

Figure 10: Comparison of wrapped phase error compensation. (a) Our proposed method; (b) three-frequency with four-phase shifts' method; (c) comparison of wrapped phase measurement errors in 800 columns.

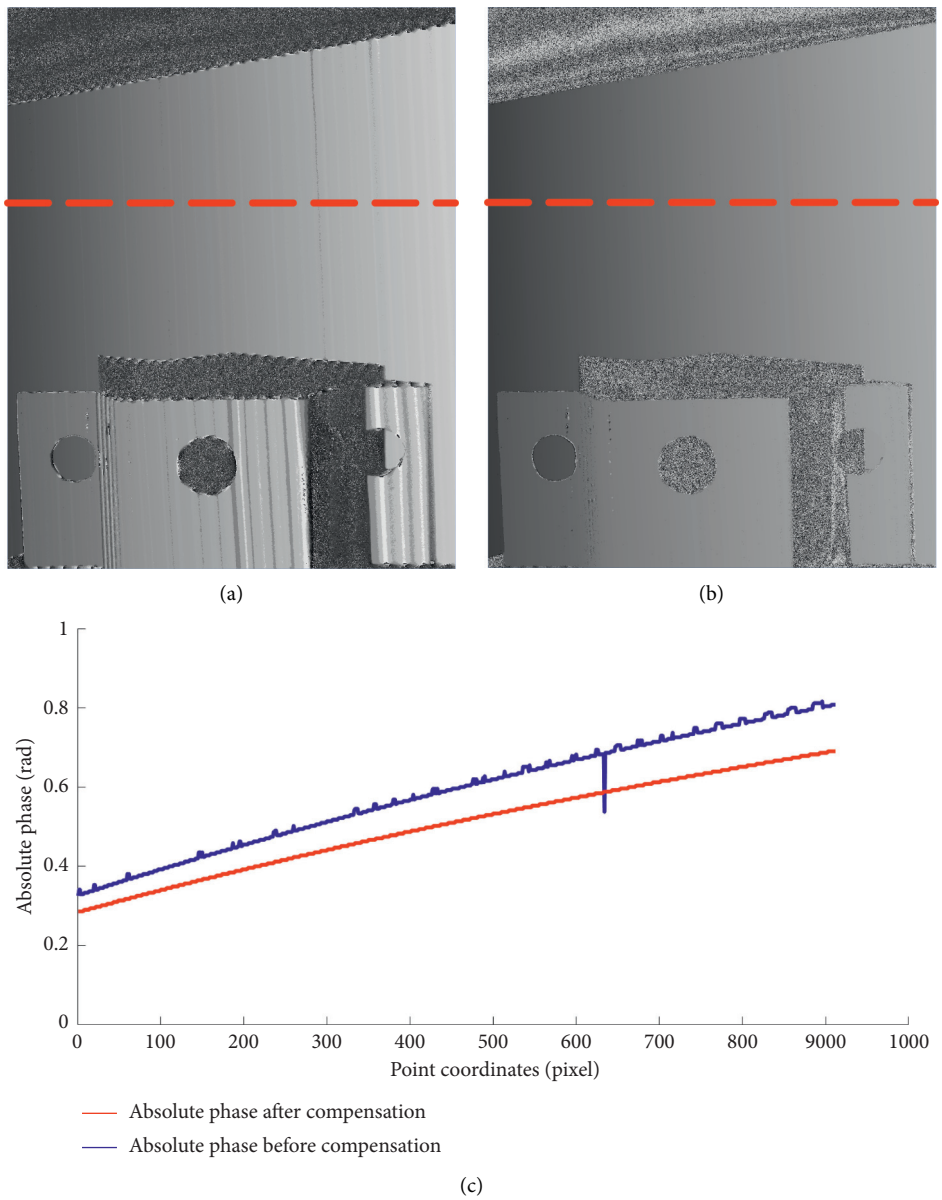

Figure 11: Comparison of absolute phase error compensation. (a) Three-frequency with four-phase shifts' method; (b) our proposed method; (c) comparison of absolute phase measurement errors in 400 lines.

Table 2: RMS before and after correction of compensation by the proposed method.

Fringe period (pixels)	Error before correction RMS (rad)	Error after correction RMS (rad)	Ratio of RMS of phase error before and after correction compensation
14	0.0186	0.0084	2.21
24	0.0299	0.0124	2.41
32	0.0275	0.0132	2.08

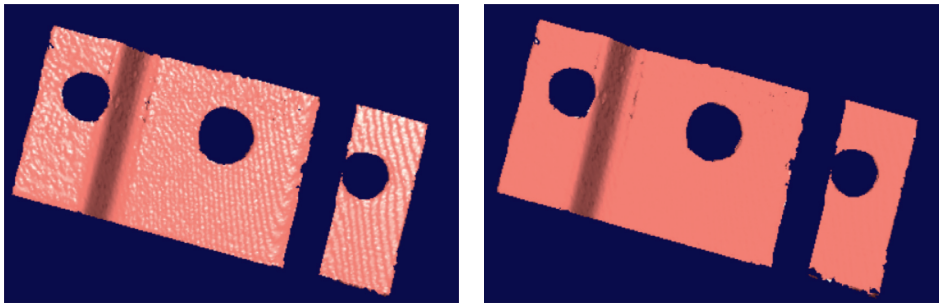

(a) (b)

Figure 12: 3D reconstructions of the aluminum material. (a) Three-frequency with four phase shifts. (b) Our proposed method.

Table 3: Evaluation and analysis of point cloud by the traditional phase-shifted method for Figure 12(a).

Direction	Maximal value (mm)	Average error (mm)	Standard deviation (mm)
Negative direction	−3.8620	−0.7231	0.7404
Absolute direction	3.8620	0.0159	0.1649
Forward direction	3.3378	0.0091	0.1129

Table 4: Evaluation and analysis of point cloud by our proposed method for Figure 12(b).

Direction	Maximal value (mm)	Average error (mm)	Standard deviation (mm)
Negative direction	−3.0667	−0.7231	0.6130
Absolute direction	3.8603	0.0027	0.1010
Forward direction	3.6375	0.0013	0.0536

4. Conclusions

In this paper, the mathematical relationship between higher harmonic component and gamma coefficient is analyzed and deduced, and an active precoding method is proposed to calibrate the nonlinear gamma coefficient of the system. Meanwhile, since gamma nonlinear error will cause the phase error, this paper also proposes the reverse solution initial phase method based on three-frequency with three-phase shifts and the phase error compensation method based on phase offset. Aluminum material was taken as the measured surface, and the experimental results showed that the RMS values of the difference between the phase plane and the standard phase plane before and after gamma correction were reduced by nearly 80%. Compared with the traditional three-frequency with four-phase shifts' method, the proposed method needed less compensation fringe patterns and had less phase error. Our method had good noise resistance, which could be used in many measurement situations. However, our method also has some limitation. Noise and uncertainty will have a great impact on the measurement accuracy, so the follow-up work will improve the quality from the image acquisition and processing.

Data Availability

The data used to support the findings of this study are included within the article.

Conflicts of Interest

The authors declare no conflicts of interest.

Acknowledgments

This research was funded by the National Natural Science Foundation of China (Grant no. 51805153), State Key Laboratory of Precision Measuring Technology and Instruments (Tianjin University) (pilab1801), Announcement Project of Hubei Province (2019AEE014), and College Students' Innovation and Entrepreneurship Training Program of Hubei Province (S202010500035).

References

[1] V. L. Tra and Y. Lin, "A structured light RGB-D camera system for accurate depth measurement," *International Journal of Optics*, vol. 2018, p. 7, Article ID 8659847, 2020.

[2] H. Guo, H. He, and M. Chen, "Gamma correction for digital fringe projection profilometry," *Applied Optics*, vol. 43, no. 14, pp. 2906–2914, 2004.

[3] S. Ma, C. Quan, R. Zhu, L. Chen, B. Li, and C. J. Tay, "A fast and accurate gamma correction based on Fourier spectrum analysis for digital fringe projection profilometry," *Optics Communications*, vol. 285, no. 5, pp. 533–538, 2012.

[4] S. Zhang and S. P. Huang, "Phase error compensation for a 3D shape measurement system based on the phase-shifting method," *Optics Engineering*, vol. 46, no. 6, pp. 063601–063609, 2007.

[5] Y. Xu, L. Ekstrand, J. Dai, and S. Zhang, "Phase error compensation for three-dimensional shape measurement with projector defocusing," *Applied Optics*, vol. 50, no. 17, pp. 2572–2581, 2011.

[6] Z. Li and Y. Li, "Gamma-distorted fringe image modeling and accurate gamma correction for fast phase measuring profilometry," *Optics Letters*, vol. 36, no. 2, pp. 154–156, 2011.

[7] C. Zuo, Q. Chen, and G. H. Gu, "High-speed three-dimensional shape measurement for dynamic scenes using bi-frequency tripolar pulse-width-modulation fringe projection," *Optics and Lasers in Engineering*, vol. 51, no. 13, pp. 953–960, 2013.

[8] H. Cui, T. Jiang, X. Cheng, W. Tian, and W. Liao, "A general gamma nonlinearity compensation method for structured light measurement with off-the-shelf projector based on unique multi-step phase-shift technology," *Journal of Modern Optics*, vol. 66, no. 15, pp. 1579–1589, 2019.

[9] K. Yatabe, K. Ishikawa, and Y. Oikawa, "Compensation of fringe distortion for phase-shifting three-dimensional shape measurement by inverse map estimation," *Applied Optics*, vol. 55, no. 22, pp. 6017–6024, 2016.

[10] Y. Zhang, Z. L. Zhang, and Y. Q. Li, "Phase measuring method and error compensation in 3D profile measurement," *10th International Symposium on Precision Engineering Measurements and Instrumentation (ISPEMI)*, vol. 11053, 2019.

[11] L. Geng, Y. Liu, Z. Xiao et al., "Phase unwrapping method based on heterodyne three frequency non-equal step phase shift," *Lecture Notes in Computer Science*, vol. 9279, pp. 68–79, 2015.

[12] X. F. Wang, H. Fan, and J. Ma, "Three-dimensional reconstruction based on tri-frequency heterodyne principle," *Procedia Computer Science*, vol. 183, pp. 596–602, 2021.

[13] C. Zuo, L. Huang, M. Zhang, Q. Chen, and A. Asundi, "Temporal phase unwrapping algorithms for fringe projection profilometry: a comparative review," *Optics and Lasers in Engineering*, vol. 85, pp. 84–103, 2016.

[14] Z. Cai, X. Liu, X. Peng et al., "Phase error compensation methods for high-accuracy profile measurement," *Measurement Science and Technology*, vol. 27, no. 4, Article ID 045201, 2016.

[15] T. Hoang, B. Pan, D. Nguyen, and Z. Wang, "Generic gamma correction for accuracy enhancement in fringe-projection profilometry," *Optics Letters*, vol. 35, no. 12, pp. 1992–1994, 2010.

[16] K. Liu, Y. Wang, D. L. Lau, Q. Hao, and L. G. Hassebrook, "Gamma model and its analysis for phase measuring profilometry," *Journal of the Optical Society of America A*, vol. 27, no. 3, pp. 553–562, 2010.

[17] Z. Li and Y. Li, "Gamma-distorted fringe image modeling and accurate gamma correction for fast phase measuring profilometry," *Optics Letters*, vol. 36, no. 2, pp. 154–156, 2011.

[18] X. Zhang, L. Zhu, Y. Li, and D. Tu, "Generic nonsinusoidal fringe model and gamma calibration in phase measuring profilometry," *Journal of the Optical Society of America A*, vol. 29, no. 6, pp. 1047–1058, 2012.

[19] W. Feng, S. J. Tang, X. D. Zhao, G. D. Sun, and D. X. Zhao, "Adaptive fringe projection for 3D shape measurement with large reflectivity variations by using image fusion and predicted search," *International Journal of Optics*, vol. 2020, Article ID 4876876, 14 pages, 2020.

[20] D. Zheng, F. Da, Q. Kemao, and H. S. Seah, "Phase error analysis and compensation for phase shifting profilometry with projector defocusing," *Applied Optics*, vol. 55, no. 21, p. 5721, 2016.